

SILICOALUMINOPHOSPHATE NANOPOROUS MATERIALS FOR CARBON DIOXIDE ADSORPTION AT LOW CONCENTRATION

by

Ana G. Arévalo-Hidalgo

A dissertation submitted in partial fulfillment of the requirements for the degree of

DOCTOR OF PHILOSOPHY
in
CHEMICAL ENGINEERING

UNIVERSITY OF PUERTO RICO
MAYAGÜEZ CAMPUS
2011

Approved by:

Arturo J. Hernández-Maldonado, PhD
President, Graduate Committee

Date

David Suleiman, PhD
Member, Graduate Committee

Date

María M. Martínez, PhD
Member, Graduate Committee

Date

José Colucci, PhD
Member, Graduate Committee

Date

Juan A. Ortiz, PhD
Representative of Graduate Studies

Date

Aldo Acevedo, PhD
Chairperson of the Department

Date

©Copyright 2011
Ana G. Arévalo Hidalgo. All rights reserved

This dissertation contains portions that were published by the author in the Journal of Microporous and Mesoporous Materials of Elsevier Inc., the Journal of Industrial and Engineering Chemistry Research of the American Chemical Society, and the Journal of Solid State Chemistry of Elsevier Inc.

Silicoaluminophosphate Nanoporous Materials for Carbon Dioxide Adsorption at Low Concentration

by Ana G. Arévalo -Hidalgo

Submitted to the Department of Chemical Engineering

on December 9, 2011, in partial fulfillment of the requirements for the degree of

Doctor of Philosophy

Abstract

The incorporation of extraframework Sr^{2+} and Ba^{2+} cations onto silicoaluminophosphate (SAPO-34) zeolitic materials has been proven to influence their adsorptive properties. In this study, three approaches were employed to increase the cation content and, therefore, the material adsorption capacity: a multi-step liquid-phase ion exchange (LSIE), a novel coupled partial detemplation / solid-state ion exchange (PD-SSIE) and a coupled SSIE-LSIE. The use of multi-step LSIE resulted in an increase in cation content per unit cell, but the presence of solvated species and the interaction between the in-going cation and the available sites within the structure resulted in an equilibrium limitation. On the other hand, the introduction of Sr^{2+} and Ba^{2+} cations via SSIE was found to be heavily dependent on the nature of the starting material, the temperature of the solid-state reaction, and the amount of salt used (i.e. available sites). Among the different SSIE variants, the sample prepared via PD-SSIE exhibited the best CO_2 uptake capacity at moderate gas partial pressures. Finally, the preparation of Sr^{2+} -SAPO-34 and Ba^{2+} -SAPO-34 via SSIE-LSIE resulted in materials with superior CO_2 adsorption capacity at any pressure. Furthermore, experimental and theoretical calculations studies indicated that Sr^{2+} and Ba^{2+} cations were preferentially located on Site II' extra-framework positions, which allows for the development of stronger interactions with CO_2 molecules. This was confirmed by ^1H and ^{23}Na MAS NMR studies, which allowed us to elucidate the presence and location of H^+ and Na^+ cations. This was essential to determine the amount and location of sites available for Sr^{2+} and Ba^{2+} ion exchange.

Dissertation Work Supervisor: Dr. Arturo J. Hernández-Maldonado

Silicoaluminofosfatos Nanoporosos para la Adsorción de Dióxido de Carbono a Bajas Concentraciones

by Ana G. Arévalo -Hidalgo

Submitted to the Department of Chemical Engineering

on December 9, 2011, in partial fulfillment of the requirements for the degree of

Doctor of Philosophy

Resumen

La incorporación de cationes de Sr^{2+} y Ba^{2+} en silicoaluminofosfatos (SAPO-34) nanoporosos ha demostrado tener influencia en sus propiedades de adsorción. En este estudio, se utilizaron tres estrategias para incrementar el contenido catiónico y, por lo tanto, la capacidad de adsorción del material: intercambio iónico en fase líquida realizado en multi-etapas (LSIE), una técnica novedosa que involucra remoción parcial de la plantilla e intercambio iónico en fase sólida (PD-SSIE) e intercambio iónico en fase sólida acoplado con intercambio iónico en fase líquida. El empleo de LSIE realizado en multi-etapas resultó en un incremento en el contenido catiónico por celda unitaria, pero la presencia de especies solvatadas y la interacción entre el catión que se estaba incorporando y los sitios disponibles en la estructura del material resultó en una limitación de equilibrio. Por otra parte, se encontró que la introducción de cationes de Sr^{2+} y Ba^{2+} mediante SSIE depende enormemente de la naturaleza del material base, la temperatura de la reacción en estado sólido y la cantidad de sal utilizada (i.e. sitios disponibles). Entre las diferentes variantes preparadas mediante SSIE, la muestra preparada vía PD-SSIE exhibió la mejor capacidad de adsorción de CO_2 a presiones parciales moderadas. Finalmente, la preparación de Sr^{2+} -SAPO-34 y Ba^{2+} -SAPO-34 vía SSIE-LSIE resultó en materiales con una capacidad de adsorción de CO_2 superior en todo el rango de presiones analizada. Además, estudios experimentales y cálculos teóricos indican que los cationes de Sr^{2+} y Ba^{2+} están localizados preferencialmente en el Sitio II', el cual permite el desarrollo de fuertes interacciones con las moléculas de CO_2 . Esto fue confirmado mediante estudios de ^1H y ^{23}Na MAS NMR, los cuales nos permitieron elucidar la presencia y localización de los cationes de H^+ y Na^+ . Esto fue esencial para determinar la cantidad y localización de los cationes de Sr^{2+} y Ba^{2+} en sitios disponibles para intercambio iónico.

Supervisor del Trabajo de Disertación: Dr. Arturo J. Hernández-Maldonado

DEDICATED TO MY PARENTS

Braulio Augusto Arévalo Dubón y Ana María Hidalgo Jomell,

TO MY BELOVED HUSBAND

José Roberto Ramírez Hernández

AND SPECIALLY TO MY SON

André Bautista Arévalo

Acknowledgements

First, I want to thank God for his guidance and presence in my life. Also, I am deeply grateful to my parents for teaching me the value of education and strong belief that with effort and dedication you can succeed. I want to give special thanks to my beloved son André, for his love, his patience, and the spice he brings into my life. I would like to extend my special thanks to my husband José Roberto for all his support and love and for making my life more beautiful. In addition, I want to thank my brothers Braulio, Estuardo, José Ricardo, and all my family for encouraging me to pursue my goals.

I am gratefully to the Chemical Engineering Department at the University of Puerto Rico Mayagüez for giving me the opportunity to study the Ph.D. I am grateful to my advisor, Dr. Arturo J. Hernández Maldonado, for his support, valuable guidance, and his excellent research work which made possible the successful completion of this dissertation. I am especially grateful to Dr. Antonio Estévez because he was the one who recruited me in Guatemala and for his company and mentoring in this process. I would like to express gratitude to the members of my graduate committee: Dr. David Suleiman, Dr. María Martínez, Dr. José Colucci and Dr. Juan A. Ortiz for their advice and corrections to this dissertation. I also want to thank Noelia Almodóvar who was my undergraduate student for more than two years and to Lucille Oliver and Madeline Pardo who worked with me during three summers.

I am deeply grateful with my friends Victoria Calero, Denisse Soto, Jorge Sánchez, Ana Gonzalez, Adriana Herrera, Richard Serrano, Maik Irrazábal, Vivian Florián, María Teresa Acevedo and Arlex Chavez for helping me during all this years and being part of my family. I want to thank my colleagues in the NSSAL group: Dr. Milton Rivera, Andrea Cabanzo, José

Primera, Wilman Cabrera, Jenniffer Guerrero, Marietta Marcano, Dr. Li Zhang, and specially to Dr. Sindia Rivera for being my lab mentor and for her valuable and extended help. Also, to my friends and family in the Department: Edward Guerrero, David Motta, Fernando Mérida, Karem Court, Sonia Avilés, Liliana Gámez, María del Pilar Sierra, Mar Creixell, Liliana Polo, Roberto Olayo, Isaac Torres. To all my friends in Puerto Rico: María José Pérez, Mauricio León, Mervin Pérez, Teresa Alarcón, Angie Córdoba, Luis Zapata, Omar Lazo, Ulises Barajas, Ruth Román, Alexander Recamán, Milena Salcedo, Angie Soto, Adrián Rodríguez, Adrieliz Chaparro and Vanessa Soto for all the moments we shared in “la isla del encanto”. Finally, to my friends in Guatemala; Mónica Soto, Ginger Méndez, Astrid Ucelo, Andrea Rodas Morán, Yadira Portillo, Magda Juárez, Silvia Angel, Sarah Osegueda, Regina Pacajoj, Dulce De León, Juan Gabriel Andrade, Mauricio De León, Etel Tzep, Andrea Rodas Bolaños and Febe Ávila for their friendship through the years.

I also want to thank the National Aeronautics and Space Administration (NASA) Award NNX08BA48A for providing the funding for this work. Also, partial support provided by the National Science Foundation (NSF) Center of Research Excellence in Science and Technology (CREST) Award is gratefully acknowledged. I extend my gratitude to the Puerto Rico Institute for Functional Materials under the National Science Foundation (NSF) Award No. EPS-1002410 for have provided me the opportunity of being a Graduate Fellow. The NMR experimental work was performed at the National High Magnetic Field Laboratory in collaboration with Dr. Riqiang Fu and Sneha Dugar, which is supported by NSF Cooperative Agreement No. DMR-0654118, the State of Florida and the U.S. Department of Energy. The DFT studies were performed in collaboration with Dr. Yasuyuki Ishikawa and Dr. Juan A. Santana. The TGA-FTIR and SEM/EDX analyzes were performed in the laboratory of Dr. Nelson Cardona and Dr. Carlos

Velásquez. Elemental analyzes were performed at the Chemical Department of the UPR Mayaguez with Tatiana Luna Pineda and the Material Characterization Center at UPR Río Piedras with Josué Ortiz. Oxygen isotherm analyses were performed in collaboration with Dr. María M. Martínez and Leonel Quiñones at UPRM Chemical Engineering Department.

Finally, I want to thank Maritza Arroyo, “La Red de Cuido”, and Cinderella Nursery Day Care Center for taking care of my precious baby while I was studying and conducting experiments at the university, as well as to all agencies and professionals who helped me during all these years in Puerto Rico.

Contents

Copyright.....	ii
Abstract.....	iii
Resumen.....	iv
Dedication.....	v
Acknowledgements.....	vi
Table of Contents.....	ix
List of Figures.....	xiii
List of Tables.....	xvii
1. Introduction.....	1
1.1 Carbon Dioxide Removal Applications.....	1
1.2 Materials for Carbon Dioxide Adsorption.....	2
1.3 Silicoaluminophosphate Nanoporous Materials.....	4
1.4 Sorbent Functionalization: Tailoring of the Surface Interactions.....	5
1.5 Ion Exchange Techniques.....	7
1.6 Overview of the Thesis.....	8
1.7 References.....	9
2. Separation of CO₂ from Light Gas Mixtures Using Nanoporous Silicoaluminophosphate Sorbents: Effect of Multiple-Step Ion Exchange and Adsorption Mechanism via Computational Studies.....	15
2.1 Introduction.....	16
2.2 Experimental Section.....	17
2.2.1 Sorbent Synthesis.....	17
2.2.2 Preparation of Ion-Exchanged Materials.....	18
2.2.3 X-ray Diffraction, Scanning Electron Microscopy and Compositional Analyses	18
2.2.4 Solid-State Magic Angle Spinning Nuclear Magnetic Resonance.....	19
2.2.5 Surface Area, Pore Volume and Pore-Size.....	20
2.2.6 Adsorption Equilibrium Isotherms.....	20

2.2.7 Isosteric Heat of Adsorption (ΔH_{ads}).....	21
2.2.8 DFT Calculations.....	21
2.3 Results and Discussion.....	22
2.3.1 Sorbents Characterization.....	24
2.3.2 Surface Area, Pore Volume and Pore-Size Determination.....	31
2.3.3 Carbon Dioxide Pure Component Equilibrium Adsorption.....	32
2.3.4 CO ₂ Heat of Adsorption in M ⁿ⁺ -SAPO-34.....	36
2.3.5 CO ₂ , N ₂ , O ₂ and CH ₄ Pure Component Equilibrium Adsorption in Sr ²⁺ -SAPO-34 and Ba ²⁺ -SAPO-34.....	40
2.4 Conclusions.....	41
2.5 References.....	42
 3. Sr²⁺-SAPO-34 Prepared via Coupled Partial Detemplation and Solid State Ion Exchange: Effect on Textural Properties and Carbon Dioxide Adsorption.....	 45
3.1 Introduction.....	46
3.2 Experimental Section.....	48
3.2.1 Adsorbent Synthesis.....	48
3.2.2 Preparation of Strontium (II) Ion-Exchanged Materials.....	48
3.2.3 Coupled Thermal Gravimetric Analyses (TGA)/Fourier Transform Infrared (FT-IR) Spectroscopy.....	49
3.2.4 X-ray Diffraction and Compositional Analyses.....	50
3.2.5 Porosimetry Analyses and CO ₂ Adsorption Equilibrium.....	51
3.2.6 Isosteric Heat of Adsorption (ΔH_{ads}).....	51
3.3 Results and Discussion.....	52
3.3.1 Basis SAPO-34 Materials for SSIE.....	53
3.3.2 Adsorbents Characterization.....	56
3.3.3 CO ₂ Adsorption Performance.....	65
3.4 Conclusions.....	70
3.5 References.....	71

4. Location of Cationic Species in Alkaline Earth Metal Exchanged SAPO-34	
Materials from Solid State ^1H MAS NMR and ^{23}Na MAS NMR Spectroscopy.....	76
4.1 Introduction.....	76
4.2 Experimental Section.....	79
4.2.1 Samples Preparation.....	79
4.2.2 Compositional Analyses.....	80
4.2.3 Solid-state Magic Angle Spinning Nuclear Magnetic Resonance.....	80
4.2.4 CO_2 Adsorption Equilibrium Isotherms.....	81
4.3 Results and Discussion.....	81
4.3.1 ^1H MAS-NMR investigation of partially exchanged SAPO-34 samples.....	82
4.3.2 ^{23}Na MAS-NMR investigation of partially exchanged SAPO-34 samples.....	85
4.3.3 Compositional Analyzes and Carbon Dioxide Pure Component Equilibrium Adsorption	88
4.4 Conclusions.....	90
4.5 References.....	90
5. Synthesis of SAPO-34 using triethylamine as Structure Directing Agent to Improve the Textural and Adsorptive Properties of the Sorbent Material.....	94
5.1 Introduction.....	95
5.2 Experimental Section.....	96
5.2.1 Sorbent Synthesis.....	96
5.2.2 Sorbent Characterization.....	97
5.2.3 Porosimetry Analyses and CO_2 Adsorption Equilibrium Isotherms.....	98
5.3 Results and Discussion.....	98
5.3.1 Synthesis Characterization.....	99
5.3.2 TGA-FTIR studies of Template Decomposition.....	103
5.3.3 DRIFT studies of Partial Detemplated H^+ -SAPO material.....	
5.3.4 CO_2 Adsorption Performance.....	105
5.4 Conclusions.....	107
5.5 References.....	107

6. Concluding Remarks and Thesis Contributions.....	110
Appendix.....	112
A. Ion exchanged Sr^{2+} - and Ba^{2+} -13X materials for Carbon Dioxide Adsorption Applications.....	112
B. Binder-less Procedure for Pelletizing Ion Exchanged Zeolitic Materials and CO_2 Adsorption for a Powder and a Pelletized Material.....	115
C. Sr^{2+} -SAPO-34 materials prepared via Wetness Impregnation and Solvent Mixing.....	118
D. Ion exchanged Ba^{2+} -SAPO-34 materials prepared via Coupled Partial Detemplation and Solid State Ion Exchange.....	120
E. Deconvolution Parameter for ^1H and ^{23}Na MAS NMR spectra for SAPO-34 materials...	121

List of Figures

1.1. CO ₂ adsorption isotherms at 25°C for alumina, zirconia, metal organic framework and varios zeolite materials.....	2
2.1. Chabazite framework with possible cation positions (large spheres).....	23
2.2. SEM micrographs of Na ⁺ -SAPO-34 and ion-exchanged samples prepared via multiple liquid phase ion exchange. Stages 1, 2 and 3 refer to ion exchange for 24, 48 and 72 hours, respectively.....	24
2.3. X-ray diffraction patterns for Na ⁺ -SAPO-34 and ion-exchanged samples prepared via multiple liquid phase ion exchange. Stages 1, 2 and 3 refer to ion exchange for 24, 48 and 72 hours, respectively.....	25
2.4. ²⁷ Al and ²⁹ Si MAS NMR spectra for Na ⁺ -SAPO-34 and partially exchanged Sr ²⁺ -SAPO-34 samples prepared via multiple liquid phase ion exchange. Stages 1, 2 and 3 refer to ion exchange for 24, 48 and 72 hours, respectively.....	26
2.5. ²⁷ Al and ²⁹ Si MAS NMR spectra for Na ⁺ -SAPO-34 and partially exchanged Ba ²⁺ -SAPO-34 samples prepared via multiple liquid phase ion exchange. Stages 1, 2 and 3 refer to ion exchange for 24, 48 and 72 hours, respectively.....	27
2.6. CO ₂ adsorption isotherms (normal and logarithm scales) for Na ⁺ -SAPO-34 and ion-exchanged samples prepared via multiple liquid phase ion exchange. Stages 1, 2 and 3 refer to ion exchange for 24, 48 and 72 hours, respectively.....	33
2.7. CO ₂ —Sr ²⁺ -SAPO-34 structure before (initial structure) and after (optimized structure) geometrical optimization.....	35
2.8. Isosteric heats of adsorption of CO ₂ for partially exchanged Sr ²⁺ -SAPO-34 and Ba ²⁺ -SAPO-34 sorbents prepared via multiple liquid phase ion exchange. Stages 1, 2 and 3 refer to ion exchange for 24, 48 and 72 hours, respectively.....	36
2.9. Pure component adsorption isotherms at 298 K. for CO ₂ , CH ₄ , N ₂ and O ₂ on partially exchanged Sr ²⁺ -SAPO-34 and Ba ²⁺ -SAPO-34 prepared via multiple liquid phase ion exchange. Stages 1, 2 and 3 refer to ion exchange for 24, 48 and 72 hours, respectively.....	40
3.1. Coupled thermal gravimetric analyses (TGA)(A) and Fourier transform infrared spectroscopy (FT-IR) spectra(B) of the desorbed species arising from the decomposition NH ₄ ⁺ -SAPO-34 under helium at various temperatures.....	58

3.2. Coupled thermal gravimetric analyses (TGA) (A) and Fourier transform infrared spectroscopy (FT-IR) spectra(B) of the desorbed species arising from decomposition of TEA ⁺ in Na ⁺ -SAPO-34 under helium at various temperatures.....	59
3.3. X-ray diffraction patterns and specific surface areas for Na ⁺ -SAPO-34 and ion-exchanged Sr ²⁺ -SAPO-34 samples via SSIE at 350(A) and 600°C (B), respectively, as a function of the SrCl ₂ ·6H ₂ O loading (wt.%), using NH ₄ ⁺ -SAPO-34 as basis material.....	61
3.4. X-ray diffraction patterns and specific surface areas for ion-exchanged Sr ²⁺ -SAPO-34 samples via SSIE at 430 (A) and 600°C (B), respectively, as a function of the SrCl ₂ ·6H ₂ O loading (wt.%), using as-synthesized Na ⁺ -SAPO-34as basis material. Ion exchanged Sr ²⁺ -SAPO-34 via liquid-state ion exchange (LSIE) and combination of solid state ion exchange followed by liquid-state ion exchange procedure (SSIE-LSIE) are also presented.....	63
3.5. CO ₂ adsorption isotherms obtained at 25 °C for Sr ²⁺ -SAPO-34 prepared samples via SSIE at 350(A) and 600°C (B), respectively, and NH ₄ ⁺ -SAPO-34 as basis material. The figure also included isotherm data gathered for a fully detemplated Na ⁺ -SAPO-34 material.....	66
3.6. CO ₂ adsorption isotherms obtained at 25 °C for Sr ²⁺ -SAPO-34 prepared samples via SSIE at 430(A) and 600°C (B), respectively, and as-synthesized Na ⁺ -SAPO-34 as basis material. The also included isotherm data gathered for a fully detemplated Na ⁺ -SAPO-34 material.....	67
3.7. CO ₂ adsorption isotherms obtained at 25 °C for several Sr ²⁺ -SAPO-34 samples. The figure also includes isotherm data gathered for a fully detemplated Na ⁺ -SAPO-34 material.Refer to Table 1 for sample identification.....	69
3.8. Isosteric heat of adsorption for CO ₂ inSr ²⁺ -SAPO-34 samples. Refer to Table 1 for sample identification.....	69
4.1. ¹ H MAS NMR spectra recorded at 300 MHz for fully detemplated Na ⁺ -SAPO-34 and NH ₄ ⁺ -SAPO-34 samples. The red line corresponds to the experimental data, while the black line corresponds to the simulated spectra. Blue, green and purple lines correspond to the deconvoluted resonances. Chemical shifts are referred to an adamantane sample.....	82
4.2. ¹ H MAS NMR spectra recorded at 300 MHzforSr ²⁺ -SAPO-34 and Ba ²⁺ -SAPO-34 samples prepared via LSIE,SSIE and SSIE-LSIE, respectively. The red line corresponds to the experimental data, while the black line corresponds to the simulated spectra. Blue, green and purple lines correspond to the deconvoluted resonances. Chemical shifts are referred to an adamantane sample.....	85

4.3. ^{23}Na MAS NMR spectra recorded at 900 MHz for fully detemplated Na^+ -SAPO-34 and NH_4^+ -SAPO-34 samples. The red line corresponds to the experimental data, while the black line corresponds to the simulated spectra. Blue and green lines correspond to the deconvoluted resonances. Chemical shifts are referred to a sodium chloride sample.....	86
4.4. ^{23}Na MAS NMR spectra recorded at 900 MHz for Sr^{2+} -SAPO-34 and Ba^{2+} -SAPO-34 samples prepared via LSIE, SSIE and SSIE-LSIE, respectively. The red line corresponds to the experimental data, while the black line corresponds to the simulated spectra. Blue and green lines correspond to the deconvoluted resonances. Chemical shifts are referred to a sodium chloride sample.....	88
4.5. CO_2 adsorption isotherms obtained at 25 °C for Sr^{2+} -SAPO-34 and Ba^{2+} -SAPO-34 samples prepared via LSIE, SSIE and SSIE-LSIE, respectively. The figure also includes isotherm data gathered for a fully detemplated Na^+ -SAPO-34 material. Refer to Table 4.1 for sample description.....	89
5.1. X-ray diffraction patterns for H^+ -SAPO-34 materials prepared using TEA as template and different synthesis pH values, the pattern for Na^+ -SAPO-34 synthesized using TEOH as template is also presented.....	101
5.2. SEM images of H^+ -SAPO-34 (pH=8.3) synthesized using triethylamine as SDA.....	102
5.3. ^1H MAS-NMR spectra of H^+ -SAPO-34 (pH=8.3) recorded at 900 MHz synthesized using triethylamine as SDA.....	102
5.4. Coupled thermal gravimetric analyses (TGA) and Fourier transform infrared spectroscopy (FT-IR) spectra of the desorbed species arising from decomposition of TEA^+ in H^+ -SAPO-34 (pH=8.3) under helium at various temperatures.....	104
5.5. CO_2 adsorption isotherms obtained at 25 °C for H^+ -SAPO-34 materials.....	106
A.1. CO_2 adsorption isotherms (normal and logarithm scales) for Na^+ -13X and ion-exchanged samples prepared via multiple step liquid phase ion exchange. Stages 1, 2 and 3 refer to ion exchange for 24, 48 and 72 hours, respectively.....	112
A.2. CO_2 adsorption isotherms (normal and logarithm scales), X-ray diffraction analyses, and surface area for Na^+ -13X and ion-exchanged samples prepared via solid state ion exchange.....	113
A.3. CO_2 , CH_4 , N_2 and O_2 single gas adsorption isotherms for Na^+ -13X and Sr^{2+} and Ba^{2+} -13X after 72 hours of liquid state ion exchange (SII).....	114
B.1 Punch and die set used to prepare pellets of Sr^{2+} -SAPO-34 material.....	115

B.2 CO ₂ adsorption isotherms at 25°C for a powder and a pelletized ion-exchanged Sr ²⁺ -SAPO-34 material.....	116
C.1. CO ₂ adsorption isotherms (normal and logarithm scale) obtained at 25 °C of partially exchanged Sr ²⁺ -SAPO-34 prepared via solvent mixing or wetness impregnation and subsequent solid state ion exchange treatment. The figure also included isotherm data gathered for a fully detemplated Na ⁺ -SAPO-34 material.....	117
D.1. CO ₂ adsorption isotherms (normal and logarithm scale) obtained at 25 °C of partially exchanged Ba ²⁺ -SAPO-34 prepared via Solid State Ion Exchange using A) NH ₄ ⁺ -SAPO-34 and B) as-synthesized Na ⁺ -SAPO-34 as starting materials. The figure also included isotherm data gathered for a fully detemplated Na ⁺ -SAPO-34 material.....	118
D.2. CO ₂ adsorption isotherms (normal and logarithm scale) obtained at 25 °C of partially exchanged Ba ²⁺ -SAPO-34 via Coupled Partial Detemplation and Solid State Ion Exchange (SSIE), Solid State, Conventional Liquid State Ion Exchange (LSIE) and Liquid State Ion Exchange techniques together (SSIE-LSIE), respectively. The figure also included isotherm data gathered for a fully detemplated Na ⁺ -SAPO-34 material.....	119

List of Tables

1.1. Kinetic diameter, polarizability contribution for chabazite material and Quadrupole moment for CO ₂ , N ₂ , O ₂ and CH ₄ . Also included drawings showing the approximate molecular dimensions of the molecules.....	6
2.1. Unit cell composition, surface area, pore volume and median pore width of Na ⁺ -SAPO-34 and ion-exchanged Sr ²⁺ -SAPO-34 and Ba ²⁺ -SAPO-34 materials.....	29
2.2. Calculated Sr ²⁺ binding energy (E _{bind}) SAPO-34 material at four possible sites (see Figure 1 for sites reference).....	33
2.3. Calculated CO ₂ adsorption energy (E _{ads}) on Na ⁺ -, Sr ²⁺ -, and Ba ²⁺ -SAPO-34 and Mulliken gross atomic charge on the metal cation and CO ₂ atoms.....	38
2.4. Calculated CO ₂ adsorption energy (E _{ads}) on Sr ⁿ⁺ ion (n=1, 2) in gas phase and Mulliken gross atomic charge on the constituent atoms.....	39
3.1. Unit cell composition of fully detemplated Na ⁺ -SAPO-34 and Sr ²⁺ -SAPO-34 samples prepared via SSIE. Data for samples prepared via conventional LSIE and coupled SSIE-LSIE are also presented.....	55
4.1. Unit cell composition of fully detemplated Na ⁺ -SAPO-34 and ion exchanged Sr ²⁺ -SAPO-34 and Ba ²⁺ -SAPO-34 samples prepared via conventional liquid state ion exchange (LSIE), solid state ion exchange (SSIE) and both techniques together (SSIE-LSIE).....	83
5.1. Unit cell composition of fully detemplated H ⁺ -SAPO-34 samples, prepared using triethylamine as templating agent and different pH values.....	100
E.1. ¹ H MAS NMR deconvolution parameters for SAPO-34 samples.....	120
E.2. ²³ Na MAS NMR deconvolution parameters for SAPO-34 samples.....	121
E.2. ¹ H MAS NMR deconvolution parameters for H ⁺ -SAPO-34 sample synthesized with triethylamine as template.....	121

Chapter 1

Introduction

1.1 Carbon Dioxide Removal Applications

Removal of carbon dioxide (CO₂) is an utmost necessity in many applications today, including those related to emissions to the atmosphere, gas energy sources, and breathing air purification. For example, the CO₂ released to the environment by combustion of fossil fuels is already known to greatly contribute to global warming and future stringent regulations will call for innovative ways to achieve its ultra-deep removal, whether onsite or onboard.¹⁻⁵ On the other hand, CO₂ must also be removed from natural gaseous combustible sources to improve its energy density.^{6, 7} For space life-support systems, removal and storage of CO₂ is vital since the current spacecraft maximum allowable concentration (SMAC) for CO₂ exposure during space flights requires no more than 2500 ppm for long term missions.^{8, 9} Furthermore, medical studies now suggest that a new CO₂ SMAC of less than 2500 ppm should be considered to avoid a critical loss of red cell mass, loss of plasma volume, decrease in total body water and head-ward shift of fluid after micro-gravity conditions are achieved. These new constraints call for re-evaluation of

sorption technology currently used in space missions that does not show suitable working capacities at such SMAC levels. In addition, long-term space missions would require onboard CO₂ reduction units to provide source materials for production of valuable chemicals.¹⁰ In order to supply a constant CO₂ stream it would be suitable to also consider adsorbents as a mean for storage of gas.

When approaching remediation or solution alternatives to the above scenarios it is clear across the board that the main challenge is to achieve CO₂ removal both in an effective and energy efficient way. In this respect, continuous regenerative approaches are required and an adsorption based separation scheme has been proposed as an effective and energy efficient way to remove CO₂ from space cabins, astronaut's helmets, or in any closed system that, in addition to removing the CO₂, may also allow for the recovery of oxygen.^{10, 11}

1.2 Materials for Carbon Dioxide Adsorption

As mentioned previously, to remove CO₂ in an effective and energy efficient way, suitable adsorbents should combine several attributes including high CO₂ adsorption capacity, fast kinetics, high CO₂ selectivity, mild conditions for regeneration, low cost, among others.⁵ In this respect, a large number of adsorbents for CO₂ separation have been identified during the last two decades such as metal oxides and metal oxide modified zirconia,¹² alumina and metal-promoted alumina,¹³ carbon molecular sieves (CMS),¹⁴ SBA-15,¹⁵ numerous zeolites (e.g. 5A, 13X, ZSM-5, ETS-4, X, Y, clinoptilolite and mordenite)¹⁶⁻²³ and several other materials have also been considered. Recently, metal organic frameworks have been developed specially for adsorption of CO₂ at high pressures.²⁴⁻²⁷ Comparison of the aforementioned materials is presented in Figure 1.1. The main problem is that despite of all available materials, they suffer from inadequate

working capacity and/or regeneration problems, and even selectivity limitations depending on the ultimate gas phase concentration operating range.

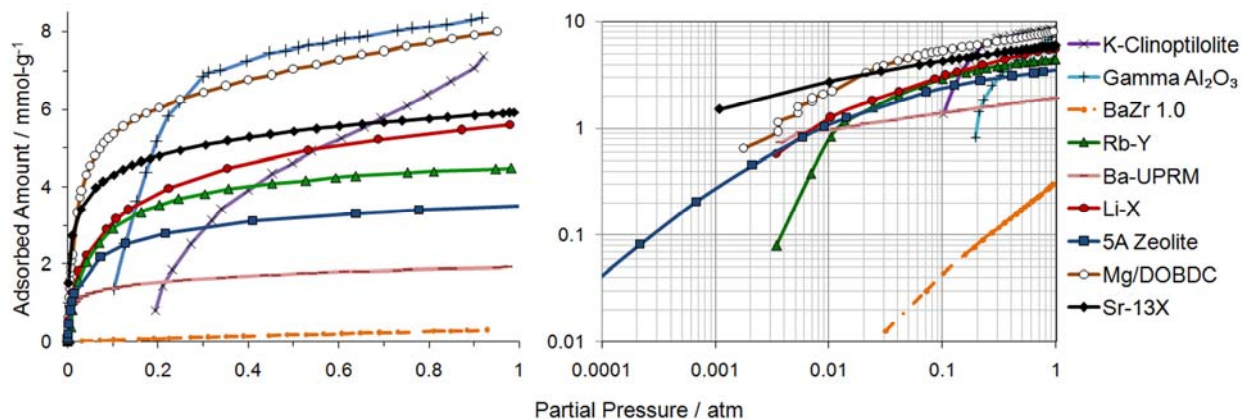


Figure 1.1. CO₂ adsorption isotherms (normal and logarithm scales) at 25°C for alumina, zirconia, metal organic framework and various zeolitic materials.^{12, 17, 20, 25, 28, 29}

For example, sorbents such as Sr-13X presents high CO₂ adsorption capacity even at low partial pressures but the problem is the high hydrophilicity of the material (additional information about Sr²⁺ and Ba²⁺-13X materials is presented in Appendix A). Metal organic frameworks (MOFs) such as MgDOBDC show high adsorption capacity although effective regeneration of the sorbents is still under study.²⁵ Figure 1.1 also shows that materials such as K-Clinoptilolite, Gamma Al₂O₃ and Zirconia are not suitable options for low partial pressures applications.^{12, 17} Even though, zeolitic materials such as 5A, LiX, Ba-UPRM and RbY present a considerable CO₂ adsorption,^{20, 28, 29} there is still room for improvement especially in the low partial pressure range to comply with requirements such as NASA Carbon Dioxide Removal Assembly.

1.3 Silicoaluminophosphate Nanoporous Materials

Silicoaluminophosphates (SAPO-34) are crystalline nanoporous materials with the framework characteristics of the natural zeolite Chabazite. The structure of SAPO-34 is formed by tetrahedrally coordinated silicon, aluminum, phosphorous, and oxygen atoms assembled into well-defined hexagonal pores and cavities. Depending on the substitution of silicon for aluminum, phosphorous or simultaneous substitution of two silicon for one aluminum and one phosphorous, the SAPO framework holds a net charge of +1, -1, or 0, respectively.^{30, 31} Protons or cations are necessary to counterbalance the SAPO-34 framework charge. These species can be exchanged by other metal cations changing the net electronic charge, the atomic radii and the field-gradient quadrupole contribution to the total adsorption energy.³² Thus, extra-framework cations play an important role in determining the adsorption, separation, and catalytic properties of zeolites.³³⁻³⁶ Exhaustive studies have reported that the most promising zeolites for CO₂ adsorption are characterized by a low Si/Al ratio, corresponding to high content of extraframework cations.

The incorporation of metal cations into SAPO-34 framework resulted in promising materials for the selective removal of CO₂ from light gas mixtures at temperatures and pressures that approach ambient conditions.^{6, 37-47} In 2007 Rivera-Ramos and Hernández-Maldonado reported a SAPO-34 variant possessing extraframework strontium cations (Sr²⁺-SAPO-34)^{48, 49} which has a high adsorption capacity and selectivity for the removal of CO₂ from light gas mixtures, especially for ultra-purification applications. The sorbent is effectively functionalized by the exposed Sr²⁺ species and the small dimensions of the SAPO-34 cages, which combined still do not provide transport resistance or pore blocking to the structure. In addition, the observed

adsorption interactions are in the physisorption range and therefore the adsorbent can be fully regenerated by simple engineering methods (i.e., lowering pressure). Furthermore, Hernandez-Maldonado and co-workers⁴⁹ proposed that introducing additional extraframework Sr^{2+} cations in the partially exchanged Sr^{2+} -SAPO-34 sorbent could further improve its adsorptive capacity since the observed adsorption amounts are well below the saturation value, and this is part of the motivation of the present thesis dissertation.

1.4 Sorbent Functionalization: Tailoring of the Surface Interactions

For a better understanding of the adsorptive properties of SAPO-34 materials toward CO_2 , it is important to analyze the sorbate-sorbent interactions or the heat of adsorption of the material which correlates with the shape of the isotherms. At ambient temperatures, for physisorption level interactions and low surface coverage, the heat of adsorption can be related to dispersion and repulsion energies (nonspecific) and additional components attributed to electrostatic interactions (specific) as follows.³²

$$\phi \approx \Delta H_{ads} \quad (1.1)$$

$$\phi \approx \phi_{\text{sorbate-sorbate}} + \phi_{\text{sorbate-sorbent}} \quad (1.2)$$

$$\phi \approx \phi_D + \phi_R + \phi_{Ind} + \phi_{F\mu} + \phi_{FQ} \quad (1.3)$$

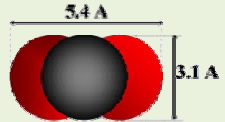
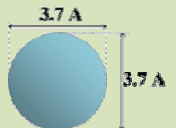
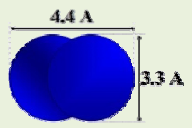
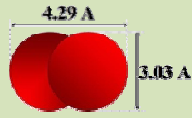
Where ϕ_D is the dispersion energy, ϕ_R is the close-range repulsion energy, ϕ_{Ind} is the induction energy between the electric field and an induced dipole ϕ_F is the interaction between electric field \vec{F} and a permanent dipole μ , and ϕ_{FQ} is the interaction between field gradient \vec{F} and a quadrupole.³²

The nonspecific interactions (ϕ_D and ϕ_R) strongly depend on the polarizability, α . On the other hand, the specific contributions (ϕ_{Ind} , $\phi_{F\mu}$ and ϕ_{FQ}) arise from charges on the solid surface, and these have been discussed extensively by Hernandez Maldonado et al.³³ These interactions can be described in the following terms:

$$\phi_D \propto -\frac{\alpha}{r_0^6}, \phi_R \propto \frac{\alpha}{2r_0^6}, \phi_{Ind} \propto \frac{q_C^2 \alpha}{r_0^4}, \phi_{FQ} \propto \frac{q_C^2 Q}{r_0^3} \quad (1.4-1.7)$$

where r_0 is the contact distance between the centers of the interacting pair, q_c is the electronic charge of the cation or functionalization species and Q is the quadrupole moment.³²

Table 1.1. Kinetic diameter, polarizability contribution for chabazite material and quadrupole moment for CO₂, N₂, O₂ and CH₄. Drawings included show the approximate molecular dimensions of the molecules.³²

	Kinetic Diameter (Å)	Polarizability (cm ³)	Quadrupole (erg ^{1/2} cm ^{5/2})
CO₂ 	3.30	29.1x10 ⁻²⁵	4.3x10 ⁻²⁶
CH₄ 	3.80	25.0x10 ⁻²⁵	0
N₂ 	3.64	17.6x10 ⁻²⁵	1.47x10 ⁻²⁶
O₂ 	3.46	16.3x10 ⁻²⁵	0.39x10 ⁻²⁶

Analyzing the kinetic diameters and the polarizabilities of CO₂, O₂, N₂ and CH₄ presented in Table 1.1, a simple inspection of these values it is possible to conclude that CO₂ will have a slight advantage in the nonspecific interactions region and for the specific contributions the considerable difference in sorbates quadrupole moment (see Table 1) will be the driving force for the design and synthesis of the sorbents proposed here.

1.5 Ion Exchange Techniques

To improve the adsorption capacity and selectivity of the material it is desired to optimize ion exchange methods in order to increase the concentration of extraframework cations per unit cell. Techniques such as conventional and multi step liquid state ion exchange,^{33, 50-52} wetness impregnation^{36, 53-56} as well as solid state ion exchange⁵⁷⁻⁶² have been studied to fully exchange the charge-balancing species.

Liquid state ion exchange is the conventional method to incorporate metal cations into zeolitic materials. The problem is that not all metal cations can be exchanged to exhaustion since classical hydrolysis mechanisms⁶³ and equilibrium limitations are present.^{32, 64} On the other hand, solid-state ion exchange (SSIE) technique, is an excellent approach of exchanging cations in a more direct fashion. The advantages of SSIE over conventional ion exchange from aqueous media include:^{65, 66} (i) avoiding the use of large volumes of salt solution, (ii) avoiding the problem of discarding waste salt solution, and (iii) allowing the metal cations (which are small) to be introduced through narrow windows or channels that would impede or prevent the ion exchange of solvated cations (which are larger) from aqueous solution. Therefore, the advantage of employing solid-state ion exchange (SSIE) is the potential elimination of some if not all of the equilibrium problems previously mentioned. Although this comes at the expense of a higher

energy input (i.e., solid phase diffusion), this technique has proven to be effective for other zeolitic systems.^{58, 67, 68}

1.6 Overview of the Thesis

The main objective of this dissertation is the development of silicoaluminophosphate nanoporous sorbents for CO₂ adsorption at low concentration. Two different strategies were studied to increase the Sr²⁺ and Ba²⁺ functional surface species and therefore improve the CO₂ adsorption capacity of the sorbent material; first, the incorporation of Sr²⁺ and Ba²⁺ extraframework cations via multi-step liquid phase ion exchange and second, the incorporation of the metal cations via solid state ion exchange, including a novel couple partial detemplation and solid state ion exchange approach, and the use of both liquid and solid state ion exchange techniques together. In addition, it also presents the study of the location of extraframework cations in the material structure using MAS-NMR technique and the synthesis of SAPO-34 material using a sodium free approach to improve the cation loading in the material.

Chapter 2 presents the study of the incorporation of Sr²⁺ and Ba²⁺ cations in SAPO-34 material via multi-step liquid phase ion exchange (M-LPIE) for the selective adsorption of CO₂ at temperatures and pressures that approach ambient conditions. Using crystallinity, textural characteristics and adsorptive properties of Na⁺-SAPO-34 and exchanged materials, the limitations of the LPIE technique were established. In addition, a density functional theory (DFT) study is presented as an effort to elucidate the CO₂ adsorption mechanism in both sorbent variants. This part of the work was published in the Microporous and Mesoporous Materials Journal in 2010.⁶⁹

Chapter 3 focuses on the evaluation of solid state ion exchange technique (SSIE) for the introduction of extraframework Sr^{2+} cations onto SAPO-34 material. It has been studied the use of different strontium chloride salt loadings ($\text{SrCl}_2 \cdot 6\text{H}_2\text{O}$), ion exchange temperatures, and starting materials (i.e. NH_4^+ -SAPO-34 vs. Na^+ -SAPO-34). The use of a partial detemplation (PD) method was also included and used in combination with solid and liquid state ion exchange techniques (PD-SSIE-LSIE) for the exchange of tenacious Na^+ ions remaining in the SAPO-34 crystal structure after SSIE. The work presented in this chapter was published in Industrial and Engineering Chemical Research Journal in 2011.⁷⁰

Chapter 4 presents a study of the location of the extra-framework sodium and hydrogen cations in Sr^{2+} and Ba^{2+} -SAPO-34 materials prepared by using ^1H and ^{23}Na Magic Angle Spinning Nuclear Magnetic Resonance (MAS NMR) experiments at room temperatures. The results obtained were correlated with the CO_2 adsorption and compositional analysis of the samples. The work presented in this chapter has been submitted for publication in the Journal of Solid State Chemistry in 2011.

Chapter 5 includes the synthesis of silicoaluminophosphates using an alternative structure directing agent or template, triethylamine (TEA), with the purpose of avoiding the presence of tenacious sodium cations that remain after the ion exchange treatments as studied in the previous chapters.

Finally, the more relevant contributions of the thesis are presented in Chapter 6. Complementary data and additional experiments are included in the Appendix Section.

References

1. Abanades, J. C.; Rubin, E. S.; Anthony, E. J., Sorbent Cost and Performance in CO₂ Capture Systems. *Ind. Eng. Chem. Res.* **2004**, 43, (13), 3462-3466.
2. Herzog, H., What Future for Carbon Capture and Sequestration? *Environ. Sci. Technol.* **2001**, 35, (7), 148A-153A.
3. Idem, R.; Tontiwachwuthikul, P., Preface for the Special Issue on the Capture of Carbon dioxide from Industrial Sources: Technological Developments and Future Opportunities. *Ind. Eng. Chem. Res.* **2006**, 45, (8), 2413-2413.
4. Olajire, A. A., CO(2) capture and separation technologies for end-of-pipe applications - A review. *Energy* **2010**, 35, (6), 2610-2628.
5. Sayari, A.; Belmabkhout, Y.; Serna-Guerrero, R., Flue gas treatment via CO(2) adsorption. *Chemical Engineering Journal* **2011**, 171, (3), 760-774.
6. Li, S. G.; Falconer, J. L.; Noble, R. D., SAPO-34 Membranes for CO₂/CH₄ Separation. *J. Membrane Sci.* **2004**, 241, (1), 121-135.
7. Baker, R. W., Future directions of membrane gas separation technology. *Ind. Eng. Chem. Res.* **2002**, 41, (6), 1393-1411.
8. National Research Council (U.S.). Subcommittee on Spacecraft Maximum Allowable Concentrations., *Spacecraft Maximum Allowable Concentrations for Selected Airborne Contaminants*. National Academy Press: Washington, D.C., 1996; p v. <2-4>.
9. Seter, A. J. *Allowable Exposure Limits for Carbon Dioxide During Extravehicular Activity*; Technical Memorandum 103832; NASA Ames Research Center: Moffett Field, April, 1993.
10. Brooks, K. P.; Hu, J. L.; Zhu, H. Y.; Kee, R. J., Methanation of Carbon Dioxide by Hydrogen Reduction Using the Sabatier Process in Microchannel Reactors. *Chem. Eng. Sci.* **2007**, 62, (4), 1161-1170.
11. Hwang, H. T.; Harale, A.; Liu, P. K. T.; Sahimi, M.; Tsotsis, T. T., A membrane-based reactive separation system for CO₂ removal in a life support system. *Journal of Membrane Science* **2008**, 315, (1-2), 116-124.
12. Liu, A. G.; Nyavor, K.; Ankumah, R., Structural and Adsorptive Properties of Ba or Mg Oxide Modified Zirconia. *J. Colloid Interf. Sci.* **2005**, 284, (1), 66-70.
13. Lee, K. B.; Sircar, S., Removal and Recovery of Compressed CO₂ from Flue Gas by a Novel Thermal Swing Chemisorption Process. *AIChE J.* **2008**, 54, (9), 2293-2302.
14. Kim, T. H.; Vijayalakshmi, S.; Son, S. J.; Ryu, S. K.; Kim, J. D., A Combined Study of Preparation and Characterization of Carbon Molecular Sieves (CMS) for Carbon Dioxide Adsorption from Coals of Different Origin. *J. Ind. Eng. Chem.* **2003**, 9, (5), 481-487.
15. Liu, X. W.; Zhou, L.; Fu, X.; Sun, Y.; Su, W.; Zhou, Y. P., Adsorption and Regeneration Study of the Mesoporous Adsorbent SBA-15 Adapted to the Capture/Separation of CO₂ and CH₄. *Chem. Eng. Sci.* **2007**, 62, (4), 1101-1110.

16. Mulloth, L. M.; Finn, J. E. *Carbon Dioxide Adsorption on a 5A Zeolite Designed for CO₂ Removal in Spacecraft Cabins*; NASA Ames Research Center: Moffett Field, 1998.
17. Rege, S. U.; Yang, R. T.; Buzanowski, M. A., Sorbents for air prepurification in air separation. *Chemical Engineering Science* **2000**, 55, (21), 4827-4838.
18. Siporin, S. E.; McClaine, B. C.; Davis, R. J., Adsorption of N₂ and CO₂ on Zeolite X Exchanged with Potassium, Barium, or Lanthanum. *Langmuir* **2003**, 19, (11), 4707-4713.
19. Takamura, Y.; Narita, S.; Aoki, J.; Hironaka, S.; Uchida, S., Evaluation of Dual-Bed Pressure Swing Adsorption for CO₂ Recovery from Boiler Exhaust Gas. *Sep. Purif. Technol.* **2001**, 24, (3), 519-528.
20. Walton, K. S.; Abney, M. B.; LeVan, M. D., CO₂ Adsorption in Y and X Zeolites Modified by Alkali Metal Cation Exchange. *Micropor. Mesopor. Mat.* **2006**, 91, (1-3), 78-84.
21. Hyun, S. H.; Song, J. K.; Kwak, B. I.; Kim, J. H.; Hong, S. A., Synthesis of ZSM-5 Zeolite Composite Membranes for CO₂ Separation. *J. Mater. Sci.* **1999**, 34, (13), 3095-3103.
22. Delgado, J. A.; Uguina, M. A.; Gomez, J. M.; Ortega, L., Adsorption Equilibrium of Carbon Dioxide, Methane and Nitrogen onto Na- and H-Mordenite at High Pressures. *Sep. Purif. Technol.* **2006**, 48, (3), 223-228.
23. Pillai, R. S.; Peter, S. A.; Jasra, R. V., Adsorption of Carbon Dioxide, Methane, Nitrogen, Oxygen and Argon in NaETS-4. *Micropor. Mesopor. Mat.* **2008**, 113, (1-3), 268-276.
24. Li, J. R.; Ma, Y. G.; McCarthy, M. C.; Sculley, J.; Yu, J. M.; Jeong, H. K.; Balbuena, P. B.; Zhou, H. C., Carbon dioxide capture-related gas adsorption and separation in metal-organic frameworks. *Coordination Chemistry Reviews* 255, (15-16), 1791-1823.
25. Caskey, S. R.; Wong-Foy, A. G.; Matzger, A. J., Dramatic tuning of carbon dioxide uptake via metal substitution in a coordination polymer with cylindrical pores. *Journal of the American Chemical Society* **2008**, 130, (33), 10870-+.
26. Liu, J.; Benin, A. I.; Furtado, A. M. B.; Jakubczak, P.; Willis, R. R.; LeVan, M. D., Stability Effects on CO(2) Adsorption for the DOBDC Series of Metal-Organic Frameworks. *Langmuir* **2011**, 27, (18), 11451-11456.
27. Garcia-Ricard, O. J.; Hernandez-Maldonado, A. J., Cu(2)(pyrazine-2,3-dicarboxylate)(2)(4,4'-bipyridine) Porous Coordination Sorbents: Activation Temperature, Textural Properties, and CO(2) Adsorption at Low Pressure Range. *Journal of Physical Chemistry C* 114, (4), 1827-1834.
28. Mulloth, L. M.; Finn, J. E., Carbon dioxide adsorption on a 5A zeolite designed for CO₂ removal in spacecraft cabins. In Center, N. A. R., Ed. NASA/TM-1998-208752: Moffett Field, CA, 1998; p 1.
29. Primera-Pedrozo, J. N.; Torres-Cosme, B. D.; Clardy, M. E.; Rivera-Ramos, M. E.; Hernandez-Maldonado, A. J., Titanium Silicate Porous Materials for Carbon Dioxide Adsorption: Synthesis Using a Structure Directing Agent, Detemplation and Inclusion of Alkaline Earth Metal Cations. *Ind. Eng. Chem. Res.* 49, (16), 7515-7523.

30. Lok, B. M.; Messina, C. A.; Patton, R. L.; Gajek, R. T.; Cannan, T. R.; Flanigen, E. M., Silicoaluminophosphate molecular-sieves: Another new class of microporous crystalline inorganic solids. *Journal of the American Chemical Society* **1984**, 106, (20), 6092-6093.
31. Lok, B. M.; Messina, C. A.; Patton, R. L.; Gajek, R. T.; Cannan, T. R.; Flanigen, E. M. Crystalline Silicoaluminophosphates. 1984.
32. Yang, R. T., *Adsorbents: Fundamentals and Applications*. Wiley: New York, 2003.
33. Rivera-Ramos, M. E.; Hernandez-Maldonado, A. J., Adsorption of N₂ and CH₄ by ion-exchanged silicoaluminophosphate nanoporous sorbents: Interaction with monovalent, divalent, and trivalent cations. *Ind. Eng. Chem. Res.* **2007**, 46, (14), 4991-5002.
34. Pirngruber, G. D.; Raybaud, P.; Belmabkhout, Y.; Cejka, J.; Zuck, A., The role of the extra-framework cations in the adsorption of CO(2) on faujasite Y. *Physical Chemistry Chemical Physics* **2010**, 12, (41), 13534-13546.
35. Esquivel, D.; Cruz-Cabeza, A. J.; Jimenez-Sanchidrian, C.; Romero-Salguero, F. J., Local environment and acidity in alkaline and alkaline-earth exchanged beta zeolite: Structural analysis and catalytic properties. *Microporous and Mesoporous Materials* 142, (2-3), 672-679.
36. Wei, Y. X.; Zhang, D. Z.; Xu, L.; Chang, F. X.; He, Y. L.; Meng, S. H.; Su, B. L.; Liu, Z. M., Synthesis, characterization and catalytic performance of metal-incorporated SAPO-34 for chloromethane transformation to light olefins. *Catalysis Today* **2008**, 131, (1-4), 262-269.
37. Poshusta, J. C.; Tuan, V. A.; Pape, E. A.; Noble, R. D.; Falconer, J. L., Separation of Light Gas Mixtures Using SAPO-34 Membranes. *AIChE J.* **2000**, 46, (4), 779-789.
38. Li, S. G.; Alvarado, G.; Noble, R. D.; Falconer, J. L., Effects of Impurities on CO₂/CH₄ Separations through SAPO-34 Membranes. *J. Membrane Sci.* **2005**, 251, (1-2), 59-66.
39. Li, S. G.; Martinek, J. G.; Falconer, J. L.; Noble, R. D.; Gardner, T. Q., High-Pressure CO₂/CH₄ Separation using SAPO-34 Membranes. *Ind. Eng. Chem. Res.* **2005**, 44, (9), 3220-3228.
40. Li, S. G.; Falconer, J. L.; Noble, R. D., Improved SAPO-34 Membranes for CO₂/CH₄ Separations. *Adv. Mater.* **2006**, 18, (19), 2601.
41. Li, S. G.; Falconer, J. L.; Noble, R. D.; Krishna, R., Modeling Permeation of CO₂/CH₄, CO₂/N₂, and N₂/CH₄ Mixtures Across a SAPO-34 Membrane with the Maxwell-Stefan Equations. *Ind. Eng. Chem. Res.* **2007**, 46, (12), 3904-3911.
42. Hong, M.; Li, S.; Funke, H. F.; Falconer, J. L.; Noble, R. D., Ion-exchanged SAPO-34 Membranes for Light Gas Separations. *Micropor. Mesopor. Mat.* **2007**, 106, (1-3), 140-146.
43. Carreon, M.; Li, S.; Falconer, J.; Noble, R., Alumina-supported SAPO-34 membranes for CO₂/CH₄ separation. *J. Am. Chem. Soc.* **2008**, 130, (16), 5412.
44. Hong, M.; Li, S. G.; Falconer, J. L.; Noble, R. D., Hydrogen Purification using a SAPO-34 Membrane. *J. Membrane Sci.* **2008**, 307, (2), 277-283.
45. Krishna, R.; Li, S.; van Baten, J. M.; Falconer, J. L.; Noble, R. D., Investigation of Slowing-Down and Speeding-Up Effects in Binary Mixture Permeation Across SAPO-34 and MFI Membranes. *Sep. Purif. Technol.* **2008**, 60, (3), 230-236.

46. Li, S. G.; Falconer, J. L.; Noble, R. D., SAPO-34 Membranes for CO₂/CH₄ Separations: Effect of Si/Al Ratio. *Micropor. Mesopor. Mat.* **2008**, 110, (2-3), 310-317.
47. Avila, A.; Funke, H.; Zhang, Y.; Falconer, J.; Noble, R., Concentration Polarization in SAPO-34 Membranes at High Pressures. *J. Membrane Sci.* **2009**.
48. Rivera-Ramos, M. E.; Ruiz-Mercado, G. J.; Hernandez-Maldonado, A. J., Separation of CO₂ from Light Gas Mixtures using Ion-Exchanged Silicoaluminophosphate Nanoporous Sorbents. *Ind. Eng. Chem. Res.* **2008**, 47, (15), 5602-5610.
49. Rivera-Ramos, M. E.; Hernandez-Maldonado, A. J., Adsorption of N₂ and CH₄ by Ion-Exchanged Silicoaluminophosphate Nanoporous Sorbents: Interaction with Monovalent, Divalent, and Trivalent Cations. *Ind. Eng. Chem. Res.* **2007**, 46, (14), 4991-5002.
50. Murad, S.; Jia, W.; Krishnamurthy, M., Ion-exchange of monovalent and bivalent cations with NaA zeolite membranes: a molecular dynamics study. *Molecular Physics* **2004**, 102, (19-20), 2103-2112.
51. Dyer, A., Ion-exchange capacity. *Microporous and Mesoporous Materials* **1998**, 22, (4-6), 543-545.
52. Melian-Cabrera, I.; Espinosa, S.; Groen, J. C.; van de Linden, B.; Kapteijn, F.; Moulijn, J. A., Utilizing full-exchange capacity of zeolites by alkaline leaching: Preparation of Fe-ZSM5 and application in N₂O decomposition. *Journal of Catalysis* **2006**, 238, (2), 250-259.
53. Obrzut, D. L.; Adekkanattu, P. M.; Thundimadathil, J.; Liu, J.; Dubois, D. R.; Guin, J. A., Reducing methane formation in methanol to olefins reaction on metal impregnated SAPO-34 molecular sieve. *Reaction Kinetics and Catalysis Letters* **2003**, 80, (1), 113-121.
54. Dzwigaj, S.; Che, M., Oxidation state of vanadium introduced in dealuminated beta zeolite by impregnation with V(IV)OSO(4) solution: Influence of preparation parameters. *Journal of Physical Chemistry B* **2005**, 109, (47), 22167-22174.
55. Michalska, A.; Daturi, M.; Saussey, J.; Nowak, I.; Ziolek, M., The role of MCM-41 composition in the creation of basicity by alkali metal impregnation. *Microporous and Mesoporous Materials* **2006**, 90, (1-3), 362-369.
56. Roldan, R.; Beale, A. M.; Sanchez-Sanchez, M.; Romero-Salguero, F. J.; Jimenez-Sanchidrian, C.; Gomez, J. P.; Sankar, G., Effect of the impregnation order on the nature of metal particles of bi-functional Pt/Pd-supported zeolite Beta materials and on their catalytic activity for the hydroisomerization of alkanes. *Journal of Catalysis* **2008**, 254, (1), 12-26.
57. Zamaro, J. M.; Miro, E. E.; Boix, A. V.; Martinez-Hernandez, A.; Fuentes, G. A., In-zeolites prepared by oxidative solid state ion exchange (OSSIE): Surface species and structural characterization. *Microporous and Mesoporous Materials* **2010**, 129, (1-2), 74-81.
58. Weitkamp, J.; Ernst, S.; Bock, T.; Kromminga, T.; Kiss, A.; Kleinschmit, P. Modified Molecular Sieves by means of Solid Ion Exchange. 1996.
59. Mihalyi, R. M.; Schay, Z.; Szegedi, A., Preparation of In,H-ZSM-5 for DeNO_x reactions by solid-state ion exchange. *Catalysis Today* **2009**, 143, (3-4), 253-260.
60. Zhang, Y. H.; Drake, I. J.; Bell, A. T., Characterization of Cu-ZSM-5 prepared by solid-state ion exchange of H-ZSM-5 with CuCl. *Chemistry of Materials* **2006**, 18, (9), 2347-2356.

61. Price, G. L., Solid state ion exchange of zeolites. *Abstracts of Papers of the American Chemical Society* **2004**, 227, U831-U831.
62. Teraoka, Y.; Furukawa, H.; Moriguchi, I., Preparation of copper-loaded MFI zeolites by solid-state ion exchange method and their catalytic activity for direct NO decomposition. In *Science and Technology in Catalysis 2002*, Anpo, M.; Onaka, M.; Yamashita, H., Eds. 2003; Vol. 145, pp 231-234.
63. Baes, C.; Mesmer, R., The Hydrolysis of Cations. *RE Krieger, Malabar* **1986**.
64. Breck, D. W., *Zeolites Molecular Sieves*. Wiley: New York, 1973.
65. Karge, H.; Wichterlová, B.; Beyer, H., High-temperature interaction of solid Cu chlorides and Cu oxides in mixtures with H-forms of ZSM-5 and Y zeolites. *Journal of the Chemical Society, Faraday Transactions* **1992**, 88, (9), 1345-1351.
66. Haniffa, R.; Seff, K., Partial Structures of Fully Dehydrated Ni₃₀Na₇Cl₁₂Si₁₃₇Al₅₅O₃₈₄ (Solid-State Nickel (II)-Exchanged Zeolite Y) and of Its D₂O Sorption Complex by Pulsed-Neutron Diffraction. *J. Phys. Chem. B* **1998**, 102, (15), 2688-2695.
67. Haniffa, R.; Seff, K., Partial Structures of Fully Dehydrated Ni₃₀Na₇Cl₁₂Si₁₃₇Al₅₅O₃₈₄ (Solid-State Nickel(II)-Exchanged Zeolite Y) and of Its D₂O Sorption Complex by Pulsed-Neutron Diffraction. *J. Phys. Chem. B* **1998**, 102, (15), 2688-2695.
68. Zanjanchi, M. A.; Ebrahimian, A., Studies on the Solid-State Ion Exchange of Nickel Ions into Zeolites Using DRS Technique. *J. Mol. Struct.* **2004**, 693, (1-3), 211-216.
69. Arévalo-Hidalgo, A. G.; Santana, J. A.; Fu, R.; Ishikawa, Y.; Hernández-Maldonado, A. J., Separation of CO₂ from light gas mixtures using nanoporous silicoaluminophosphate sorbents: Effect of multiple-step ion exchange and adsorption mechanism via computational studies. *Microporous and Mesoporous Materials* **2009**, 130, (1-3), 142-153.
70. Arevalo-Hidalgo, A. G.; Almodovar-Arbelo, N. E.; Hernandez-Maldonado, A. J., Sr²⁺-SAPO-34 Prepared via Coupled Partial Detemplation and Solid State Ion Exchange: Effect on Textural Properties and Carbon Dioxide Adsorption. *Ind. Eng. Chem. Res.* **2011**, 50, (17), 10259-10269.

Chapter 2

Separation of CO₂ from Light Gas Mixtures Using Nanoporous Silicoaluminophosphate Sorbents: Effect of Multiple-Step Ion Exchange and Adsorption Mechanism via Computational Studies

Na⁺-SAPO-34 materials were partially exchanged with Sr²⁺ and Ba²⁺ cations in a multi-step fashion in an attempt to improve adsorptive properties and study the effect of ion exchange treatments on the morphological, textural and chemical properties. Characterization of the sorbents included scanning electron microscopy (SEM), X-ray diffraction (XRD), solid-state magic angle spinning nuclear magnetic resonance (MAS-NMR), energy-dispersive analysis by X-ray diffraction (EDAX), porosimetry, and pure component gas adsorption (sorbates: CO₂, N₂, O₂ and CH₄). Analysis of the textural and adsorptive properties of SAPO-34 as a function of the degree of exchange corroborated that the long-range order of the sorbents was preserved. MAS-NMR spectra revealed that the calcination process to remove the template from Na⁺-SAPO-34 materials produces a small fraction of extra-framework or amorphous species in the local structure, but no changes associated to the multi-stage ion exchange process were observed. Performance wise both the Sr²⁺ and Ba²⁺ sorbent variants showcase outstanding adsorption capacity and selectivity towards CO₂, especially at low gas partial pressures. The multi-step ion

exchange procedure was effective in increasing the barium content in the SAPO-34 unit cell, resulting in an increase in CO₂ uptake. Both experimental and theoretical analyses suggest that Sr²⁺ and Ba²⁺ cations are located at exposed positions within the material framework (site II'), which should explain the resulting interaction with CO₂ molecules and, therefore, high adsorption capacity. Furthermore, a Mulliken gross atomic charge study indicates that the interaction between CO₂ and the adsorption sites is predominantly a bond of ionic character. In general the results indicate that both sorbent materials are good alternatives for CO₂ adsorption, especially for ultrapurification applications.

2.1. Introduction

The introduction of additional extraframework Sr²⁺ cations in the partially exchanged Sr²⁺-SAPO-34 sorbent could further improve its adsorptive capacity since the observed adsorption amounts are well below the saturation value. To improve the adsorption capacity and selectivity of a silicoaluminophosphate framework (or a zeolitic material), it is desired to optimize ion exchange methods to increase the concentration of extraframework cations per unit cell.

In this study Na⁺-SAPO-34 was modified by means of a multi-step liquid phase ion exchange (M-LPIE) strategy. Previous studies have analyzed the structural and textural characteristics of zeolites as a function of the adsorptive properties of the materials. For example, it was found that after the incorporation of copper and zinc cations via binary and ternary exchanges in zeolite X, the material lost its crystallinity, being accentuated after the ternary exchange.¹ Also, a significant reduction in the crystallinity of NaY material was observed after three ion exchange steps to introduce NH₄⁺ into the zeolitic material.² For cation-exchanged LTA zeolites, using a one-step LPIE to incorporate Li⁺, Co²⁺, Ni⁺, Cu²⁺ and Zn²⁺, it was found crystalline damage in

the material related to low pH of the exchanging solutions or produced during the dehydration of the materials.³ For the case of ion exchanged A zeolite with nitrate solutions containing Li^+ , K^+ , Mg^{2+} , Ca^{2+} , Sr^{2+} , Zn^{2+} , Cd^{2+} , Co^{2+} , Ni^{2+} and Mn^{2+} with NaA zeolite it was found stability effects of the material as function of the percentage of cation exchange and the results were more striking in the case of Sr^{2+} and K^+ ion exchange.⁴ These studies indicate that LPIE has shown strong influence on textural properties of the material, including the working surface area and particle morphology.

The main goal of this study was to maximize the concentration of Sr^{2+} and Ba^{2+} cations in the SAPO-34 unit cell, respectively, via M-LPIE. The limitations of the LPIE technique were established based on the observed crystallinity, textural characteristics and adsorptive properties of the Na^+ -SAPO-34 (i.e., calcined SAPO-34) and exchanged materials. In addition, an effort to elucidate the CO_2 adsorption mechanism has been made in both sorbent variants by means of a density functional theory (DFT) study. By combining the experimental and theoretical efforts, this study aims to develop better nanoporous sorbents for the selective and high capacity gas separations involving CO_2 .

2.2. Experimental Section

2.2.1 Sorbent Synthesis

The crystalline material, Na^+ -SAPO-34, was synthesized by hydrothermal crystallization using tetraethylammonium hydroxide (TEAOH) as a structure directing agent (SDA).⁵ The procedure was previously reported by our research group^{6, 7} and elsewhere^{5, 8}. Some small modifications have been done to the general procedure and better results were observed when

vigorous mixing and aging times of 2 hours for each mixing step of the synthesis. The TEAOH is removed from the nanoporous material framework by calcination at 873 K in a computer controlled muffle furnace using flowing air.⁹

2.2.2 Preparation of Ion-Exchanged Materials

The detemplated material was effectively modified by means of liquid phase ion exchange with the respective salt containing the in going cation, being Sr^{2+} and Ba^{2+} for this study. Details of the procedure have been also reported by Hernandez Maldonado et al. and are available elsewhere.^{6, 7, 10, 11} The degree of ion exchange was optimized using multi-steps of 24 hours each, renewing the salt solution after each step, and improving the selection of the concentration gradient between the zeolite and the salt solution. The general procedure was based on the amount of salt necessary to achieve complete ion exchange and the solubility of the respective salt in water at the experimental conditions. A high cation chloride salt/zeolite aqueous solution with an equivalent molar ratio of 20:1 for strontium ($5.4 < \text{pH} < 5.6$) and 30:1 for barium ($5.3 < \text{pH} < 5.7$) were used for ion exchange, respectively. The ion exchange was performed in three steps. Each equilibration step was performed at 333 K under vigorous stirring for 24 hours. After each ion-exchange step, the samples were filtered with copious amount of deionized/distilled water and dried at 363 K for 24 h in a forced convection oven.

2.2.3 X-ray Diffraction, Scanning Electron Microscopy and Compositional Analyses

Na^+ -SAPO-34 materials partially exchanged with strontium and barium were characterized by X-ray powder diffraction (XRD), scanning electron microscopy (SEM), and energy-dispersive analysis by X-rays (EDAX). XRD patterns of the materials were obtained using a

Rigaku ULTIMA III X-ray diffraction ($\text{CuK}\alpha$) equipped with a cross beam optics system and were used to corroborate the crystallinity of the materials. Scanning electron micrographs were obtained using a JEOL JSM-6390LV instrument while the elemental composition was obtained by employing the unit's onboard EDAX energy dispersive X-ray spectrometer. The morphologies of the samples were captured using an accelerating voltage of 5.0 kV. Samples were coated with gold to improve secondary electron emission and prevent charging. The unit cell elemental composition data was obtained with a voltage of 10.0 KV with a SUTW-Sapphire Detector.

2.2.4 Solid-State Magic Angle Spinning Nuclear Magnetic Resonance

Solid-State ^{27}Al and ^{29}Si Magic Angle Spinning Nuclear Magnetic Resonance (MAS NMR) measurements were performed on an ultra-narrow bore 19.6T magnet with a Bruker DRX NMR console where the ^{27}Al and ^{29}Si Larmor frequencies are 217.14 and 165.55 MHz, respectively, using an in-house made single resonance 4 mm MAS NMR probe. The samples were spun at ~8 kHz. The ^{31}P solid-state MAS NMR measurements were carried out on a Bruker Advance 600 MHz NMR spectrometer where the ^{31}P Larmor frequency is 242.94 MHz. A 2.5 mm Bruker MAS NMR probe was used with a sample spinning rate of 26 kHz for all ^{31}P measurements. For the ^{27}Al analyses, the chemical shifts were referenced to a saturated $\text{Al}_2(\text{SO}_4)_3$ solution. The NMR experimental parameters were recycle delay of 2 s, pulse length of 1.0 ls ($\sim\pi/10$ small angle pulse), td (the number of FID points) of 512, dwell time of 5 ls, and 128 scans for both Sr^{2+} -SAPO-34 and Ba^{2+} -SAPO-34. ^{29}Si chemical shifts were referenced to 4,4-dimethyl-4-silapentanesulfonate sodium (DSS). The NMR experimental parameters were recycle delay of 10, pulse length of 1 ls ($\sim\pi/10$ small angle pulse), td of 1024, dwell time of 5 ls, and the number

of scans ranging from 3000 to 7300 for Sr^{2+} -SAPO-34 and from 1024 to 5400 for Ba^{2+} -SAPO-34. For the ^{31}P analyses, the chemical shifts were referenced to a $\text{NH}_4\text{H}_2\text{PO}_4$ sample. The NMR experimental parameters were: recycle delay of 5 s, pulse length of 2 ls ($\sim\pi/7$ small angle pulse), τ_d of 1024, dwell time of 2 ls, and 512 scans for both Sr^{2+} -SAPO-34 and Ba^{2+} -SAPO-34.

2.2.5 Surface Area, Pore Volume and Pore-Size

Surface area, pore volume and median pore width were determined for strontium and barium partially exchanged SAPO-34 materials after each ion exchange treatment. The textural properties were estimated after evaluation of nitrogen volumetric equilibrium adsorption uptake data gathered at 77K. The corrected Horvath and Kawazoe model was used to determine the median pore width^{12, 13} and nitrogen adsorption isotherms were transformed using the t -plot method (Lippens and de Boer) to determine the contribution of the micropores to the overall surface area.¹⁴⁻¹⁶

2.2.6 Adsorption Equilibrium Isotherms

Equilibrium isotherm data were obtained using a static volumetric adsorption system (Micromeritics ASAP 2020) outfitted with turbo molecular drag pumps. Adsorbate gases used were CO_2 (Ultra High Purity Grade, Praxair), N_2 (Ultra High Purity Grade, Linde), O_2 (Ultra High Purity Grade, Linde), CH_4 (Ultra High Purity Grade, Praxair) and He (High Purity Grade, Linde). Helium was used as a backfill gas after the sorbent degassing stage and removed via ultra-high vacuum prior to adsorption tests. All samples were pre-treated in vacuum at 648 K to remove water molecules strongly bound inside the structure.¹⁷ For carbon dioxide, equilibrium tests were performed at temperatures ranging from 273 to 348 K and pressures up to 1 atm. Tests

for N₂, CH₄ and O₂ were performed only at 298 K. During the experiments, the temperature was kept constant by means of either a water bath or a heating blanket.

2.2.7 Isosteric Heat of Adsorption (ΔH_{ads})

The Clausius-Clapeyron equation (Eqn. 1) and pure component equilibrium adsorption data at different temperatures and constant surface loading were used to estimate the isosteric heats of adsorption.

$$\left(\frac{d \ln P}{d(1/T)} \right) \bigg|_{q=const} = \frac{\Delta H_{ads}}{R} \quad (2.1)$$

In this equation R is the gas constant, P is the equilibrium pressure at a particular coverage q and T is the absolute temperature.

2.2.8 DFT Calculations

To determine the sites of the metal cations and CO₂ in SAPO-34, we carried out first-principle DFT calculations. The SAPO-34 material was modeled by taking a cage-like section of the Chabazite framework unit cell as shown in Figure 2.1, the final model consisted of six Si atoms with the following atomic ratios: Si/Al = 0.25 and Si/(Al + P) = 0.14. The atoms were distributed following the Lowenstein rule (i.e., there were no Al-Al neighbors) and the surface dangling oxygen atoms were terminated with hydrogen to retain a neutral structure. All geometry optimizations were carried out using the DMol³ program of Accelrys Inc.^{18, 19} Perdew-Burke-Ernzerhof (PBE) exchange and correlation functionals were employed.²⁰ The Kohn-Sham orbitals are expanded in double numerical plus polarization (DNP) basis set. The density

functional semi-core pseudo-potential (DSPP) included in DMol³ program was employed for all optimizations.^{18, 19}

In large systems a number of low-lying unoccupied orbitals lie very close energetically to the ground state (~ 0.1 eV). In the present calculations, the fractional occupation number technique was employed,^{18, 19} where electrons are ‘smeared’ by an energy width of 0.1 eV over the orbitals around the Fermi energy. The resulting total energy may be viewed as an average over all configurations lying energetically close to the ground state of the cluster.

2.3. Results and Discussion

The results previously reported by Hernandez-Maldonado and co-workers showed that extraframework species on SAPO-34 sorbents provide effective functionalization of its working surface.⁶ After analyzing the effect of different monovalent, divalent and trivalent cations partially exchanged on SAPO-34 material, they found that strontium (Sr^{2+}) exchanged SAPO-34 was by far the best sorbent for separation of CO_2 from light gas mixtures. As stated in the introduction, the present work focuses on the implementation of M-LPIE in an attempt to enhance the CO_2 sorption behavior on Sr^{2+} -SAPO-34 and will extend the approach to prepare barium-rich SAPO-34 variants. Direct comparison of the sorbents will be made through out the discussion.

It should be mentioned that the starting Na^+ -SAPO-34 material for this study, in comparison with previously reported data,^{7, 21} has a higher sodium content. The unit cell has ca. 2.3 sodium atoms, more than twice the amount previously reported and which may account for differences in the maximum exchange levels obtained and related properties. In order to provide a normalization

baseline, the morphological, structural and adsorptive properties of the materials after each ion exchange step were compared with those of starting Na⁺-SAPO-34. The relevance of the starting material in the level of cation exchange in synthetic faujasites has been discussed by Fletcher and Townend²² and Sato et al.² and could be extended for other zeolitic materials such as ours. Notwithstanding, the properties of the Na⁺-SAPO-34 are in good agreement with other previously reported data for similar SAPOs.

The influence of cation sites in adsorption processes is exceptionally relevant for the discussion and, therefore, it is necessary to establish some relevant nomenclature before proceeding with the analysis. Cations are known to occupy four main sites within the Chabazite cages of the material as shown in Figure 2.1²³. These are: Site I located at the center of the hexagonal prism, Site II located at the center of the six-ring window, Site II' at the cavity displaced from the six-ring window and Site III located near the center of the eight-ring window.

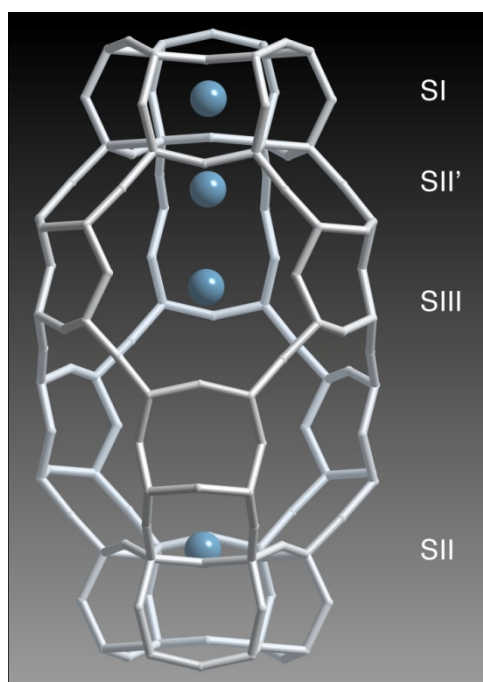


Figure 2.1. Chabazite framework with possible cation positions (large spheres).⁷ Reproduced with permission from *Ind. Eng. Chem. Res.* **2007**, *46*, 4991-5002. Copyright 2007 American Chemical Society

2.3.1 Sorbents Characterization

Figure 2.2 shows SEM micrographs for the as-prepared and ion-exchanged materials. Stage 1, 2 and 3 refers to 24, 48 and 72 hours of liquid phase ion exchange, respectively. All micrographs exhibit the typical cubic crystal characteristic of SAPO-34 based materials, with a polydispersed particle size (0.5 to 2.5 μm). They also show the effect of the ion exchange procedure after each step/stage, which consists mainly of faults in the particle outer surface and particle aggregation. Degradation of the morphology seems less prominent in the barium variants when compared to the strontium-exchanged materials.

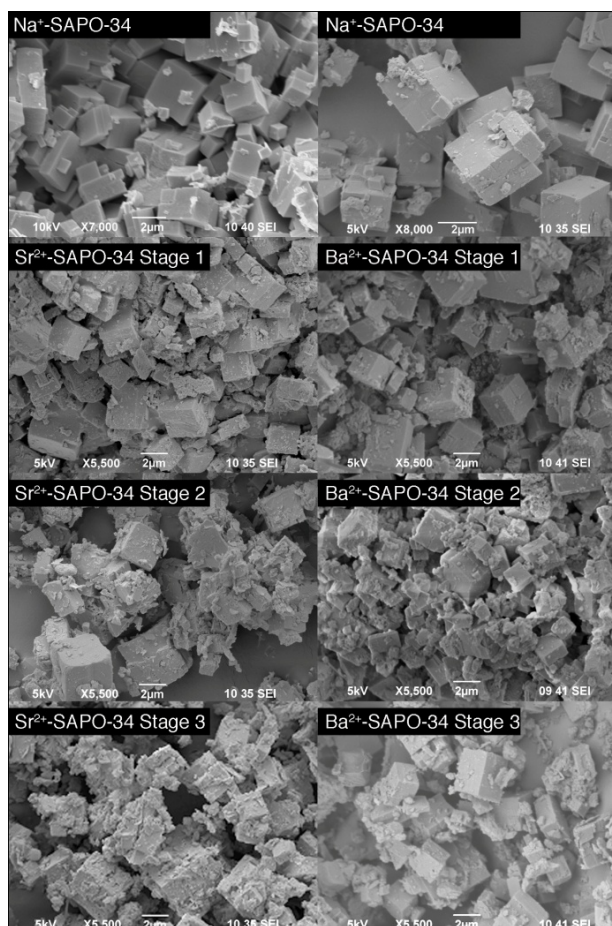


Figure 2.2. SEM micrographs of Na^+ -SAPO-34 and ion-exchanged samples. Stages 1, 2 and 3 refer to ion exchange for 24, 48 and 72 hours, respectively.

XRD patterns were gathered to analyze the materials long-range order as a function of the degree of ion exchange (see Figure 2.3). Analysis of these data showed preservation of crystallinity with some minimum changes on peak intensities when compared to those of the starting Na^+ -SAPO-34 material. These were probably caused by the ion exchange procedure, but given the small particle size exhibited by the samples, preferential orientation effects should not be discarded.

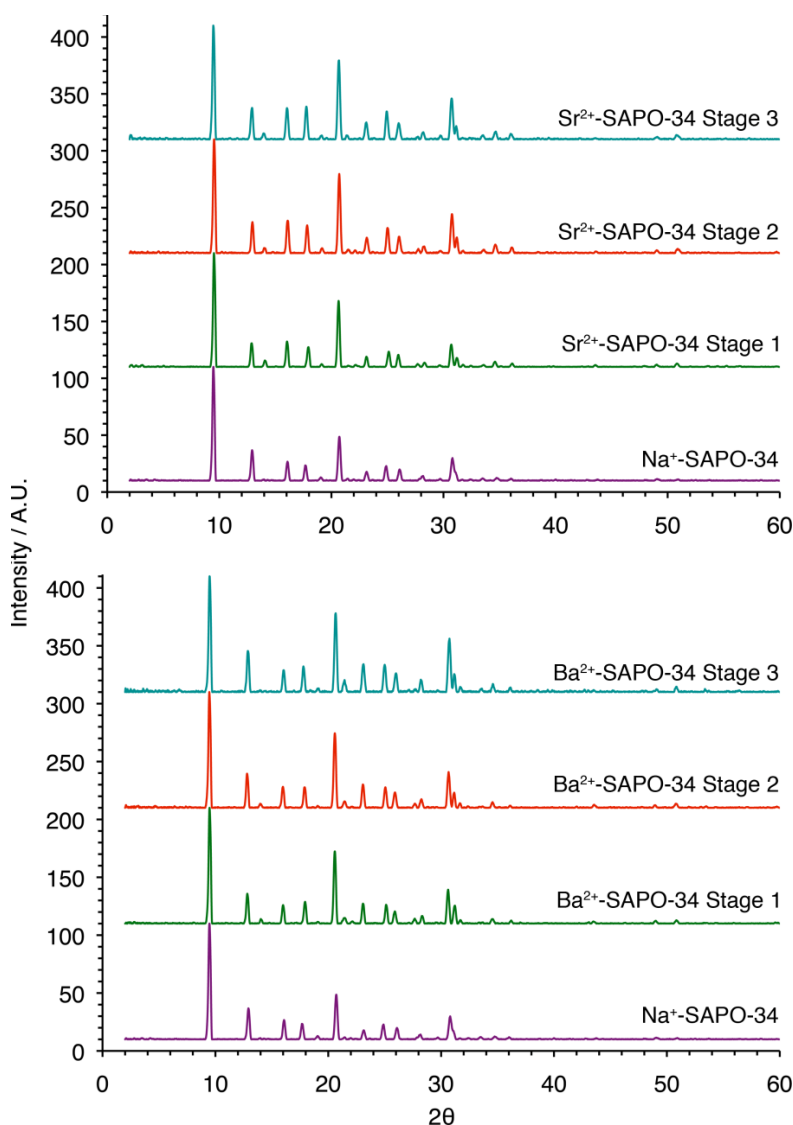


Figure 2.3. X-ray diffraction patterns for Na^+ -SAPO-34 and ion-exchanged samples. Stages 1, 2 and 3 refer to ion exchange for 24, 48 and 72 hours, respectively.

Although morphological degradation of SAPO-34 particles is evident in the SEM micrographs, XRD analysis indicated that the crystalline structure of the particles appears undamaged during the ion exchange treatments. It should be mentioned however that any short-range local coordination changes experienced by the samples would be invisible to the XRD technique and, therefore, methods such as MAS NMR should be employed to elucidate them.

MAS NMR was employed to study the environments of Al, Si and P tetrahedra before and after each LPIE stage. Figs. 4 and 5 summarize the ^{27}Al , ^{29}Si and ^{31}P MAS NMR spectra for all the sorbent variants, including Na^+ -SAPO-34. All the materials ^{27}Al NMR spectra data exhibited a strong resonance peak at ca. 48 ppm, indicating that aluminum is mainly tetrahedrally (Al^{IV}) coordinated in the zeolitic framework.²⁴ The small peaks shown in the 60 – 90 ppm region are probably resonance contributions from other tetrahedral aluminum families. Although both the Sr^{2+} and Ba^{2+} sorbents exhibited changes in the 60 – 90 ppm region, these were more prominent in the former sorbent variant.

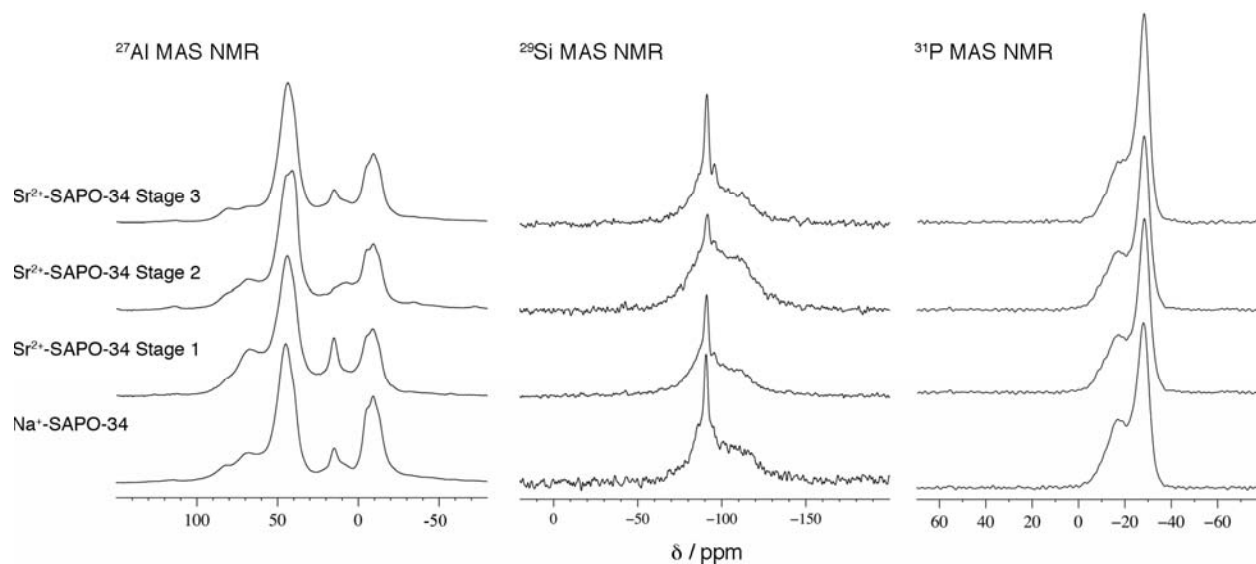


Figure 2.4. ^{27}Al and ^{29}Si MAS NMR spectra for Na^+ -SAPO-34 and partially exchanged Sr^{2+} -SAPO-34 samples. Stages 1, 2 and 3 refer to ion exchange for 24, 48 and 72 hours, respectively.

The ^{27}Al spectra also exhibited a peak at approximately -10 ppm and should correspond to the presence of octahedral aluminum species (Al^{VI}) resulting probably from thermal treatment to remove the TEAOH.²⁴ However, the Al^{VI} peak remains almost unchanged after each ion exchange stage. The peak observed at 12 ppm is attributed to aluminum with penta- or hexa-coordination,^{25, 26} probably resulting from interaction with water molecules. For Sr^{2+} -SAPO-34, the intensity of this peak decreases and is broadened after the ion exchange procedure as a result of the interaction of water with AlO_4 tetrahedra.^{2, 27}

Figures 2.4 and 2.5 also include the ^{29}Si MAS NMR spectra for the sorbents presented in this study. The peak at -90 ppm is associated to the $\text{Si}(4\text{Al})$ and also to the presence of traces of water adsorbed on $\text{Si}(\text{OH})\text{Al}$ groups.²⁴ The spectra also show a band at ca. -95 ppm after each ion exchange stage, probably corresponding to $\text{Si}(3\text{Al})$.²⁴

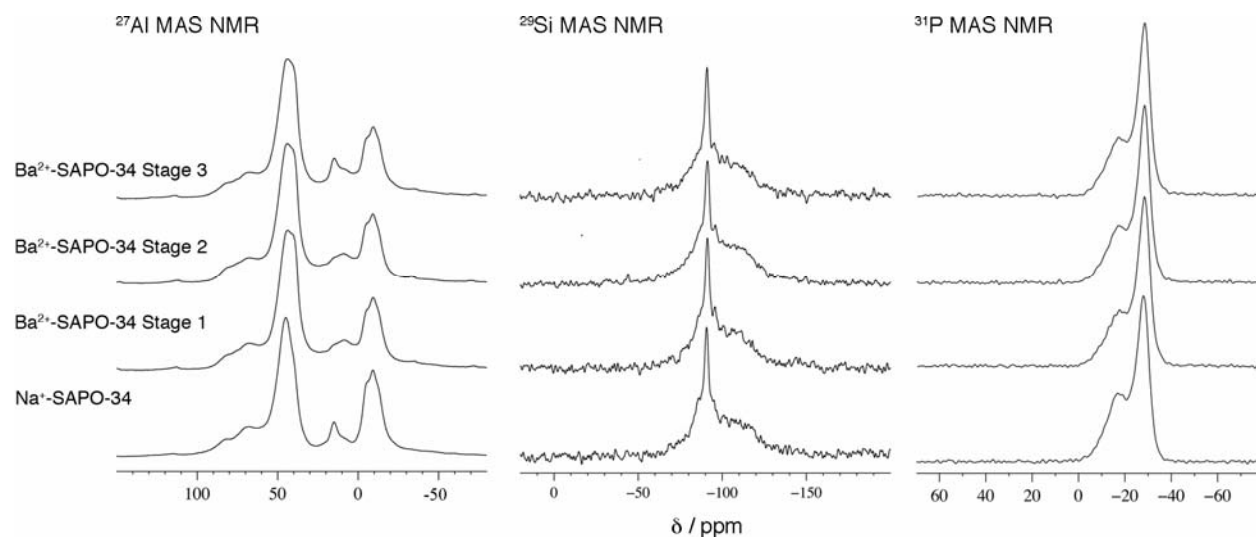


Figure 2.5. ^{27}Al and ^{29}Si MAS NMR spectra for Na^+ -SAPO-34 and partially exchanged Ba^{2+} -SAPO-34 of samples. Stages 1, 2 and 3 refer to ion exchange for 24, 48 and 72 hours, respectively.

When coupled to the ^{27}Al NMR results, the appearance of silicon species coordinated to a sole Al atom probably suggests the presence of a small fraction of local amorphous species. For

the case of strontium-exchanged sorbents the intensity of the -90 ppm peak decreases after each ion exchange stage accompanied by broadening of the spectra in the -100 to -130 ppm region. It should be mentioned that although there is some peak broadening in the ^{27}Al NMR spectra for the barium-containing samples, it is not as severe as in the case of the strontium variants. ^{31}P MAS NMR spectra for the ion-exchanged samples and the basis material (see Figures 4 and 5) show a high resonance peak at approximately -28 ppm, assigned to tetrahedrally coordinated phosphorous atoms bounded to four aluminum atoms $\text{P}(\text{OAl})_4$.^{26, 28-30} A weak resonance peak observed at -18 ppm could be attributed to phosphorous atoms, which are probably coordinated to water molecules instead of aluminum atoms.^{26, 30} For strontium ion exchanged materials, the -18 ppm peak intensity appears to weaken while the -28 ppm signal gets stronger, probably indicating that the species associated to the former peak are been transformed into additional framework $\text{P}(\text{OAl})_4$ units.

In general, it appears that these NMR observations are the result of the detemplation of the samples after synthesis to produce Na^+ -SAPO-34 and not due to the multi-stage ion exchange process. The observations, however, could correlate to local structural changes that might impact the materials overall performance as CO_2 adsorbents.

Table 2.1 summarizes the unit cell composition for all the materials studied. The unit cell composition of the materials was determined by EDAX and we should stress at this point of the discussion that the technique gives semi-quantitative information of the surface composition, which is still quite useful to denote the presence of the exchanged cation. To account for any potential variability, measurements were performed on six different spots.

Table 2.1. Unit cell composition, surface area, pore volume and median pore width of Na⁺-SAPO-34 and ion-exchanged Sr²⁺-SAPO-34 and Ba²⁺-SAPO-34 materials.

Material	Unit Cell Composition	Micropore Surface Area (m ² /g)	External Surface Area (m ² /g)	Pore Volume HK (cm ³ /g)	Pore Size: median pore width-HK (Å)
Na ⁺ -SAPO-34	Na _{2.30} H _{3.37} [Si _{4.10} Al _{18.74} P _{13.16} O ₇₂]	572	48	0.221	5.2
Sr ²⁺ -SAPO-34 Stage 1 ^a	Sr _{0.64} Na _{0.40} H _{3.24} [Si _{4.30} Al _{18.31} P _{13.39} O ₇₂]	611	44	0.234	3.7
Sr ²⁺ -SAPO-34 Stage 2 ^a	Sr _{0.68} Na _{0.47} H _{3.38} [Si _{4.18} Al _{18.51} P _{13.31} O ₇₂]	533	23	0.198	3.7
Sr ²⁺ -SAPO-34 Stage 3 ^a	Sr _{0.69} Na _{0.40} H _{3.52} [Si _{4.22} Al _{18.54} P _{13.24} O ₇₂]	457	18	0.170	3.7
Ba ²⁺ -SAPO-34 Stage 1 ^a	Ba _{1.01} Na _{0.67} H _{3.82} [Si _{4.28} Al _{19.11} P _{12.61} O ₇₂]	502	19	0.186	3.7
Ba ²⁺ -SAPO-34 Stage 2 ^a	Ba _{1.12} Na _{0.63} H _{3.83} [Si _{4.16} Al _{19.27} P _{12.57} O ₇₂]	458	49	0.182	3.7
Ba ²⁺ -SAPO-34 Stage 3 ^a	Ba _{1.20} Na _{0.60} H _{3.68} [Si _{4.18} Al _{19.25} P _{12.58} O ₇₂]	533	51	0.210	3.7

^a Stages 1, 2 and 3 refer to ion exchange for 24, 48 and 72 hours, respectively.

The chemical composition analysis of Sr^{2+} -SAPO 34 materials indicates that after the first stage of LPIE, 82% of the sodium cations in the structure were exchanged for strontium. For the subsequent LPIE stages, the amount of strontium in the unit cell remained un-changed, possibly indicating that some of the Na^+ or H^+ species were not easily accessible to the incoming cation. This could be due to the effective location of the original cations, probably occupying the hexagonal prism (Site I) in a predominant fashion, and/or solvation problems. It would be rather difficult for strontium centers to occupy SI sites due to its size and charge distribution and similar results have been observed by Sato et al. for ion exchanged Y zeolites.²

For barium-exchanged materials, the chemical composition analysis indicates that the amount of barium increased significantly relative to the first ion exchange stage. Contrary to the behavior observed in strontium materials, the amount of barium kept increasing after each stage of the ion exchange cycle. However, the exchange achieved only 74% of the theoretical total capacity. This could be again due to exchangeable sodium availability in the structure. In general, the chemical composition results indicate that ion-exchange did not approach 100% completion, but could be considered close to the maximum cation loading possible given the limitations of the aqueous LPIE technique.³¹ In addition, these results corroborate the long-range stability of the SAPO crystalline framework as previously concluded from the XRD data.

An interesting fact observed for both exchanged materials variants is that it seems that the only extraframework species available for exchange were the sodium centers since the acid sites available in the material remain un-changed (see Table 2.1). This could be attributable to the position of the hydrogen ions, probably located in the hexagonal prisms (SI) as in the case of the remaining sodium in the structure. Also, one should consider that equilibrium of solvated species

involved during ion exchange in the liquid phase might retain hydrogen inside the structure of the material.

2.3.2 Surface Area, Pore Volume and Pore-Size Determination

For strontium-exchanged materials the total surface area and pore volume varied considerably after each stage (see Table 2.1). A similar behavior has been observed in ion exchanged Y zeolites.² The pore volume is expected to decrease after each stage of ion exchange as a result of the incorporation of the in-going cations, which in this particular case are larger than the sodium centers. Sodium and strontium have atomic radii of 1.80 Å and 2.00 Å, respectively,³² and both will exhibit different coordination preferences due to differences in charge distribution. The latter will determine the final position of the cations within the framework cavities and, therefore, influence the porosimetry characteristics. For instance, the observed increase in pore volume after the first ion exchange stage is plausibly a result of the preferential occupancy of less prominent sites (e.g., SII vs. SII') within the structure by extra-framework species, resulting this at the same time in more void space. Another factor that plays a crucial role in the textural properties of the sorbents is the extent of the particle faults resulting from the ion exchange procedure. For the strontium-exchanged variants the SEM data (see Figure 2.2) clearly indicates pitting and agglomeration effects. In fact, the external surface area values reported in Table 2.1 correlate well with the microscopy observations. That is, upon formation of agglomerates the external surface area should decrease.

In the case of barium exchange, both the surface area and pore volume gradually decreased after the first and second stage of ion exchange. Again, this was expected given the differences in cation size between the outgoing and incoming species (1.80 vs. 2.15 Å). For the third stage,

however, the surface area increased considerably and, just like in the strontium case, this could be attributed to the final cation site position.

Another variable that should be considered for interpretation of the textural properties is the presence of faults in the short-range local structure features. As suggested by the MAS NMR results (see Figs. 2.4 and 2.5), the multiple LPIE process induced coordination changes that could have produced effective pore blocking. Since the sorption probe molecule (i.e., Nitrogen) used to estimate the textural properties, has dimensions already within the range of the SAPO-34 average pore window width, any faults within the crystal lattice could inhibit free diffusion. Therefore resulting this in variations in the porosimetry characteristics.

2.3.3 Carbon Dioxide Pure Component Equilibrium Adsorption

As stated before, the characterization results indicate that for the most part the sorbents long-range crystalline properties were preserved after each ion exchange stage. However, the same cannot be said about the adsorption properties (Figure 2.6). Still, when compared to the results previously obtained by Rivera-Ramos and Hernandez-Maldonado,⁶ the shape of the isotherms still correlates with strong sorbent-sorbate interactions for both the strontium and barium partially exchanged materials. Given the possible cation sites distribution available within the SAPO unit cell, such strong interactions are probably due in part to cations occupying SII and/or SII' sites, which are quite exposed to the main unit cell cavity. Occupancy of SI will preclude CO₂ from undergoing interactions with the cation while occupancy of SIII will result in an effective pore blockage. The latter will greatly reduce the sorbent capacity as observed before by Hernandez-Maldonado and co-workers.⁷

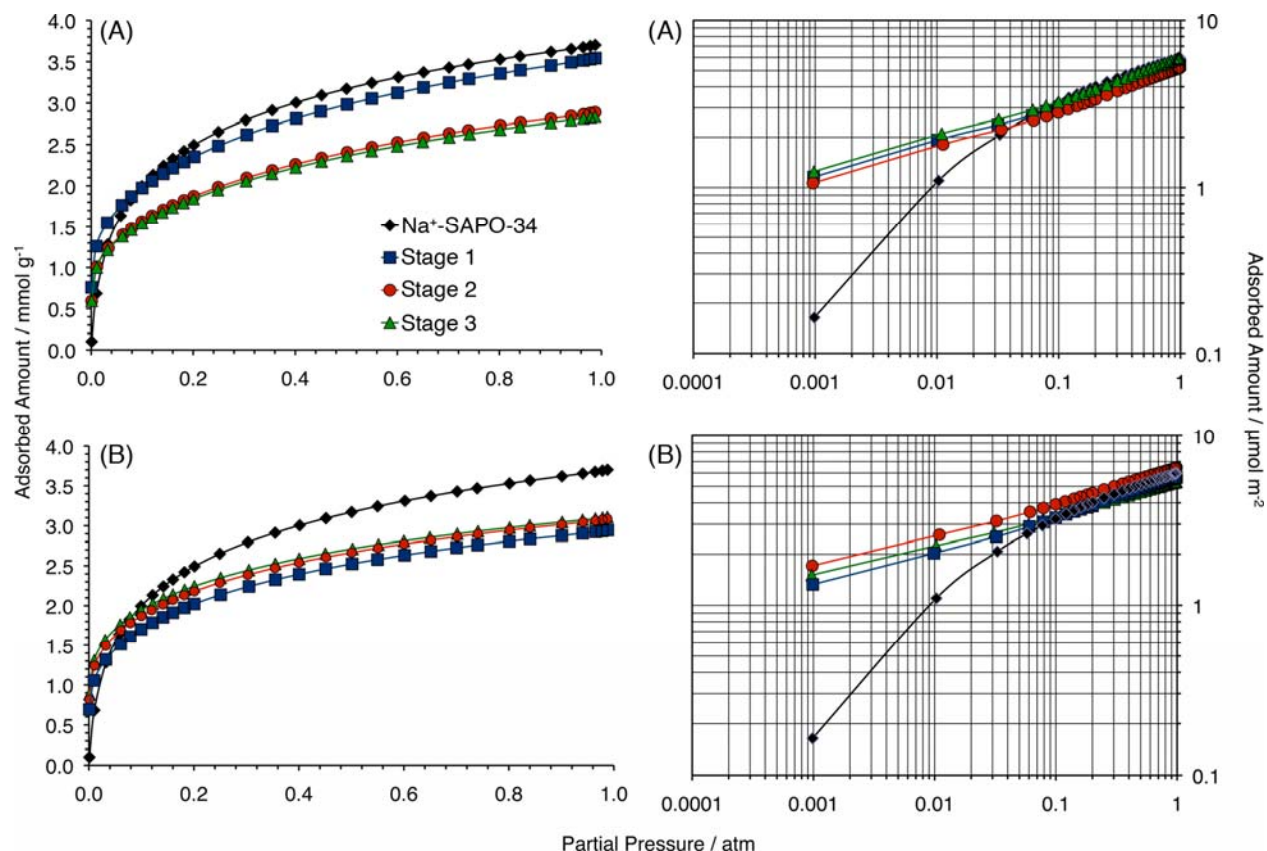


Figure 2.6. CO_2 adsorption isotherms (normal and logarithm scales) for Na^{+} -SAPO-34 and ion-exchanged A) Sr^{2+} -SAPO-34 and B) Ba^{2+} -SAPO-34 samples. Stages 1, 2 and 3 refer to ion exchange for 24, 48 and 72 hours, respectively.

Table 2.2 presents the calculated binding energy of Sr^{2+} at four possible sites in SAPO-34 (see Figure 2.1 for level reference). Our computational results indicate the SII' site as the energetically most favorable, with a binding energy of 506 kJ/mol.

Table 2.2. Calculated Sr^{2+} binding energy (E_{bind}) SAPO-34 material at four possible sites (see Figure 2.1 for sites reference).

Cation Site	S I	S II' = S II	S III
E_{bind} (kJ/mol)	418	506	397

For strontium partially exchanged materials the CO₂ adsorbed amount decreases considerably after the second ion exchange treatment stage (Figure 2.6). After the third stage, the CO₂ adsorption capacity of the material remains unchanged with respect to the second stage. The decrease in the CO₂ uptake capacity after each ion exchange stage could be ascribed to a decrease in cationic density within supercages. As previously discussed in this paper the relevance of the cations position and distribution among extra-framework sites should correlate to the adsorption behavior in the material. In other words, additional cations in the structure will limit effective access to the supercages, producing partial blockage of the SAPO-34 material cages, this in agreement with results obtained by Hammoudi et al.¹ for ion exchanged X zeolites (see Appendix A). Another possible explanation to the observed adsorption behavior for this case is the effect brought by changes in the textural properties. Figure 2.6 also includes isotherms normalized by the exchanged-sorbent surface area, which for the strontium-exchanged sorbent case points to a slight increase in adsorption amounts after each ion exchange stage.

Barium-exchanged materials also presented a high CO₂ adsorption capacity, comparable to the ones observed for Sr²⁺SAPO-34 sorbent after the first ion exchange stage. However, for Ba²⁺-SAPO-34 exchanged materials the CO₂ adsorbed amount did increase with an increase in cation content. After the third ion exchange stage, the sorbent was capable of adsorbing ca. 0.88 mmoles of CO₂ per gram of activated solid at 10⁻³ atm. Taking into account the unit cell data reported in Table 2.1 this uptake amount corresponds to about two (2) CO₂ molecules per unit cell, which matches well with the Ba²⁺ content and evidences how efficient the adsorbent is at low partial pressures. Although some morphological degradation was observed after the liquid phase ion exchange stages (Figure 2.2), it seems that it has little if no influence on the material ultimate performance at low partial pressures. At high partial pressures barium exchanged

materials present a lower saturation level when compared to the Stage 1 strontium counterpart and this could be consequence of the cationic size differences and the resulting effective pore volume. In addition, the CO₂ sorption conformation should affect the effective pore access at higher pressures.

To identify the CO₂ adsorption conformation by means of first-principles calculations, geometrical optimizations were carried out beginning with a variety of different conformations. Figure 2.7 shows the CO₂--Sr²⁺-SAPO-34 structures before and after geometry optimization. In the optimized structure CO₂--Sr²⁺-SAPO-34, CO₂ binds end-on to the metal cation at carbon-dioxide oxygen-Sr distance of 2.6 Å. A similar conformation was found to be the energetically lowest for the other metal cations (Na⁺ and Ba²⁺).

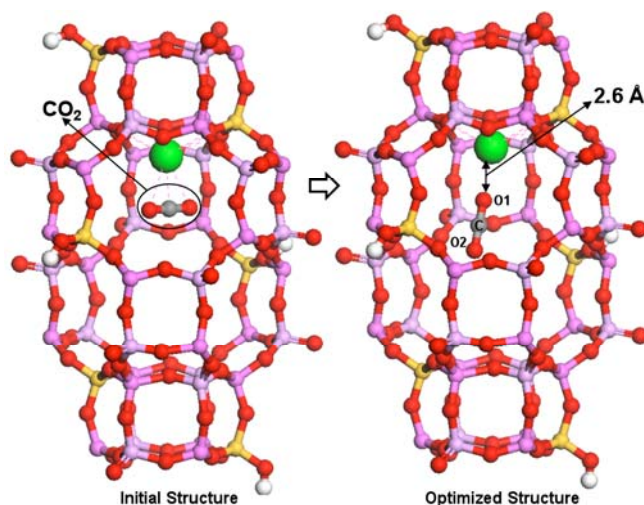


Figure 2.7. CO₂--Sr²⁺-SAPO-34 structure before (initial structure) and after (optimized structure) geometrical optimization.

At this point it is of utmost importance to state that both strontium- and barium-exchanged sorbents materials are ideal for ultra-purification applications due to the strong interactions presented by these materials towards CO₂. An attempt to quantify and explain these interactions will be made next.

2.3.4 CO₂ Heat of Adsorption in Mⁿ⁺-SAPO-34

Isosteric heats of adsorption were calculated for the materials after each ion exchange stage to evaluate the strength of adsorbate/adsorbent interactions (see Figure 2.8). It should be mentioned first that all the samples displayed isotherms that follow the classic physisorption profile, where an increase in temperature results in a decrease in uptake amounts at any given pressure (results not shown here). As such, it is expected that the estimated isosteric heats should correlate with this observation.

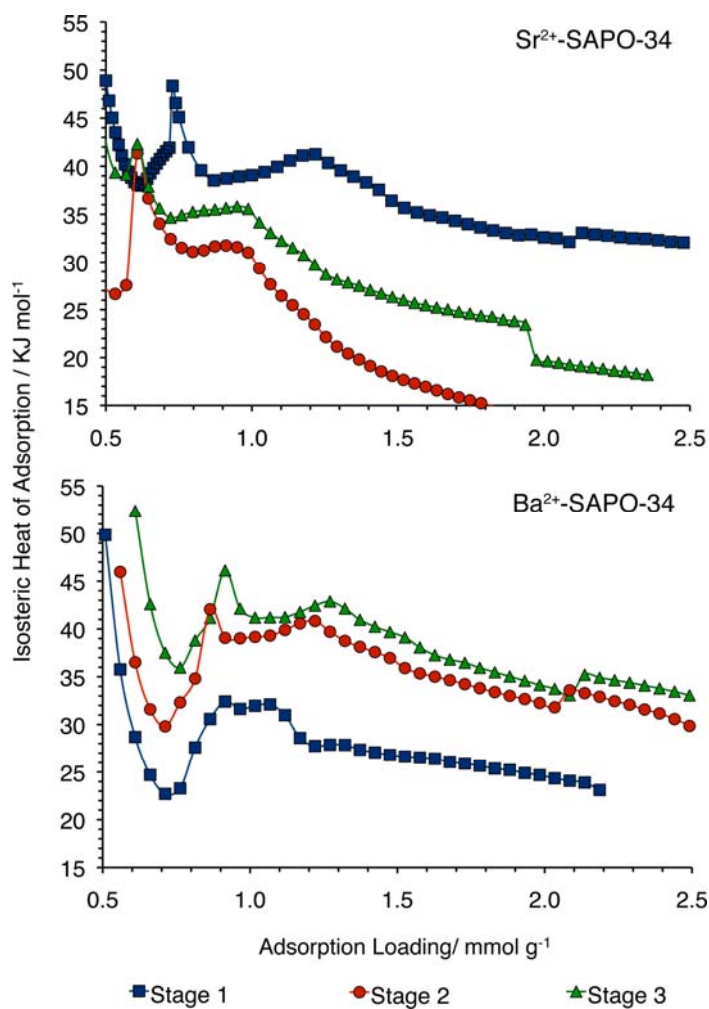


Figure 2.8. Isosteric heats of adsorption of CO₂ for partially exchanged Sr²⁺SAPO-34 and Ba²⁺-SAPO-34 sorbents. Stages 1, 2 and 3 refer to ion exchange for 24, 48 and 72 hours, respectively.

For strontium partially exchanged materials, all the isosteric heat profiles are typical of heterogeneous surfaces as discussed by Hernandez-Maldonado and co-workers elsewhere,^{6, 7} The maximum heat during CO₂ loading in Stage 1 Sr²⁺-SAPO-34 samples occurs at ca. 1.8 CO₂ molecules per unit cell, which does not correlate with the strontium loading as estimated by EDAX. One possible explanation could be the presence of additional sodium ions as compared to the material originally prepared by Hernandez-Maldonado and co-workers.⁶ Since the data shown in Table 2.1 for the strontium variants suggest that the unit cell composition remains virtually un-changed after each LPIE stage, the observed decrease in average isosteric heat (see Figure 2.8) could then be a result of textural modifications. A similar behavior has been reported in the literature for X zeolites.^{1, 33} The continuous decrease in isosteric heat of adsorption upon introduction of Sr²⁺ cations could be attributable to a progressive weakening of electrostatic fields present within the zeolitic cavities, which is supported by the results obtained for CO₂ adsorption capacity after the sequential LPIE treatment.

The heat of adsorption for barium partially exchanged materials increased as a function of the degree of ion exchange. This is consistent with the results previously discussed for the characterization and adsorptive properties of the material. In addition, the maximum heat of adsorption for Stage 2 and Stage 3 Ba²⁺-SAPO-34 materials occurs when the loading correspond to ca. 1.9 and 2.0 CO₂ molecules per unit cell, respectively. Using the unit cell data shown in Table 2.1 these numbers translate to about 1.7 CO₂ molecules per Ba²⁺ cation, which evidences that the increase in adsorption amount presented in Figure 2.6 actually comes from the increase in barium loading after each LPIE stage. For the first stage the Isosteric heat profile does not showcase a well define maximum and this could be due to the presence of exposed sodium cations which might as well interact with CO₂ already adsorbed in barium sites.

Although the observed isosteric heat of adsorption profiles seem to be a reflection of changes in textural properties, it is quite difficult to elucidate the nature of the sorbate-sorbent interaction from such data. To address this we employed first-principle calculations to estimate the sorbate-sorbent binding energies and the associated Mulliken charges. Table 2.3 collects the adsorption energy of CO₂ on Na⁺-, Sr²⁺-, and Ba²⁺-SAPO-34 and Mulliken gross atomic charge on the respective metal cations and CO₂ atoms.

Table 2.3. Calculated CO₂ adsorption energy (E_{ads}) on Na⁺-, Sr²⁺-, and Ba²⁺-SAPO-34 and Mulliken gross atomic charge on the metal cation and CO₂ atoms.

Material	E_{ads} (kJ/mol)	Mulliken gross atomic charge			
		Metal	C	O1	O2
Na ⁺ -SAPO-34	30.12	+0.78	+0.58	-0.31	-0.25
Ba ²⁺ -SAPO-34	44.56	+1.54	+0.61	-0.38	-0.21
Sr ²⁺ -SAPO-34	52.30	+1.48	+0.62	-0.40	-0.19
CO ₂ in gas phase			+0.57	-0.28	-0.28

The calculated adsorption energy of CO₂ on Na⁺-SAPO-34 is 30.12 kJ/mol in agreement with the experimental value (ca. ~35 kJ/mol) reported by Hernandez-Maldonado.⁶ The corresponding values for Ba²⁺- and Sr²⁺-SAPO-34 are 44.56 and 52.30 kJ/mol, respectively, which match very well with the average Isosteric heats presented in Figure 2.8. This relative large adsorption energy of CO₂ on the framework (nearly five times greater than a van der Waals type interaction, ca. 10 kJ/mol) arises from a chemical bond of ionic character. The positively charged metal cations polarize the CO₂ charge, allowing a relatively strong electrostatic interaction. The Mulliken gross atomic charge of the two oxygen atoms in CO₂ in gas phase is ca. -0.28, while the corresponding value for the CO₂ oxygen atom (O1) in direct contact with Sr²⁺ in SAPO-34

(see Figure 2.7) is ca. -0.40, while that of the second oxygen atom (O2) is ca. -0.19. Additional calculations of the binding energy for CO₂ on Srⁿ⁺ ($n=0, 1, 2$) in gas phase confirm the ionic character of the chemical bond between CO₂ and the metal cation on SAPO-34. Table 2.4 collects the binding energy and the Mulliken gross atomic charge for the hypothetical CO₂-Sr⁺ and CO₂-Sr²⁺ complexes in gas phase. The binding energies of CO₂-Sr⁺ and CO₂-Sr²⁺ are 35.98 and 125.93 kJ/mol, respectively. The Mulliken gross atomic charges on the Sr⁺ and Sr²⁺ cations are +0.96 and +1.87, respectively. These results show the direct relationship between the charge on the metal cation and the adsorption energy, indicating that the interaction between CO₂ and the metal cations is predominantly a bond of ionic character.

Table 2.4. Calculated CO₂ adsorption energy (E_{ads}) on Srⁿ⁺ ion ($n=1, 2$) in gas phase and Mulliken gross atomic charge on the constituent atoms.

Complex	E_{ads} (kJ/mol)	Mulliken gross atomic charge			
		Metal	C	O1	O2
CO ₂ -Sr ⁺	35.98	+0.96	+0.61	-0.40	-0.17
CO ₂ -Sr ²⁺	125.93	+1.87	+0.68	-0.49	-0.06

A detailed analysis of the Mulliken gross atomic charges on the metal cations, both in the hypothetical gas phase complexes and in SAPO-34, indicates that the Chabazite silicoaluminophosphate framework acts to donate negative charges to the adsorbed metal cations. The charge donation leads to reduction of the positive charge on the metal cation, which results in a lower CO₂ adsorption energy. The analysis indicates that it is experimentally possible to design an improved system for ultra-deep removal of CO₂ by varying the silicoaluminophosphate composition in the Chabazite framework to control the CO₂ adsorption capacity.

2.3.5 CO₂, N₂, O₂ and CH₄ Pure Component Equilibrium Adsorption in Sr²⁺-SAPO-34 and Ba²⁺-SAPO-34

The aforementioned sorbent variants are aimed at applications involving purification of light gases, particularly the removal of CO₂ from air and natural gas, respectively. Figure 2.9 shows pure component adsorption isotherms for CO₂, N₂, O₂ and CH₄ in Sr²⁺-SAPO-34 and Ba²⁺-SAPO-34 materials at 298K.

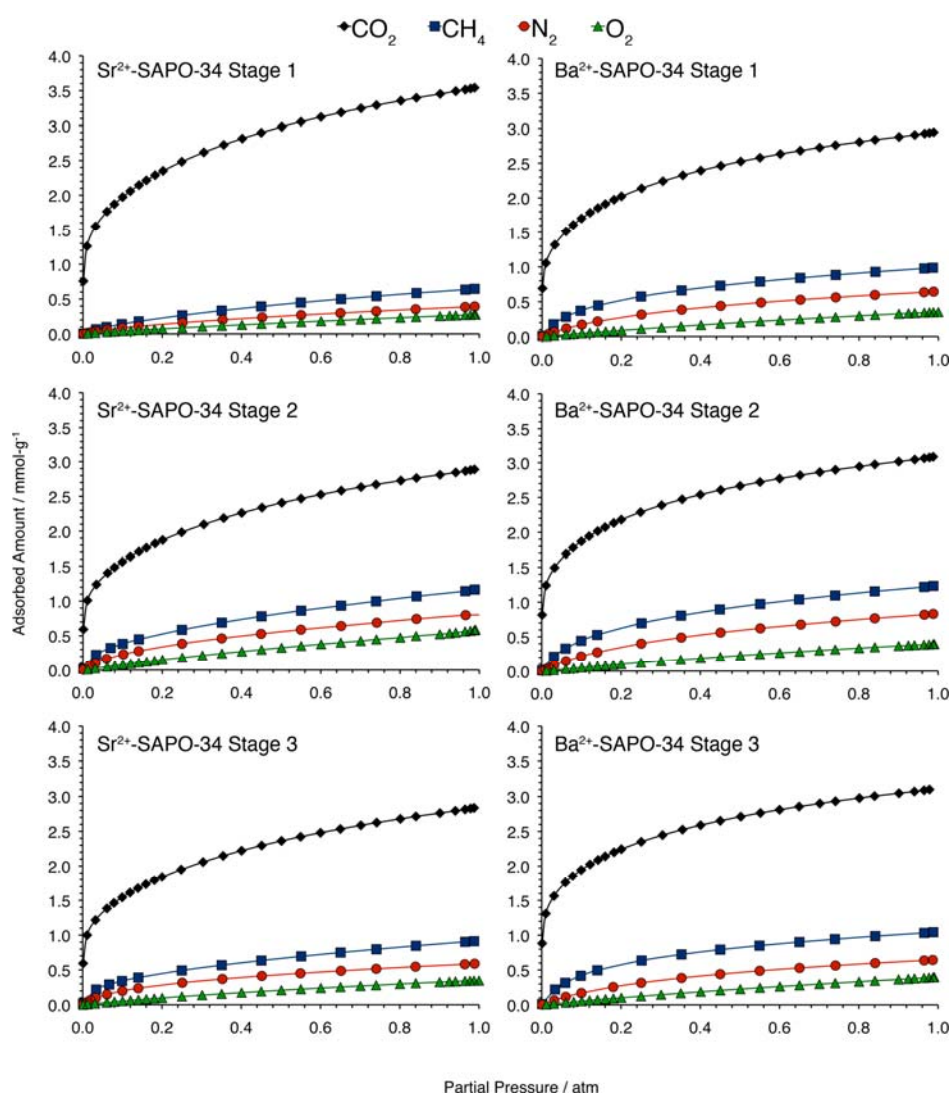


Figure 2.9. Pure component adsorption isotherms for CO₂, CH₄, N₂ and O₂ on partially exchanged Sr²⁺-SAPO-34 and Ba²⁺-SAPO-34 at 298 K. Stages 1, 2 and 3 refer to ion exchange for 24, 48 and 72 hours, respectively.

In general, all sorbents variants displayed a remarkable selectivity towards CO₂ at all partial pressures. A discussion on the strontium cation selectivity and interaction towards CO₂ has been presented before by Hernandez-Maldonado and co-workers.⁶ Their studies determined that the high selectivity towards CO₂ could only be attributed to its relatively strong quadrupole moment interaction with the divalent cation electric field. CO₂ has a strong quadrupole moment ($-4.3 \times 10^{-26} \text{ erg}^{1/2}\text{cm}^{5/2}$)³², which is 3 times greater than that of N₂ and one order of magnitude larger than that of O₂. On the other hand, CH₄ does not exhibit a quadrupole moment and its relatively low uptake is due to typical Lennard-Jones type interactions. Furthermore, Sr²⁺-SAPO-34 was pelletized (see Appendix B) and tested in NASA facilities. Breakthrough curves were obtained and Sr²⁺SAPO-34 demonstrated superior performance (results not shown in this dissertation).

2.4. Conclusions

Experiments have shown that the amount of extra-framework Sr²⁺ and Ba²⁺ cations in the SAPO-34 materials increases after multi-step ion exchange, being more predominant in the latter case. While preservation of the crystalline structure was observed during XRD analysis, there are some minimal changes within the short-range local structure. MAS-NMR tests suggested possible damage of the local crystal structure from the detemplation of the original material, but none from the ion exchange process. Single gas adsorption analyses, however, resulted in superior CO₂ adsorption capacity and selectivity for both sorbent variants. Experimental results and DFT studies indicate that strontium and barium cations are preferentially located in Site II' extra-framework positions, which allows for the development of high interaction with CO₂ molecules. It should be mentioned that a Mulliken gross atomic charge analysis suggests that a

change in SAPO framework atomic composition should impact the material adsorption performance considerably.

2.5. Literature Cited

1. Hammoudi, H.; Bendenia, S.; Marouf-Khelifa, K.; Marouf, R.; Schott, J.; Khelifa, A., Effect of the Binary and Ternary Exchanges on Crystallinity and Textural Properties of X Zeolites. *Micropor. Mesopor. Mat.* **2008**, 113, (1-3), 343-351.
2. Sato, K.; Nishimura, Y.; Matsubayashi, N.; Imamura, M.; Shimada, H., Structural Changes of Y Zeolites During Ion Exchange Treatment: Effects of Si/Al Ratio of the Starting NaY. *Micropor. Mesopor. Mat.* **2003**, 59, (2-3), 133-146.
3. Amari, D.; Ginoux, J. L.; Bonnetain, L., Textural Damage of Cation-Exchanged LTA Zeolites Studied by Gas-Adsorption. *Zeolites* **1994**, 14, (1), 58-64.
4. Fichtnerschmittler, H.; Lutz, W.; Amin, S.; Dyer, A.; Wark, M., Hydrothermal Damage of Ion-Exchanged A-type Zeolite Cation-Directed Mechanism of Phase-Transformation. *Zeolites* **1992**, 12, (6), 750-755.
5. Lok, B. M.; Messina, C. A.; Patton, R. L.; Gajek, R. T.; Cannan, T. R.; Flanigen, E. M. Crystalline Silicoaluminophosphates. 1984.
6. Rivera-Ramos, M. E.; Ruiz-Mercado, G. J.; Hernandez-Maldonado, A. J., Separation of CO₂ from Light Gas Mixtures using Ion-Exchanged Silicoaluminophosphate Nanoporous Sorbents. *Ind. Eng. Chem. Res.* **2008**, 47, (15), 5602-5610.
7. Rivera-Ramos, M. E.; Hernandez-Maldonado, A. J., Adsorption of N₂ and CH₄ by Ion-Exchanged Silicoaluminophosphate Nanoporous Sorbents: Interaction with Monovalent, Divalent, and Trivalent Cations. *Ind. Eng. Chem. Res.* **2007**, 46, (14), 4991-5002.
8. Vomscheid, R.; Briend, M.; Peltre, M. J.; Man, P. P.; Barthomeuf, D., The Role of the Template in Directing the Si Distribution in SAPO Zeolites. *J. Phys. Chem.* **1994**, 98, (38), 9614-9618.
9. Briend, M.; Vomscheid, R.; Peltre, M. J.; Man, P. P.; Barthomeuf, D., Influence of the Choice of the Template on the Short-Term and Long-Term Stability of SAPO-34 Zeolite. *J. Phys. Chem.* **1995**, 99, (20), 8270-8276.
10. Dyer, A., Ion-Exchange Capacity. *Micropor. Mesopor. Mat.* **1998**, 22, (4-6), 543-545.
11. Barros, M.; Araujo, I. F.; Arroyo, P. A.; Sousa-Aguiar, E. F.; Tavares, C. R. G. In *Multicomponent Ion Exchange Isotherms in NaX Zeolite*, Santa Fe, Argentina, Sep 16-20, 2001; Santa Fe, Argentina, 2001; pp 339-344.
12. Horvath, G.; Kawazoe, K., Method for the Calculation of Effective Pore Size Distribution in Molecular-Sieve Carbon. *J. Chem. Eng. Jpn.* **1983**, 16, (6), 470-475.
13. Rege, S. U.; Yang, R. T., Corrected Horvath-Kawazoe Equations for Pore-Size Distribution. *AIChE J.* **2000**, 46, (4), 734-750.

14. Lippens, B. C.; de Boer, J. H., Studies on Pore Systems in Catalysts V. The t-Method. *J. Catal.* **1965**, 4, (3), 319-323.
15. de Boer, J. H.; Linsen, B. G.; Osinga, T. J., Studies on Pore Systems in Catalysts VI. The Universal t-Curve. *J. Catal.* **1965**, 4, (6), 643-648.
16. de Boer, J. H.; Linsen, B. G.; van der Plas, T.; Zondervan, G. J., Studies on Pore Systems in Catalysts VII. Description of the Pore Dimensions of Carbon Blacks by the t-Method. *J. Catal.* **1965**, 4, (6), 649-653.
17. Hutson, N. D.; Reisner, B. A.; Yang, R. T.; Toby, B. H., Silver Ion-Exchanged Zeolites Y, X, and Low-Silica X: Observations of Thermally Induced Cation/Cluster Migration and the Resulting Effects on the Equilibrium Adsorption of Nitrogen. *Chem. Mater.* **2000**, 12, (10), 3020-3031.
18. Delley, B., An All-Electron Numerical Method for Solving the Local Density Functional for Polyatomic Molecules. *J. Chem. Phys.* **1990**, 92, (1), 508-517.
19. Delley, B., From Molecules to Solids with the DMol³ Approach. *J. Chem. Phys.* **2000**, 113, (18), 7756-7764.
20. Perdew, J. P.; Burke, K.; Ernzerhof, M., Generalized Gradient Approximation Made Simple. *Phys. Rev. Lett.* **1996**, 77, (18), 3865.
21. Maple, M. J.; Williams, C. D., Separating Nitrogen/Methane on Zeolite-Like Molecular Sieves. *Micropor. Mesopor. Mat.* **2008**, 111, (1-3), 627-631.
22. Fletcher, P.; Townsend, R. P., Exchange of Ammonium and Sodium-Ions in Synthetic Faujasites. *J. Chem. Soc. Farad. T. 1* **1982**, 78, 1741-1753.
23. Djieugoue, M. A.; Prakash, A. M.; Kevan, L., Electron Spin Resonance and Electron Spin Echo Modulation Studies on Reducibility, Location, and Adsorbate Interactions of N(I) in Ni(II)-Exchanged SAPO-34. *J. Phys. Chem. B* **1998**, 102, (22), 4386-4391.
24. Hunger, M.; Brunner, E., NMR Spectroscopy. *Mol. Sieves* **2004**, 4, 201-293.
25. Vistad, O. B.; Akporiaye, D. E.; Taulelle, F.; Lillerud, K. P., In Situ NMR of SAPO-34 Crystallization. *Chem. Mater.* **2003**, 15, (8), 1639-1649.
26. Buchholz, A.; Wang, W.; Xu, M.; Arnold, A.; Hunger, M., Thermal stability and dehydroxylation of Brønsted acid sites in silicoaluminophosphates H-SAPO-11, H-SAPO-18, H-SAPO-31, and H-SAPO-34 investigated by multi-nuclear solid-state NMR spectroscopy. *Micropor. Mesopor. Mat.* **2002**, 56, (3), 267-278.
27. Blackwell, C. S.; Patton, R. L., Solid-State NMR of Silicoaluminophosphate Molecular-Sieves and Aluminophosphate Materials. *J. Phys. Chem.* **1988**, 92, (13), 3965-3970.
28. Buchholz, A.; Wang, W.; Arnold, A.; Xu, M.; Hunger, M., Successive steps of hydration and dehydration of silicoaluminophosphates H-SAPO-34 and H-SAPO-37 investigated by in situ CF MAS NMR spectroscopy. *Micropor. Mesopor. Mat.* **2003**, 57, (2), 157-168.
29. Xu, L.; Du, A. P.; Wei, Y. X.; Wang, Y. L.; Yu, Z. X.; He, Y. L.; Zhang, X. Z.; Liu, Z. M., Synthesis of SAPO-34 with only Si(4Al) Species: Effect of Si Contents on Si Incorporation Mechanism and Si Coordination Environment of SAPO-34. *Micropor. Mesopor. Mat.* **2008**, 115, (3), 332-337.

30. Yan, Z. M.; Chen, B. H.; Huang, Y., A solid-state NMR study of the formation of molecular sieve SAPO-34. *Solid State Nucl. Mag.* **2009**, 35, (2), 49-60.
31. Karge, H. G.; Beyer, H. K., *Solid-State Ion Exchange in Microporous and Mesoporous Materials*. Springer-Verlag: Berlin Heidelberg, 2002; Vol. 3.
32. Yang, R. T., *Adsorbents: Fundamentals and Applications*. Wiley: New York, 2003.
33. Khelifa, A.; Derriche, Z.; Bengueddach, A., Sorption of Carbon Dioxide by Zeolite X Exchanged with Zn^{2+} and Cu^{2+} . *Micropor. Mesopor. Mat.* **1999**, 32, (1-2), 199-209.

Chapter 3

Sr²⁺-SAPO-34 Prepared via Coupled Partial Detemplation and Solid State Ion Exchange: Effect on Textural Properties and Carbon Dioxide Adsorption

Sr²⁺-SAPO-34 materials were prepared via solid-state ion exchange (SSIE) to improve their CO₂ adsorptive properties, particularly at low partial pressures, and to study the effect of the ion exchange treatments on the structural and textural properties of the materials. In the past, these materials have been prepared with traditional liquid-state ion exchange (LSIE) methods yielding a strontium(II) content of about one cation per unit cell, well below the theoretical maximum and probably due to aqueous phase equilibrium constraints. Characterization of the SSIE materials included coupled thermal gravimetric analyses / Fourier transform infrared spectroscopy (TGA/FT-IR), X-ray diffraction (XRD), energy-dispersive analysis by X-rays (EDAX), surface area, and pure component CO₂ equilibrium adsorption. Coupled TGA/FT-IR studies were used for the selection of the SSIE temperature for both NH₄⁺-SAPO-34 and as-synthesized Na⁺-SAPO-34 starting materials. In general, the results indicated that temperatures well above the Tammann point are necessary to achieve acceptable strontium(II) loadings via SSIE while minimizing the loss of effective surface area due to pore clogging with unexchanged SrCl₂. Furthermore, *in situ* partial detemplation (PD) of the as-synthesized material during SSIE

avoided the formation of excess proton (acid) sites and allowed further loading of strontium(II) onto sites suitable for interaction with CO₂. In order to increase the strontium(II) loading per unit cell, a combined PD/SSIE/LSIE strategy was used to remove some of the remaining tenacious sodium(I) cations remaining after SSIE. This approach resulted in materials with a loading of nearly two strontium cations per unit cell and, as a result, improved the overall CO₂ adsorption performance of the materials in a remarkable fashion.

3.1. Introduction

The work presented in Chapter 2 was focused on a multistep liquid-state ion exchange (LSIE) strategy to increase the extraframework strontium(II) loading onto Sr²⁺-SAPO-34 zeolitic structure in an attempt to enhance the CO₂ sorption behavior.¹ In this respect, limitations of the ion exchange technique were established based on the detrimental effect of the procedure in the textural and adsorptive properties of SAPO-34, emphasizing that complete ion exchange was never achieved (i.e. only 24% of the cation sites in the structure were exchanged for strontium). Although this behavior has been observed in other zeolitic materials,²⁻⁶ there is still room for improvement if one deals with the equilibrium limitations imposed by LSIE and manages to inhibit the formation of cation sites forbidden to strontium(II) exchange.

The advantage of employing solid-state ion exchange (SSIE) is the potential elimination of some if not all of the equilibrium problems previously mentioned. Although this comes at the expense of a higher energy input (i.e., solid phase diffusion), this technique has proven to be effective for other zeolitic systems.⁷⁻⁹ The SSIE technique has been extensively reviewed by Karge et al., including the introduction of rare earth elements onto zeolitic frameworks.^{10, 11} Additional reports about SSIE include the introduction of In³⁺, Ga³⁺, Cu²⁺ and Ni²⁺ onto SAPO¹²⁻

¹⁶ via a reductive solid-state reaction, introduction of a number of extraframework species onto other zeolitic frameworks,^{17, 18} and the preparation of catalysts.¹⁹⁻²⁸ Although these reports are sound evidence of the prospects of SSIE, there are no detailed studies dealing with the introduction of strontium(II) cations or any rare earth element onto the small-pore SAPO-34 via SSIE.

One of the objectives of the present study is the evaluation of SSIE for the introduction of extraframework strontium(II) cations onto SAPO-34 using different loadings of a strontium chloride salt ($\text{SrCl}_2 \cdot 6\text{H}_2\text{O}$), ion exchange temperatures, and starting materials (i.e. NH_4^+ -SAPO-34 vs. Na^+ -SAPO-34). Analysis of the salt loading was necessary since, upon complete detemplation, these materials contain considerable amounts of H^+ and residual Na^+ cations per unit cell that occupy positions forbidden to strontium(II). For SSIE based on Na^+ -SAPO-34 as basis material, we also employed a partial detemplation (PD) method in an attempt to minimize the formation of H^+ . Hernandez-Maldonado recently reported about the possibility of cleaving quaternary ammonium ion templates to produce ammonium ions as evidenced by infrared spectroscopy methods.²⁹ Partial decomposition of the template, tetraethylammonium (TEA^+), leads to the formation of larger protonated species (i.e., NH_4^+) that given their size would be located in sites exposed for strontium(II) ion exchange. In addition, we have studied for the first time a combined PD-SSIE-LSIE approach to allow for the exchange of Na^+ ions that remain after SSIE. All of the following results and discussion are based on the analyses of the crystallinity, compositional characteristics, and textural and CO_2 adsorptive properties of the materials.

3.2. Experimental Section

3.2.1 Adsorbent Synthesis

The crystalline material Na^+ -SAPO-34, was prepared via hydrothermal synthesis using tetraethylammonium hydroxide (TEAOH) as a structure-directing agent (SDA) or template. A detailed description of the synthesis is available elsewhere.^{1, 30-33} The TEA^+ was partially or completely decomposed (i.e., detemplation) via calcination in a computer-controlled muffle furnace.³⁴ Preparation of the ammonium based SAPO-34 consisted of liquid phase ion exchanging fully detemplated Na^+ -SAPO-34 materials with ammonium chloride rich aqueous solutions in a multistep fashion. A 20:1 molar salt cation to zeolite cation content was employed, and the details of the procedure are available elsewhere.^{1, 35}

3.2.2 Preparation of Strontium(II) Ion-Exchanged Materials

SSIE of ammonium and proton (acid) sites in SAPO-34 with strontium(II) was accomplished via thermal treatment of mechanical mixtures.^{7, 10, 14, 15} NH_4^+ -SAPO-34 and as-synthesized Na^+ -SAPO-34 materials were each thoroughly mixed with different amounts of strontium chloride salt ($\text{SrCl}_2 \cdot 6\text{H}_2\text{O}$) in an agate mortar for 3 to 5 minutes, with careful attention given not to applying too much friction to avoid zeolitic dealumination.³⁶⁻³⁸ Although, other techniques were used for mixing the salt in the zeolitic matrix (see Appendix C), better results were obtained using the mortar. The amount of $\text{SrCl}_2 \cdot 6\text{H}_2\text{O}$ used was 10, 18, 25 or 31-wt% (dry zeolite basis) and the resulting mixture was placed in a flow reactor under helium atmosphere and heated to a specific temperature. The SSIE occurred after raising the temperature at $10^\circ\text{C}/\text{min}$ to 350°C , 430°C or 600°C and holding this temperature for 50 hours to ensure complete ion exchange of

the strontium(II) species. The samples prepared via SSIE at 600°C using as-synthesized Na⁺-SAPO-34 were first treated at 430°C for 15 hours to partially decompose the template (TEA⁺). After the SSIE procedure was completed, the samples were also treated at 600°C with air for 15 hours to remove any tenacious template residues. A justification for the selection of the SSIE temperatures will be presented in the Results and Discussion section.

To avoid the presence of intracrystalline water molecules adsorbed in the zeolite surface, which could be detrimental to the SSIE process, a two-stage thermal dehydration process (100°C and 200°C) was employed prior to each SSIE step. It should be mentioned that preliminary tests confirmed that the gas environment nature (i.e. nitrogen, helium or air) has no effect on the development of the ion exchange reaction.¹⁴ However, the gas employed for SSIE has to be moisture and oil free. The length of the reaction was also studied and it was found that 50 hours was sufficient time to achieve the ion exchange.

3.2.3 Coupled Thermal Gravimetric Analyses (TGA) / Fourier Transform Infrared Spectroscopy (FT-IR).

A TA-Q500 microbalance was employed for gravimetric measurements. Samples were heated inside the chamber of the TGA unit from ambient temperature to 800°C at a heating rate of 15°C/min using a constant helium (high purity grade, Praxair) flow of 60 mL/min. The gas was pretreated with presorbers (i.e., 3A zeolites and hydrocarbon traps) to remove traces of water or other contaminants that could have been present. The gas exhaust of the TGA instrument was monitored and analyzed with a Fourier transform infrared (FT-IR) spectrometer in an attempt to identify the species evolving from the as-synthesized Na⁺-SAPO-34 and the ion exchanged NH₄⁺-SAPO-34.

The FT-IR spectrometer setup consisted of a Nicolet 6700 Optical Spectrometer Mainframe connected to a Nicolet X700 TGA/IR interface module. The latter contains a high efficiency condensing and collection optics setup, a DLa TGS detector, a nickel-coated stainless steel gas cell and a heated transfer line. Both the transfer line and the gas cell are thermally insulated to prevent cold spots and, therefore, condensation of high boiling point materials onto the system. Although the TGA can be operated at temperatures close to 1000°C, the IR interface is only operable at temperatures up to 327°C. During the experiments, about 30 mg of sample were placed in the TGA instrument and heated from room temperature to 800°C at a rate of 15°C/min in a flow of dry, high-purity helium. The transfer line between the TGA exhaust and the IR bench, and the IR gas cell were heated to 210 and 220°C, respectively. During the tests, the spectral resolution (data spacing) was kept at 3.857 cm⁻¹ and signal averaging was performed for 50 scans/sample every 30seconds. Decomposition species were identified using IR reference data available elsewhere.

3.2.4 X-ray Diffraction and Compositional Analyses

X-ray diffraction (XRD) patterns of the materials were obtained using a Rigaku UTIMA III X-ray diffraction (CuK_α) equipped with a crossbeam optics system and used to corroborate the crystallinity of the materials. The unit cell elemental composition data were obtained employing the onboard energy dispersive X-ray (EDX) spectrometer of a JEOL JSM-6480LV instrument and using a voltage of 20.0 KV with a SUTW-sapphire detector. In addition, the strontium content was measured using an Agilent 7500ce inductively coupled plasma mass spectrometry (ICP-MS) instrument.

3.2.5 Porosimetry Analyses and CO₂ Adsorption Equilibrium Isotherms

Effective material surface area values were measured for all the SAPO-34 variants. The textural property was estimated after evaluation of nitrogen equilibrium adsorption data gathered at -196°C in a static volumetric adsorption system (Micromeritics ASAP 2020) outfitted with turbo molecular drag pumps. Carbon dioxide equilibrium isotherm data were also obtained employing the volumetric adsorption unit described above. Gases used were CO₂ (ultrahigh purity grade, Praxair) and He (high purity grade, Linde). Helium was used as a backfill gas after the adsorbent degassing stage and removed via an ultrahigh vacuum prior to the adsorption tests. All samples were pretreated in vacuum at 375°C to remove water molecules strongly bound inside the structure.³⁹ Carbon dioxide equilibrium tests were performed at 25, 50 and 75 °C, and pressures up to 1 atm. During the experiments, the temperature was kept constant by means of either a water bath or a heating blanket.

3.2.6 Isosteric Heat of Adsorption (ΔH_{ads})

The Clausius-Clapeyron equation (Eqn. 1) and pure component equilibrium adsorption data at different temperatures and constant surface loading were used to estimate the isosteric heats of adsorption.

$$\left(\frac{d \ln P}{d(1/T)} \right) \bigg|_{q=const} = \frac{\Delta H_{ads}}{R} \quad (3.1)$$

In this equation R is the gas constant, P is the equilibrium pressure at a particular coverage q and T is the absolute temperature.

3.3. Results and Discussion

It has been shown that extraframework cations play a key role in the adsorption properties of zeolitic materials since the magnitude of the surface electric field depends significantly on the valence and final location of these.^{40, 41} For CO₂ adsorption, the electric field gradient interacts with the adsorbate quadrupole moment, adding a significant and specific contribution to the total surface potential and, therefore, the heat of adsorption. Hernandez-Maldonado and co-workers have shown that, for SAPO-34 frameworks, strontium(II) cations result in outstanding CO₂ adsorption capacities at low partial pressures, probably due to cations occupying positions readily accessible to the adsorbate molecules and/or a synergistic effect with the SAPO framework.^{1, 29-31} After analysis of the strontium(II) loadings in SAPO-34 materials previously reported, it is evident that there is still room for improvement, particularly since divalent cations should prefer occupancy of positions around the chabazite cage perimeter due to charge repulsion criteria. Therefore, increasing the extraframework strontium(II) loading in SAPO-34 structures could only lead to an increase in CO₂ adsorption capacities at low partial pressure. Previous efforts have shown that liquid-state ion exchange (LSIE), even when employed in a multistage fashion, is not a suitable technique to increase the loading of alkaline earth metals onto SAPO-34 and other strategies should be considered.

Solid-state ion exchange (SSIE) is an alternative method to conventional LSIE, avoiding the use of water as a third component and the presence of solvated species during the procedure.^{8, 11, 42} Although hydrolysis of alkaline earth metal is not existent or negligible,⁴⁰ water molecules dictate the final position of cation sites in Na⁺-SAPO-34 materials and therefore weights significantly in the ion exchange equilibrium thermodynamics. Furthermore, since SSIE only

requires the use of stoichiometric amounts of the in-going cation source, waste or side products generation is minimized considerably.

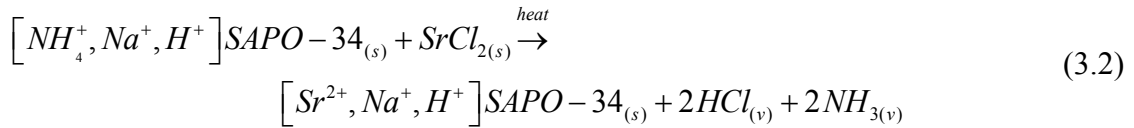
The availability of exposed sites in the material framework plays an important role in the success of ion exchange techniques, especially in SSIE where a relative excess of the in-going cation salt may cause detrimental adsorptive properties due to the presence of unreacted salt in the pore channels (i.e., occlusion). The influence of cation positions in adsorption processes is also exceptionally relevant for the discussion, and therefore the nomenclature related to the main sites occupied by cations within chabazite cages presented in Figure 3.2.1.1 Chapter 2 will be also useful: SI located at the center of the hexagonal prism; SII located at the center of the six-ring window; SII' at the cavity displaced from the six-ring window; SIII located near the center of the eight-ring window.¹⁶

For the SSIE procedure, selection of the starting material (i.e. NH_4^+ -SAPO-34 or H^+ -SAPO-34 vs. as-synthesized Na^+ -SAPO-34), the amount of salt containing the in-going cation and the temperature are important parameters for successful exchange. These are thoroughly discussed next.

3.3.1 Basis SAPO-34 materials for SSIE

The ammonium form of the zeolitic material (NH_4^+ -SAPO-34) was selected as one of the starting materials for SSIE because of the size and nature of NH_4^+ cations, which indicates that these are possibly located in sites available for ion-exchange of divalent species (SII, SII' or SIII). It is important to note that NH_4^+ -SAPO-34 was prepared via a multistep LSIE of fully detemplated Na^+ -SAPO-34 with NH_4Cl . However, some Na^+ cations still remained unexchanged

as evidenced by the elemental composition analysis made for the SAPO-34 materials (Table 3.1). The presence of Na^+ cations on the basis material will limit the percentage of strontium(II) ion exchange that could be achieved via SSIE since the former cations are known to preferentially occupy sites located at the center of hexagonal prisms (i.e., SI),⁴¹ which are usually restrictive for divalent cation occupancy due to charge repulsion criteria. It is also important to mention that the presence of Na^+ centers is not desired for SSIE because the temperature will not suffice for decomposition of the resulting NaCl molecules. Therefore, it is imperative to minimize the concentration of Na^+ per unit cell. The mechanism for the SSIE reaction between NH_4^+ -SAPO-34 and SrCl_2 (the incoming cation source) proceeds under removal of HCl and NH_3 , produced as volatile components according to Eqn.3.2:



As-synthesized Na^+ -SAPO-34 was used as an alternative basis material for SSIE due to results recently reported by Zhang et al. about avoiding the formation of some of the proton sites during the degradation of tetraethylammonium (TEA^+).²⁹ They found that partial detemplation (PD) at mild temperatures in helium (partial pyrolysis) could favor ion exchange since it allows the direct formation of NH_4^+ instead of H^+ . Although the resulting basis material would still contain sodium cations, some of these could be removed via a sequential LSIE stage as will be shown later in the discussion.

Table 3.1. Unit cell composition of fully detemplated Na⁺-SAPO-34 and Sr²⁺-SAPO-34 samples prepared via SSIE. Data for samples prepared via conventional LSIE and coupled SSIE-LSIE are also presented.

Sample	Preparation	Unit Cell Composition	Sr ²⁺ Unit Cell Content (wt.%)
Na ⁺ -SAPO-34	---	Na _{2.03} H _{3.09} [Si _{4.07} Al _{18.52} P _{13.41} O ₇₂]	0
NH ₄ ⁺ -SAPO-34 (LSIE) ^a	LSIE of Na ⁺ -SAPO-34	Na _{0.96} H _{3.84} [Si _{4.16} Al _{18.32} P _{13.52} O ₇₂]	0
Sr ²⁺ -SAPO-34 (SSIE-350-NH ₄ ⁺ -10) ^b	SSIE of NH ₄ ⁺ -SAPO-34 at 350 °C with ca. 10-wt%SrCl ₂ ·6H ₂ O	Na _{0.98} Sr _{0.87} H _{1.85} [Si _{4.11} Al _{18.23} P _{13.66} O ₇₂]	3.30
Sr ²⁺ -SAPO-34 (SSIE-600- NH ₄ ⁺ -10) ^b	SSIE of NH ₄ ⁺ -SAPO-34 at 600 °C with ca. 10-wt%SrCl ₂ ·6H ₂ O	Na _{1.16} Sr _{0.99} H _{1.54} [Si _{4.05} Al _{18.31} P _{13.63} O ₇₂]	3.73
Sr ²⁺ -SAPO-34 (SSIE-430-TEA ⁺ -10) ^b	SSIE of TEA ⁺ ,Na ⁺ -SAPO-34 at 430 °C with ca. 10-wt%SrCl ₂ ·6H ₂ O	Na _{1.73} Sr _{0.80} H _{1.52} [Si _{4.09} Al _{18.39} P _{13.53} O ₇₂]	3.01
Sr ²⁺ -SAPO-34 (SSIE-600-TEA ⁺ -10) ^b	SSIE of TEA ⁺ ,Na ⁺ -SAPO-34 at 600 °C with ca. 10-wt%SrCl ₂ ·6H ₂ O	Na _{1.56} Sr _{1.12} H _{1.29} [Si _{4.21} Al _{18.44} P _{13.35} O ₇₂]	4.18
Sr ²⁺ -SAPO-34 (SSIE-600-TEA ⁺ -10/LSIE)	SSIE of TEA ⁺ ,Na ⁺ -SAPO-34 at 600 °C with ca. 10-wt%SrCl ₂ ·6H ₂ O followed by LSIE	Na _{0.97} Sr _{1.61} H _{0.96} [Si _{4.21} Al _{18.47} P _{13.32} O ₇₂]	5.97
Sr ²⁺ -SAPO-34 (LSIE)	LSIE of Na ⁺ -SAPO-34	Na _{0.85} Sr _{1.16} H _{1.90} [Si _{4.16} Al _{18.46} P _{13.38} O ₇₂]	4.38

^aSome of the hydrogen content in the unit cell is associated with the presence of ammonium cations.

^bSome of the strontium content the unit cell corresponds to unexchanged SrCl₂ as evidenced by XRD data (Figures 4 and 5

In order to avoid plugging of the SAPO-34 small pore channels with the cation salt during the SSIE, it is critical to carefully estimate the amount of the in-going cation source. This would depend on the composition of the SAPO-34 framework, which would translate into an effective cation exchange capacity. According to the elemental compositional data of NH_4^+ -SAPO-34 (see Table 3.1), the theoretical amount of salt necessary to ion exchange all the ammonium and protons in the material structure is 0.232 g of $\text{SrCl}_2 \cdot 6\text{H}_2\text{O}$ per gram of dry zeolite or about 19-wt%. In the case of the as-synthesized Na^+ -SAPO-34 as basis materials, the theoretical amount of $\text{SrCl}_2 \cdot 6\text{H}_2\text{O}$ necessary to ion exchange all the protons corresponds to about 16-wt%.

3.3.2 Adsorbents characterization

Another critical parameter for SSIE is the temperature, considered to be the main driving force during the exchange process (see Eqn. 2). For the selection of a proper temperature, we considered the Tammann point of the salt as the first approach. The Tammann point is defined as the temperature where the salt begins to become appreciably mobile in the bulk of the solid, and it is approximately $\frac{1}{2}T_m$, where T_m is the melting point in absolute temperature units (i.e., K).⁴³ Since the melting point of the strontium source ($\text{SrCl}_2 \cdot 6\text{H}_2\text{O}$) is 868°C, the Tammann point is 297°C. Therefore, in order to obtain adequate mobility of strontium(II) cations to reach the ammonium and proton(acid) sites in the solid phase, the SSIE should be performed at a temperature of at least 300°C.

For evaluation of the SSIE temperature needed for NH_4^+ -SAPO-34 as the basis material, it is imperative to first evaluate the thermal decomposition profile of the ammonium-rich matrix and correlate it to the Tammann point. This was accomplished via coupled TGA/FTIR analysis and the results are shown in Figure 3.2.1. Three weight-loss regions were observed in the range of

25-800°C (see Figure 3.2.1A), with region I (25-200°C) corresponding to water desorption, region II (200-600 °C) corresponding to the decomposition of NH_4^+ , and region III (600-800 °C) corresponding to decomposition of residues possibly resulting from the detemplation of the as-synthesized material.

An FT-IR technique was used to analyze the exhaust gas from the TGA and identify the particular functional groups during the decomposition of NH_4^+ -SAPO-34 (see Figure 3.2.1B). The transient spectra stack (Figure 3.2.1B) shows no apparent contributions from functional groups until a temperature of approximately 300 °C is reached; this corresponds to a TGA weight loss of 13.50% and evidences what appears to be the formation of NH_3 (IR stretching modes of ammonia, 920 and 960 cm^{-1}). A considerable amount of CO_2 was formed at this temperature as indicated by the characteristic IR bands of the doublet at 2360 and 2305 cm^{-1} and a sharp spike at 674 cm^{-1} , corresponding to the asymmetric stretching and the degenerate bending vibration modes of CO_2 , respectively. The products from the decomposition disappeared at a temperature of around 510 °C. According to the TGA/FT-IR and Tammann point analyses, a temperature suitable for SSIE of NH_4^+ with Sr^{2+} cations should be in the range of 300 to 500 °C. A temperature beyond this range would result in the complete decomposition of NH_4^+ , rather producing a proton rich zeolitic material (i.e., H^+ -SAPO-34). Therefore, a temperature of 350 °C was chosen as first approximation for the SSIE experiments.

A coupled TGA/FT-IR study was also used to evaluate the decomposition profile of the TEA^+ molecule and select a suitable temperature for the PD mechanism of the as-synthesized Na^+ -SAPO-34. Although this has been reported before by our group,²⁹ it is important to always perform the tests since the SAPO-34 synthesis batches usually result in samples with small but

relevant differences in structural and textural properties. Figure 3.2 shows TGA and FT-IR spectra stacks that match very well with the findings of Zhang et al.²⁹ Employing an analysis similar to the one presented by Zhang et al., which was based on the presence of extralattice oxygen (ELO)⁴⁴⁻⁴⁶ and the identification of CO and C₂H₂ products from the template decomposition using the TGA/FT-IR data, the chosen temperature for partial detemplation and SSIE of as-synthesized Na⁺-SAPO-34 was 430 °C.

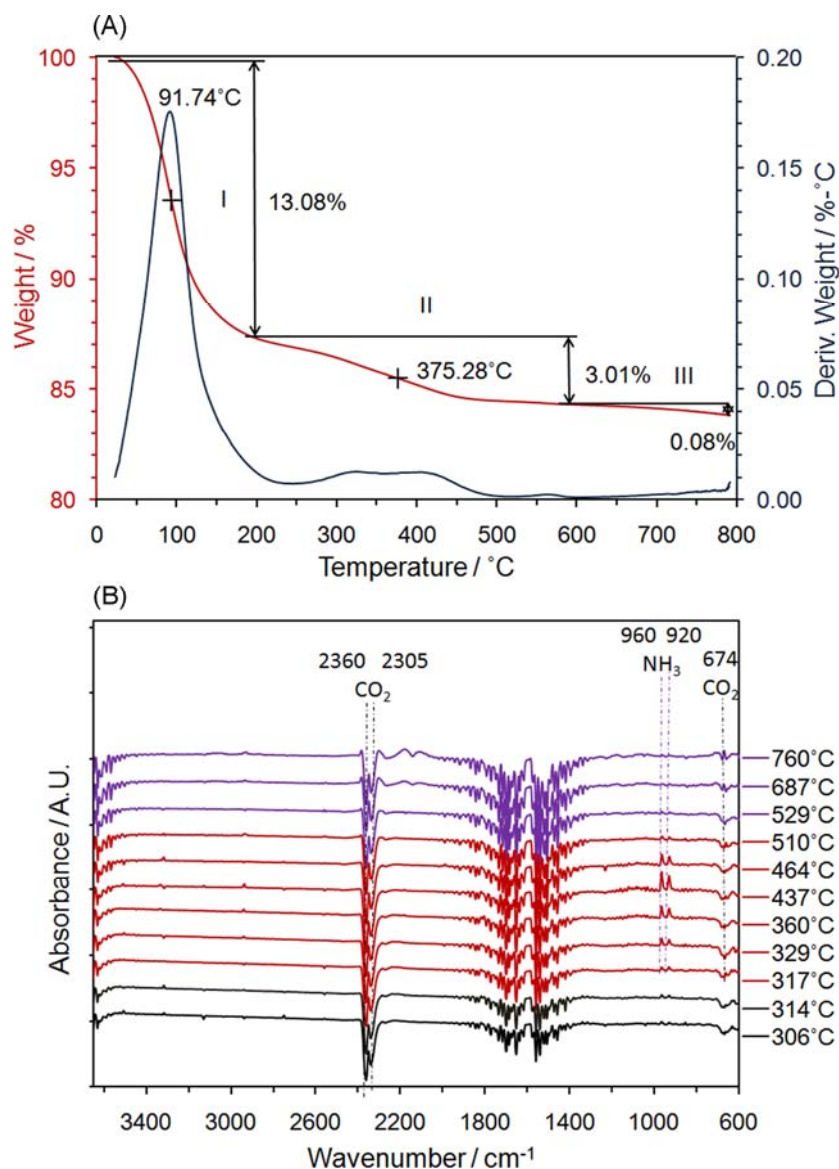


Figure 3.1. Coupled thermal gravimetric analyses (TGA)(A) and Fourier transform infrared spectroscopy (FT-IR) spectra(B) of the desorbed species arising from the decomposition NH₄⁺-SAPO-34 under helium at various temperatures.

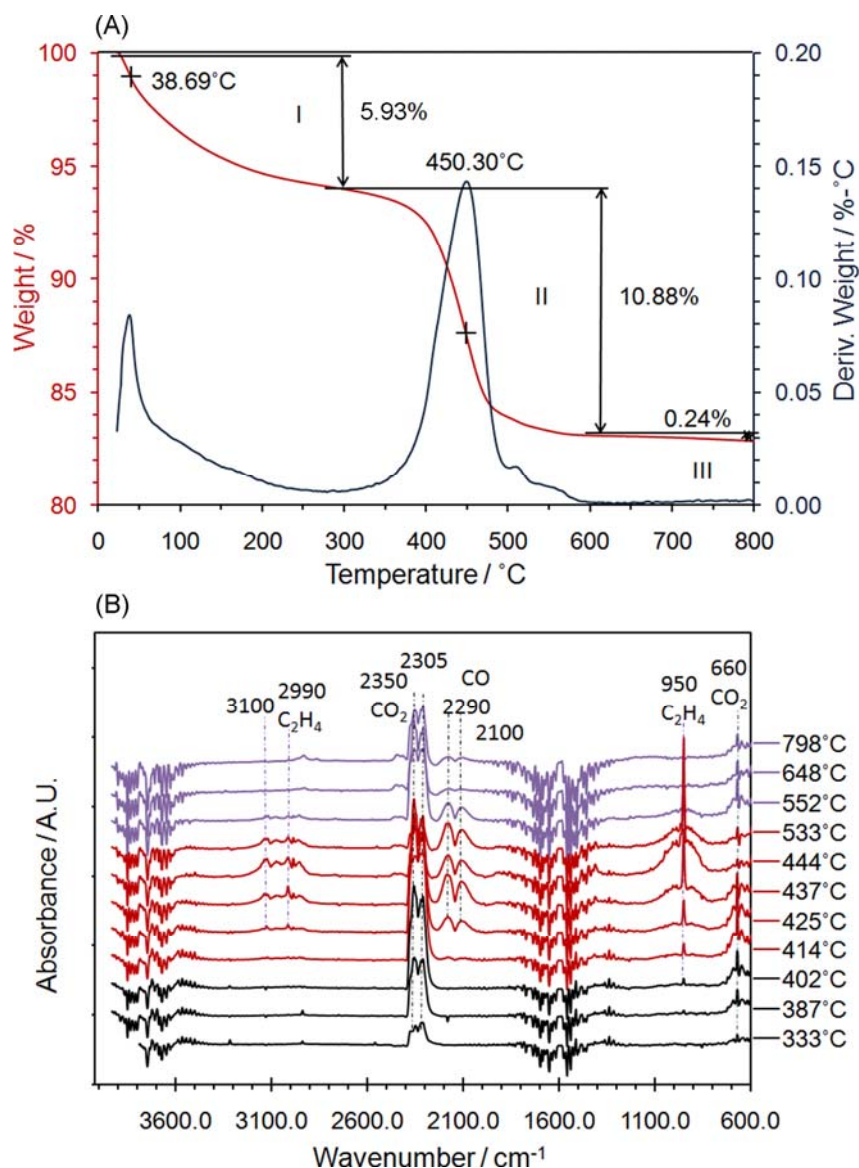


Figure 3.2. Coupled thermal gravimetric analyses (TGA) (A) and Fourier transform infrared spectroscopy (FT-IR) spectra(B) of the desorbed species arising from decomposition of TEA⁺ in Na⁺-SAPO-34 under helium at various temperatures.

It should be mentioned that a temperature of 600 °C was also used during SSIE experiments for both NH₄⁺ and Na⁺ basis materials to ensure complete diffusion of the strontium salt throughout the small SAPO-34 pores. However, the thermal treatment for the latter basis also included a soaking stage at 430 °C for 15 hours to allow for the degradation of TEA⁺ and the formation of NH₄⁺-SAPO-34 frameworks are stable up to ca. 900 °C⁴⁷ so the temperatures employed for SSIE should not be detrimental to the porous matrixes.

Figure 3.3 presents the XRD patterns and surface area values for detemplated Na^+ -SAPO-34 and Sr^{2+} -SAPO-34 samples obtained after the SSIE procedure using NH_4^+ -SAPO-34 as the starting material. XRD was employed as a technique to monitor the crystallinity of the SAPO-34 materials before and after modification. Likewise, the surface area values were employed to detect pore plugging resulting from the presence of unreacted salt. XRD peaks associated with the presence of unreacted dehydrated strontium chloride salt (SrCl_2) are $2\theta=22, 36.4$, and 43° and indicated in the patterns by asterisks.⁴⁸ Meanwhile, peaks associated with strontium chloride dihydrate ($\text{SrCl}_2 \cdot 2\text{H}_2\text{O}$) are shown by open circles at ca. $2\theta = 16, 19.7, 27.5, 32, 34$, and 35.5° .⁴⁹ In general, XRD data show that the crystal framework remains essentially unaltered after SSIE. However, all the patterns contain peaks associated within unreacted SrCl_2 . For the samples ion exchanged at 350°C (Figure 3.3A), the intensities of those peaks increased while the amount of $\text{SrCl}_2 \cdot 6\text{H}_2\text{O}$ is increased from 10 to 25-wt%. Furthermore, the surface area decreased by almost $100 \text{ m}^2 \cdot \text{g}^{-1}$ when a 25 wt.% initial salt loading was employed; this is clear evidence of pore plugging due to the presence of unreacted SrCl_2 salt. On the other hand, the sample ion exchanged based on 31 wt.% $\text{SrCl}_2 \cdot 6\text{H}_2\text{O}$ exhibits a diffraction pattern with lower intensity peaks at $2\theta = 22, 36.4$, and 43° and also contain peaks corresponding to $\text{SrCl}_2 \cdot 2\text{H}_2\text{O}$, when compared to those of the other SAPO-34 variants. Since the intensity of the peak at $2\theta = 9^\circ$ was considerably affected and the specific surface area registered was the lowest among the samples treated at 350°C , one could assume that a considerable amount of unreacted salt ended up dispersed across the pore channel surface. However, given the small dimensions of the SAPO-34 pore channel, it would be quite difficult to achieve such a phenomenon.

Although the XRD peaks associated with the pore channel conformation (low diffraction angles) are still present in the case of the samples ion exchanged at 600°C (Figure 3.3B), there

are also peaks associated with unreacted salt, indicating that an increase in temperature probably resulted in a faster decomposition of the NH_4^+ species. This would lead to the formation of H^+ and distribution of these species across sites not accessible to the in-going cation. As in the case of the samples SSIE at 350 °C, the sample surface area was greatly affected by the addition of more SrCl_2 , evidencing this clogging of the pore due to unreacted salt.

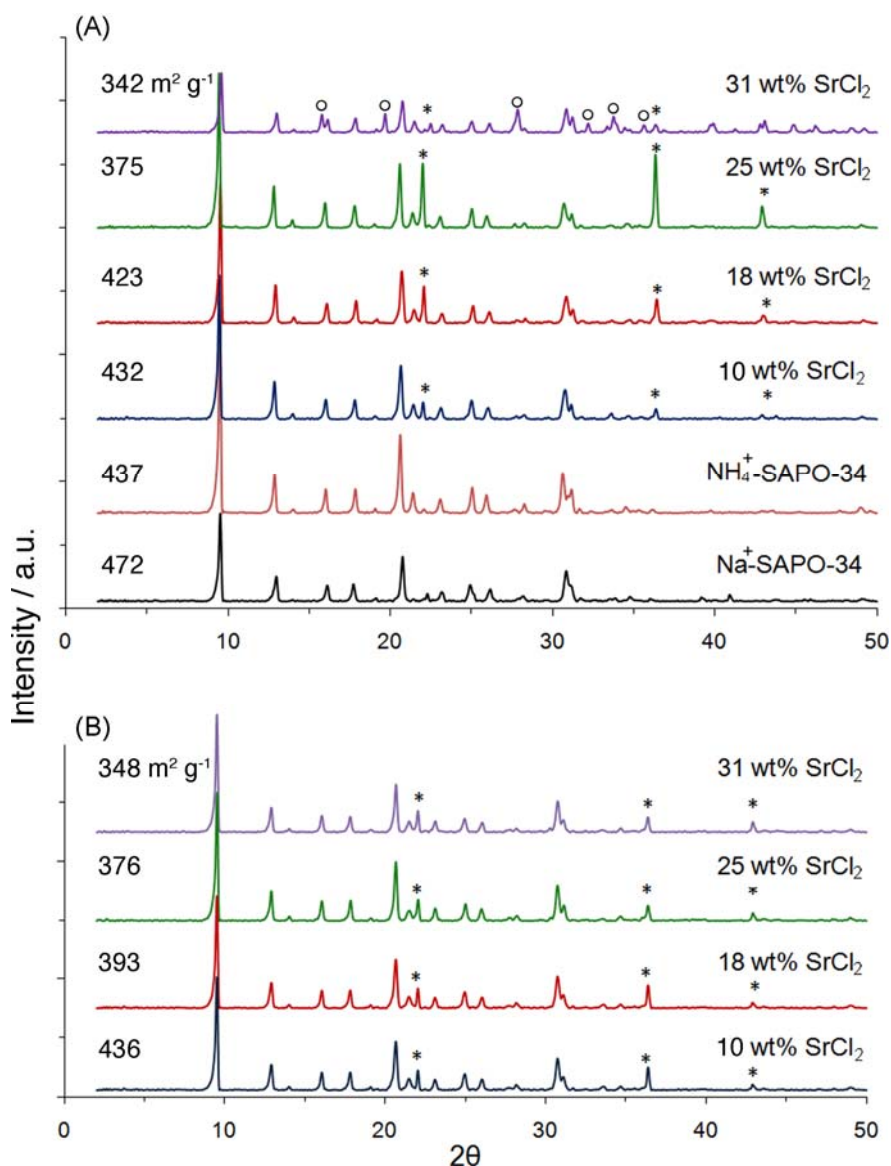


Figure 3.3, X-ray diffraction patterns and specific surface areas for Na^+ -SAPO-34 and ion-exchanged Sr^{2+} -SAPO-34 samples via SSIE at 350(A) and 600 °C (B), respectively, as a function of the $\text{SrCl}_2 \cdot 6\text{H}_2\text{O}$ loading (wt.%), using NH_4^+ -SAPO-34 as basis material. The asterisks and open circles represent diffraction peaks for SrCl_2 and $\text{SrCl}_2 \cdot 2\text{H}_2\text{O}$, respectively.

XRD data stacks for Sr^{2+} -SAPO-34 samples prepared via SSIE at 430 °C using as-synthesized Na^{+} -SAPO-34 as the starting material are gathered in Figure 3.4A. As in the previous cases, some of the XRD patterns and surface areas indicate the presence of unreacted salt after SSIE. The intensity of the peaks associated with the chloride salt became significant after the addition of 25-wt% $\text{SrCl}_2 \cdot 6\text{H}_2\text{O}$. When the SSIE temperature was increased to 600 °C (see Figure 3.4B), the effect of unreacted salt is only observed after the initial amount of $\text{SrCl}_2 \cdot 6\text{H}_2\text{O}$ in the solid matrix was equal to or greater than 18-wt%.

So far the results have indicated that, independently of the type of cation being exchanged or even the exchange temperature, the SSIE method is only capable of exchanging a specific but unknown amount of species below the theoretical cation exchange capacity of the SAPO-34 materials. This could be due to the difficulty of approaching perfect dispersion of the in-going cation salt across the solid matrix prior to SSIE and/or considerable salt diffusion resistance during the thermal process. A similar behavior has been reported for other zeolitic materials, including type-Y (synthetic Faujasite) and ZSM-5 zeolites.^{50, 51} In order to overcome the pore plugging and partial exchange problems, we employed a combined SSIE-LSIE method.

Crystallinity results for a sample prepared via SSIE at 600°C with 10wt.% of $\text{SrCl}_2 \cdot 6\text{H}_2\text{O}$ using as-synthesized Na^{+} -SAPO-34 followed by treatment via LSIE also with $\text{SrCl}_2 \cdot 6\text{H}_2\text{O}$ are shown in Figure 3.4B. This sample has the designation “SSIE-LSIE” on the patterns stack. Remarkably, the sample XRD pattern does not exhibit peaks associated with unreacted salt indicating that the LSIE stage probably removed any excess. This is also evident in the surface area estimated for the sample, which nearly matched the value obtained for a fully detemplated

Na⁺-SAPO-34 sample (see Figure 3.3B). The XRD pattern stack shown in Figure 3.4B also includes data for a SAPO-34 sample exchanged only via LSIE to serve as reference.

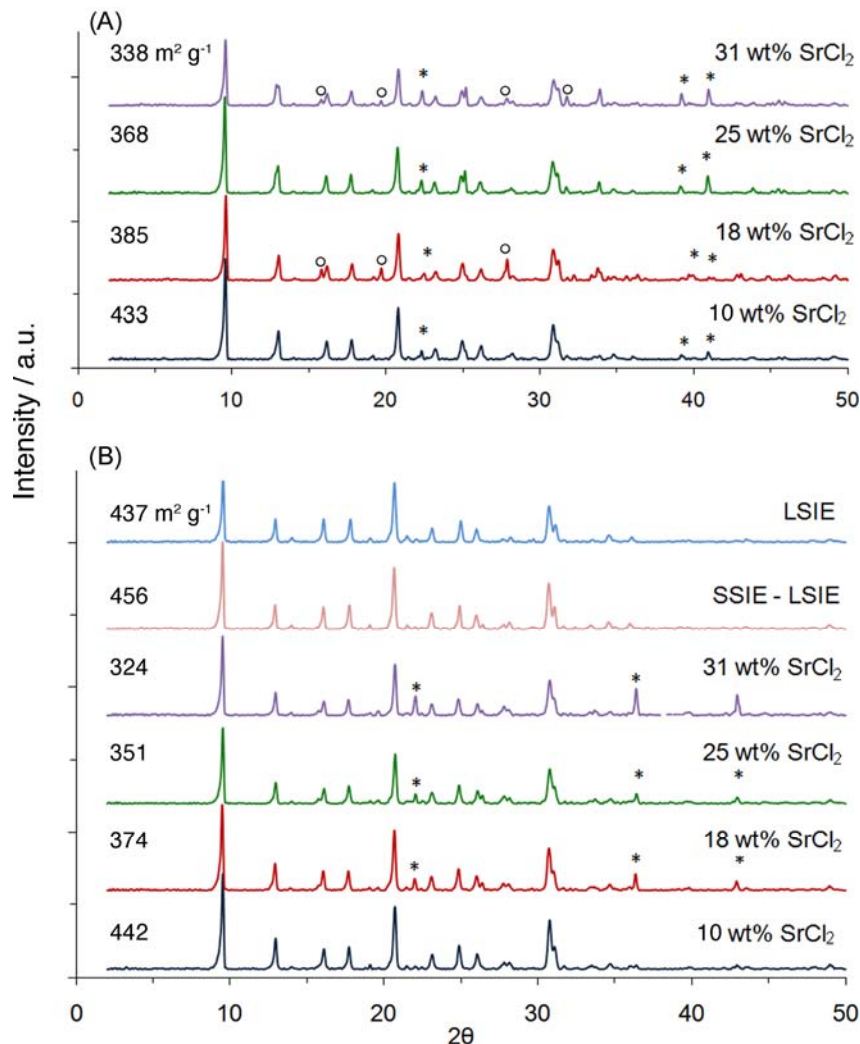


Figure 3.4. X-ray diffraction patterns and specific surface areas for ion-exchanged Sr²⁺-SAPO-34 samples via SSIE at 430 (A) and 600°C (B), respectively, as a function of the SrCl₂·6H₂O loading (wt.%), using as-synthesized Na⁺-SAPO-34 as basis material. Ion exchanged Sr²⁺-SAPO-34 via liquid-state ion exchange (LSIE) and combination of solid state ion exchange followed by liquid-state ion exchange procedure (SSIE-LSIE) are also presented. The asterisks and open circles represent diffraction peaks for SrCl₂ and SrCl₂·2H₂O, respectively.

Although the previous surface area data clearly show the effect of the SSIE on the textural properties of the materials, the extent of ion exchange could only be measured via direct monitoring of the unit cell composition. For Si, Al, P, and Na, this was accomplished using

careful EDX probing. To account for any potential variability, measurements were performed on six different spots, and the results are gathered in Table 3.1. The strontium content was estimated using ICP-MS while the proton (acid) site loading was estimated after making charge balance calculations. According to the compositional analyses, the samples prepared via SSIE at higher temperatures presented significant strontium content, apparently being slightly higher for the sample prepared at 600°C and using as-synthesized Na^+ -SAPO-34 as the basis material. This could be due to better dispersion or exchange of strontium across the bulk of the sample at higher SSIE temperature as evidenced by the XRD data shown in Figure 3.4B. In fact, when a lower temperature was used or an exchange was made for NH_4^+ -SAPO-34 as the starting material, the resulting material contained unexchanged strontium in the form of SrCl_2 (see Figures 4A-B and 5A), which could be present on a few places across the bulk. On the other hand, the highest strontium(II) loading was observed for the sample prepared via SSIE-LSIE where evidently there is no residue of SrCl_2 and, therefore, no strontium dispersion problems. The strontium loading in this case corresponds to nearly two cations per unit cell, which is the highest loading ever reported for this material and should be exceptional for gas ultrapurification applications.

The elemental analyses also show the relevance of the nature of the cations present in the zeolitic cavities in order to achieve good SSIE results. Hydrogen cations, in particular, appear to be the main species to be ion exchanged from the basis materials (i.e., NH_4^+ -SAPO-34 or Na^+ -SAPO-34). The main source of proton (acid) sites is the detemplation process and/or ammonium cations, but if the source cationic species (TEA^+ fractions) remain present during the initial stage of the exchange process it is possible to replace them since these will likely occupy sites that are readily accessible to strontium(II) (i.e., SII or SIII). Therefore, the reduction in proton (acid) sites content shown in Table 3.1 is most likely a result of the exchange of sources of proton (acid)

sites sources rather than the direct exchange of these. Table 3.1 also shows variability on the Na^+ content among the samples treated by SSIE and this was probably due to formation of NaCl. Although formation of NaCl could result in pore plugging, its Tammann point (ca. 264 °C) is lower than that of SrCl_2 , and this should provide a mean for the displacement of the former toward the outermost surface of the crystals as evidenced by the surface area values shown in Figures 4 and 5. In the case of combined SSIE-LSIE, evidently the LSIE took care of removing any NaCl besides exchanging tenacious Na^+ and H^+ cations. Upon hydrolysis, the distribution of these species throughout the framework changes considerably, probably resulting in cation sites better exposed for ion exchange with strontium(II).

In general, for samples prepared via SSIE and coupled PD-SSIE, both compositional and structural results indicate that it was possible to systematically load strontium(II) onto SAPO-34 without detrimental effects to the framework. However, LSIE was still necessary to exchange tenacious cations, suggesting that this stage should always follow SSIE for cases involving zeolitic materials such as SAPO-34.

3.3.1 CO₂ Adsorption Performance

Figure 3.5A shows pure component CO₂ adsorption isotherms obtained at 25 °C for a fully detemplated Na^+ -SAPO-34 and the Sr^{2+} -SAPO-34 materials prepared with SSIE at 350 and 600 °C, respectively, and with NH_4^+ -SAPO-34 as the starting material. The adsorption isotherms evidence how detrimental was the SSIE process to the material adsorption performance upon an increase in the SrCl_2 used. The uptake amounts obtained at moderate partial pressure corroborated that the pores were indeed plugged or at least partially plugged by unexchanged SrCl_2 . SSIE at 600°C, however, resulted in samples with better CO₂ capacity as indicated by the

isotherms gathered in Figure 3.5B. Although the average adsorption capacity of the ion-exchanged materials is lower than that of a fully detemplated Na^+ -SAPO-34, the interaction between extraframework strontium(II) cations and CO_2 molecules at low partial pressure still dominate, particularly for the materials SSIE exchanged at 600 °C. Still, the observed capacities are below the ones previously reported.^{1, 31}

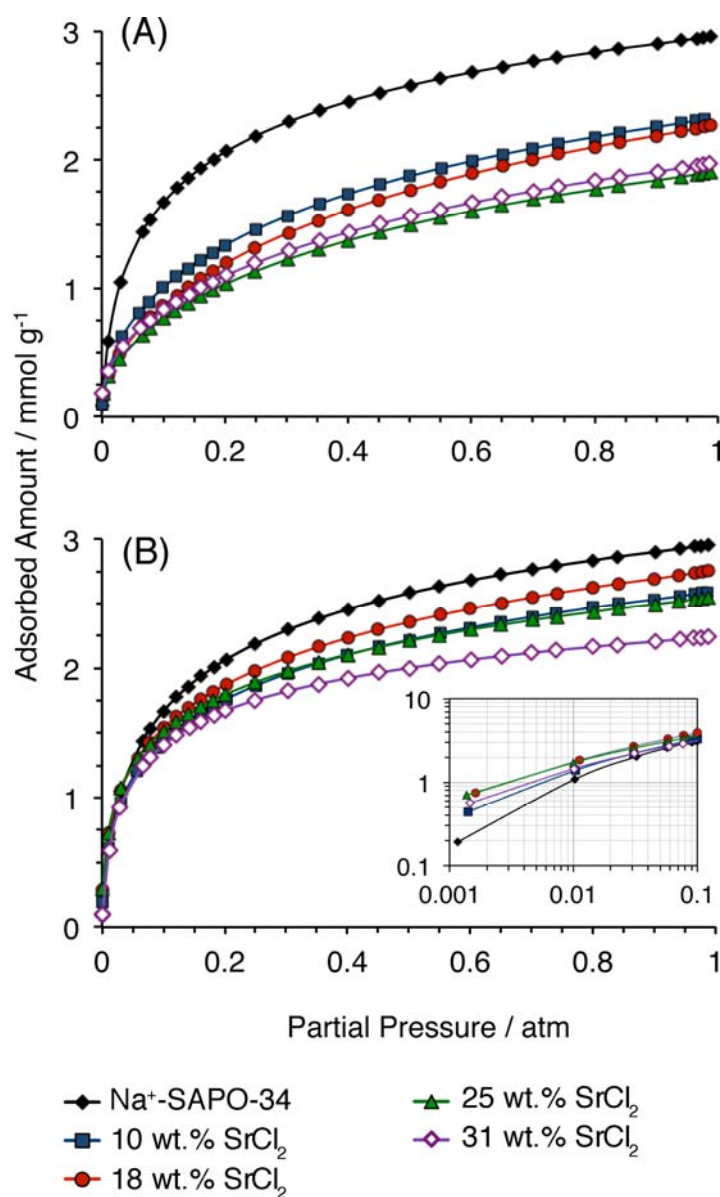


Figure 3.5. CO_2 adsorption isotherms obtained at 25 °C for Sr^{2+} -SAPO-34 prepared samples via SSIE at 350 (A) and 600 °C (B), respectively, and NH_4^+ -SAPO-34 as basis material. The figure also included isotherm data gathered for a fully detemplated Na^+ -SAPO-34 material.

Figure 3.6 shows pure component CO₂ adsorption isotherms at 25 °C obtained for Sr²⁺-SAPO-34 prepared via SSIE at 430 and 600 °C, respectively, and using as-synthesized Na⁺-SAPO-34 as basis material. The isotherms for these strontium(II)-based adsorbent variants also showed a decrease in the CO₂ adsorption capacity upon an increase in SrCl₂ during the SSIE, but not as pronounced as in the case of the materials prepared using NH₄⁺-SAPO-34 as basis.

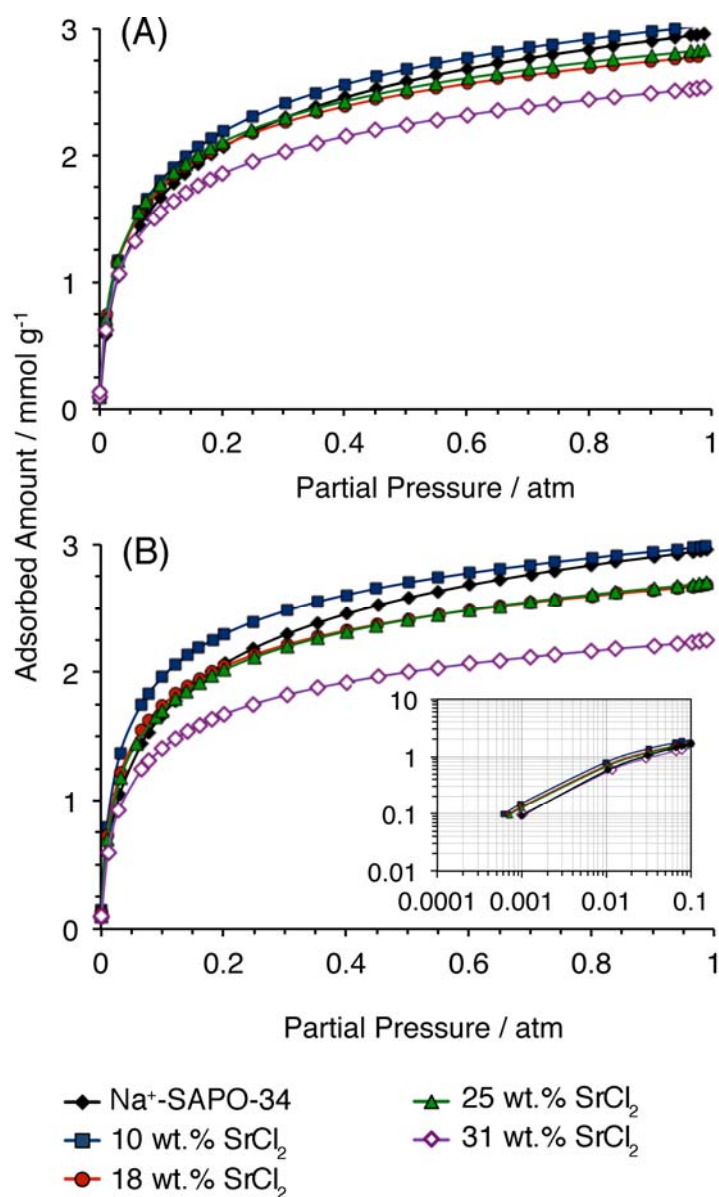


Figure 3.6. CO₂ adsorption isotherms obtained at 25 °C for Sr²⁺-SAPO-34 prepared samples via SSIE at 430 (A) and 600 °C (B), respectively, and as-synthesized Na⁺-SAPO-34 as basis material. The figure also included isotherm data gathered for a fully detemplated Na⁺-SAPO-34 material.

A significant increase in the CO₂ sorption capacity was observed for the sample prepared via SSIE at 600 °C and initial SrCl₂ loading of 10-wt% (Figure 3.6B), particularly in the 0.02 to 0.4 atm partial pressure region. The same was not observed at much lower partial pressures, probably due to occupancy of strontium(II) cations of new positions therefore affecting the overall interaction with the CO₂ molecules. This contrasts considerably with the results obtained previously with LSIE samples, where the isotherms displayed improved CO₂ loadings at low partial pressure compared to those of Na⁺-SAPO-34.^{1,29,31} Since the starting Na⁺-SAPO-34 material employed here contains a significant amount of Na⁺ cations that were not ion exchanged via SSIE at 600 °C (see Table 3.1), the presence of these extraframework species probably produced redistribution of the strontium(II) centers. This was verified by measuring the CO₂ loadings onto the material prepared via coupled SSIE-LSIE strategy, this is discussed below.

Figure 3.7 shows pure component CO₂ adsorption isotherms gathered at 25 °C for Sr²⁺-SAPO-34 materials prepared via SSIE-LSIE and conventional LSIE. When the data are compared to the ones gathered for Na⁺-SAPO-34, it is evident that the SSIE-LSIE method results in superior CO₂ loadings at low partial pressures. Furthermore, there is a ca. 25% increase in CO₂ loading compared to that of the samples prepared by LSIE. This evidences how the exchange of additional Na⁺ cations (see Table 3.1) results in more interaction of CO₂ with strontium(II). It should be mentioned that, although the adsorbent prepared via conventional LSIE also exhibits considerable CO₂ loadings, the SSIE-LSIE approach results in materials with less faulting and better textural properties as shown by the CO₂ loadings at 1 atm. Zhang et al. found that a PD approach results in less SAPO-34 framework faulting as opposed to a full detemplation approach. Similar results were observed for ion exchanged Ba²⁺-SAPO-34 materials prepared via solid state ion exchange (see Appendix D).

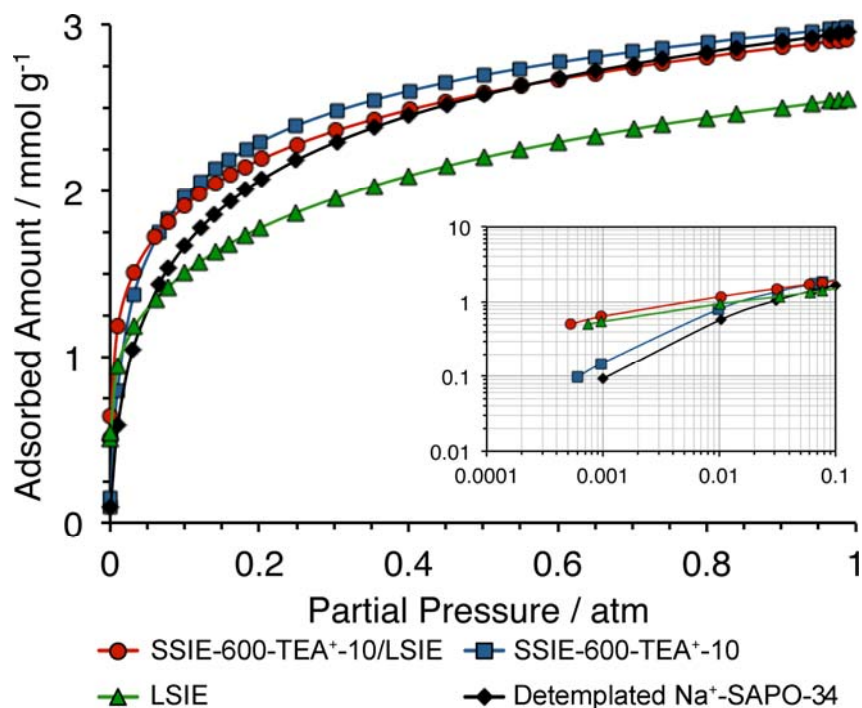


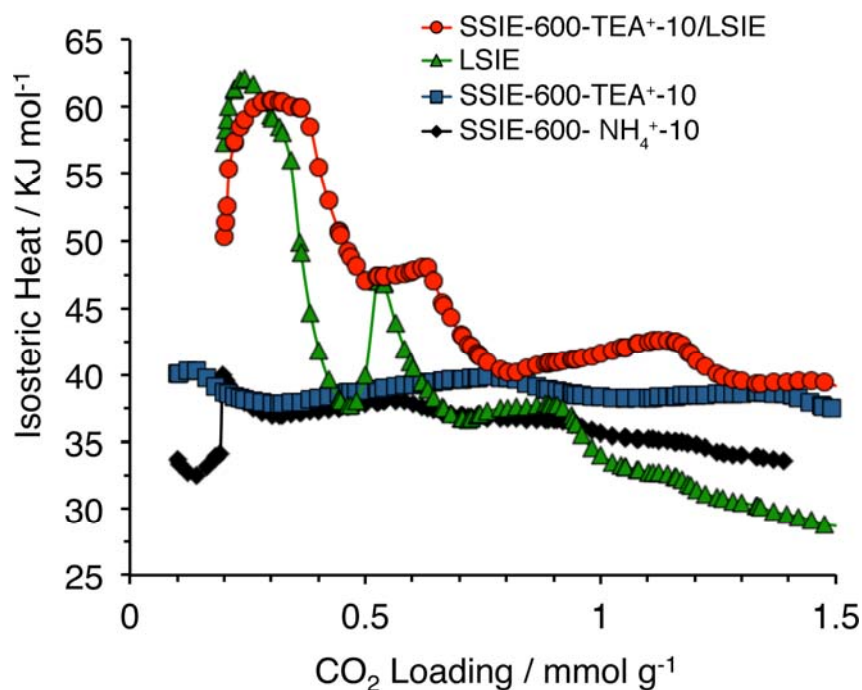
Figure 3.7. CO₂ adsorption isotherms obtained at 25 °C for several Sr²⁺-SAPO-34 samples. The figure also includes isotherm data gathered for a fully detemplated Na⁺-SAPO-34 material. Refer to Table 3.1 for sample identification.

Although it is evident that the SSIE-LSIE method results in the best overall CO₂ adsorbent possible, the other Sr²⁺-SAPO-34 variants displayed loadings at low partial pressures that deserve further discussion, particularly with emphasis on the surface interactions or isosteric heat of adsorption. Figure 3.8 shows the CO₂ isosteric heat of adsorption for Sr²⁺-SAPO-34 prepared via SSIE, LSIE and coupled SSIE-LSIE.

The profiles for the samples prepared via SSIE reflect that the adsorbent surface is mostly homogeneous, with an average heat of adsorption of approximately 36 KJ/mol. This contrasts with the results obtained for the sample prepared via LSIE, which indicated a rather heterogeneous surface and matched well with the results reported elsewhere for Sr²⁺-SAPO-34 and other zeolitic materials prepared in a similar fashion.^{1, 29, 30, 52} This evidences that the cation distribution of the samples prepared via SSIE is quite different from those of the materials prepared via LSIE, even with similar strontium(II) loadings (see Table 3.1) and further explains

the results shown in Figures 6 and 7. The sample prepared by a combination of SSIE and LSIE also showcased an isosteric heat profile typical of a heterogeneous surface, with an average heat of ca. 45 KJ/mol. Using the data shown in Table 3.1, the maximum heat of adsorption of the LSIE and SSIE-LSIE variants occurs when the CO₂ loading corresponds to ca. 1.04 and 0.9 CO₂ per strontium(II) cation, respectively, which underlines the importance of increasing the amount of exposed, extraframework strontium(II) cations in the SAPO-34 framework.

Figure 3.8. Isosteric heat of adsorption for CO₂ in Sr²⁺-SAPO-34 samples. Refer to Table 3.1 for sample identification.



3.4. Conclusions

Experiments have shown that extraframework strontium(II) cations can be introduced onto SAPO-34 frameworks via solid-state ion (SSIE) exchange. XRD, surface area, and elemental analyses indicated that it was possible to load strontium(II) at a temperature of 600 °C without major structural and textural damage, which is of utmost importance if the materials are to be

considered for adsorption applications. Coupled TGA/FT-IR studies were useful for the selection of the temperature of the SSIE in cases involving *in situ* decomposition of NH_4^+ or TEA^+ . Meanwhile, the maximum loading of strontium during SSIE greatly depends on the selection of the basis material (i.e., NH_4^+ -SAPO-34 or as-synthesized Na^+ -SAPO-34).

In terms of CO_2 adsorption performance, the Sr^{2+} -SAPO-34 adsorbent materials prepared via coupled partial detemplation / SSIE exhibited the best uptake capacity among the SSIE variants at moderate gas partial pressure. A superior CO_2 adsorption capacity at all partial pressures was obtained after preparation of Sr^{2+} -SAPO-34 via SSIE followed by a liquid-state ion exchange (LSIE) treatment, indicating that tenacious residual Na^+ ions could only be removed via an SSIE/LSIE combination. In general, these findings indicate that it is possible to increase the strontium(II) content per unit cell via SSIE due to the absence of liquid medium equilibrium limitations such as those found in typical LSIE. Although the practical aspects of SSIE could be limited by the energy input required for fast SSIE, the results are clear evidence that the technique could be considered in cases where the application demands particular adsorption characteristics and exceptional capacity such as ultrapurification of gases. Furthermore, the technique may be suitable for zeolitic materials that are unstable to humidity after detemplation, allowing their effective functionalization in a moisture-free process.

3.5. Literature Cited

1. Arevalo-Hidalgo, A. G.; Santana, J. A.; Fu, R.; Ishikawa, Y.; Hernandez-Maldonado, A. J., Separation of CO_2 from Light Gas Mixtures Using Nanoporous Silicoaluminophosphate Sorbents: Effect of Multiple-Step Ion Exchange and Adsorption Mechanism Via Computational Studies. *Microporous Mesoporous Mater.* **2009**, 130, (1-3), 142-153.
2. Hammoudi, H.; Bendenia, S.; Marouf-Khelifa, K.; Marouf, R.; Schott, J.; Khelifa, A., Effect of the Binary and Ternary Exchanges on Crystallinity and Textural Properties of X Zeolites. *Microporous Mesoporous Mater.* **2008**, 113, (1-3), 343-351.

3. Sato, K.; Nishimura, Y.; Matsubayashi, N.; Imamura, M.; Shimada, H., Structural Changes of Y Zeolites During Ion Exchange Treatment: Effects of Si/Al Ratio of the Starting NaY. *Microporous Mesoporous Mater.* **2003**, 59, (2-3), 133-146.
4. Amari, D.; Ginoux, J. L.; Bonnetain, L., Textural Damage of Cation-Exchanged LTA Zeolites Studied by Gas-Adsorption. *Zeolites* **1994**, 14, (1), 58-64.
5. Fichtnerschmittler, H.; Lutz, W.; Amin, S.; Dyer, A.; Wark, M., Hydrothermal Damage of Ion-Exchanged A-Type Zeolite Cation-Directed Mechanism of Phase-Transformation. *Zeolites* **1992**, 12, (6), 750-755.
6. Salla, I.; Salagre, P.; Cesteros, Y.; Medina, F.; Sueiras, J. E., Study of the Influence of Several Mordenite Modifications on its N₂ and O₂ Adsorption Properties. *J. Phys. Chem. B* **2004**, 108, (17), 5359-5364.
7. Weitkamp, J.; Ernst, S.; Bock, T.; Kromminga, T.; Kiss, A.; Kleinschmit, P. Modified molecular sieves by means of solid ion exchange. US Patent 5,529,964, 1996.
8. Haniffa, R.; Seff, K., Partial Structures of Fully Dehydrated Ni₃₀Na₇Cl₁₂Si₁₃₇Al₅₅O₃₈₄ (Solid-State Nickel(II)-Exchanged Zeolite Y) and of Its D₂O Sorption Complex by Pulsed-Neutron Diffraction. *J. Phys. Chem. B* **1998**, 102, (15), 2688-2695.
9. Zanjanchi, M. A.; Ebrahimian, A., Studies on the Solid-State Ion Exchange of Nickel Ions into Zeolites Using DRS Technique. *J. Mol. Struct.* **2004**, 693, (1-3), 211-216.
10. Karge, H.; Beyer, H., Solid-State Ion Exchange in Microporous and Mesoporous Materials. In *Molecular Sieves Science and Technology*, Karge, H.; Weitkamp, J., Eds. Springer: Berlin, 2002; Vol. 3, pp 43-202.
11. Karge, H. G., Post-Synthesis Modification of Microporous Materials by Solid-State Reactions. In *Progress in Zeolite and Microporous Materials, Parts A-C*, Chon, H.; Ihm, S. K.; Uh, Y. S., Eds. 1997; Vol. 105, pp 1901-1948.
12. Zamadics, M.; Chen, X. H.; Kevan, L., Solid State Ion-Exchange in H-SAPO-34: Electron-Spin-Resonance and Electron-Spin Echo Modulation Studies of Cu (II) Location and Adsorbate Interaction. *J. Phys. Chem.* **1992**, 96, (13), 5488-5491.
13. Lee, C. W.; Chen, X. H.; Zamadics, M.; Kevan, T., Anionic Coordination Involvement in Solid-State Ion Exchanged CuH-SAPO-N (N=5, 11 and 34) Molecular Sieves. *J. Chem. Soc. Faraday T.* **1993**, 89, (22), 4137-4140.
14. Neinska, Y.; Minchev, C.; Kosova, L.; Kanazirev, V., Solid State Modification of As-Synthesized SAPO Molecular Sieves with Indium. In *Studies in Surface Science and Catalysis*, Beyer, H. K.; Karge, H. G.; Kiricsi, I.; Nagy, J. B., Eds. Elsevier: 1995; Vol. 94, pp 262-269.
15. Neinska, Y.; Minchev, C.; Dimitrova, R.; Micheva, N.; Minkov, V.; Kanazirev, V., Preparation of In- and Ga-Modified SAPO Materials via a Solid State Reaction. In *Studies in Surface Science and Catalysis*, Weitkamp, J.; Karge, H. G.; Pfeifer, H.; Hölderich, W., Eds. Elsevier: 1994; Vol. 84, pp 989-996.
16. Djieugoue, M. A.; Prakash, A. M.; Kevan, L., Electron Spin Resonance and Electron Spin-Echo Modulation Studies of Synthesized NiAPSO-34 Molecular Sieve and Comparison with Ion-Exchanged NiH-SAPO-34 Molecular Sieve. *J. Phys. Chem. B* **1999**, 103, (5), 804-811.

17. Mihalyi, M. R.; Beyer, H. K., Direct Evidence for the Incorporation of Univalent Indium into High-Silica Zeolite, H-ZSM-5, by Thermal Auto-Reductive Solid-State Ion Exchange. *Chem. Commun.* **2001**, (21), 2242-2243.
18. Dimitrova, R.; Neinska, Y.; Mihalyi, M.; Pal-Borbely, G.; Spassova, M., Reductive Solid-State Ion Exchange as a Way to Vanadium Introduction in BZSM and BBeta zeolites. *Appl. Catal. A-Gen.* **2004**, 266, (1), 123-127.
19. Mhamdi, M.; Khaddar-Zine, S.; Ghorbel, A., Influence of the Co/Al Ratio and the Temperature of Thermal Treatment on Cobalt Speciation and Catalytic Properties of Co-ZSM-5 Prepared by Solid-State Ion Exchange. *Appl. Catal. A-Gen.* **2008**, 337, (1), 39-47.
20. Abu-Zied, B. M.; Schwieger, W.; Unger, A., Nitrous Oxide Decomposition Over Transition Metal Exchanged ZSM-5 Zeolites Prepared by the Solid-State Ion-Exchange Method. *Appl. Catal. B-Environ.* **2008**, 84, (1-2), 277-288.
21. Xia, H.; Sun, K.; Fan, F.; Sun, K.; Su, W.; Feng, Z.; Ying, P.; Li, C., Effect of Extra-Framework Gallium on the Structure of Iron Species in Fe/ZSM-5. *J. Catal.* **2008**, 259, (2), 269-275.
22. Mhamdi, M.; Ghorbel, A.; Delahay, G., Influence of the V plus Mo/Al Ratio on Vanadium and Molybdenum Speciation and Catalytic Properties of V-Mo-ZSM-5 Prepared by Solid-State Reaction. *Catal. Today* **2009**, 142, (3-4), 239-244.
23. Mhamdi, M.; Khaddar-Zine, S.; Ghorbel, A., Influence of the Cobalt Salt Precursors on the Cobalt Speciation and Catalytic Properties of H-ZSM-5 Modified with Cobalt by Solid-State Ion Exchange Reaction. *Appl. Catal. A-Gen.* **2009**, 357, (1), 42-50.
24. Mihalyi, R. M.; Schay, Z.; Szegedi, A., Preparation of In,H-ZSM-5 for DeNO_x Reactions by Solid-State Ion Exchange. *Catal. Today* **2009**, 143, (3-4), 253-260.
25. Zamaro, J. M.; Miro, E. E.; Boix, A. V.; Martinez-Hernandez, A.; Fuentes, G. A., In-zeolites Prepared by Oxidative Solid State Ion Exchange (OSSIE): Surface Species and Structural Characterization. *Microporous Mesoporous. Mater.* **2010**, 129, (1-2), 74-81.
26. Trejda, M.; Wojtaszek, A.; Floch, A.; Wojcieszak, R.; Gaigneaux, E. M.; Ziolek, M., New Nb and Ta-FAU Zeolites-Direct Synthesis, Characterisation and Surface Properties. *Catal. Today* **2010**, 158, (1-2), 170-177.
27. Brandenberger, S.; Kroeher, O.; Tissler, A.; Althoff, R., Effect of Structural and Preparation Parameters on the Activity and Hydrothermal Stability of Metal-Exchanged ZSM-5 in the Selective Catalytic Reduction of NO by NH₃. *Ind. Eng. Chem. Res.* **2011**, 50, (8), 4308-4319.
28. Danilina, N.; Payrer, E. L.; Troussard, E.; van Bokhoven, J. A., Selective Production of 2-Phenylhexane from Benzene and n-Hexane Over Pt- and Ga-Modified Zeolites. *Catal. Lett.* **2011**, 141, (3), 391-399.
29. Zhang, L.; Primera-Pedrozo, J. N.; Hernandez-Maldonado, A. J., Thermal Detemplation of Na-SAPO-34: Effect on Sr²⁺ Ion Exchange and CO₂ Adsorption. *J. Phys. Chem. C* **2010**, 114, (35), 14755-14762.
30. Rivera-Ramos, M. E.; Hernandez-Maldonado, A. J., Adsorption of N₂ and CH₄ by Ion-Exchanged Silicoaluminophosphate Nanoporous Sorbents: Interaction with Monovalent, Divalent, and Trivalent Cations. *Ind. Eng. Chem. Res.* **2007**, 46, (14), 4991-5002.

31. Rivera-Ramos, M. E.; Ruiz-Mercado, G. J.; Hernandez-Maldonado, A. J., Separation of CO₂ from Light Gas Mixtures Using Ion-Exchanged Silicoaluminophosphate Nanoporous Sorbents. *Ind. Eng. Chem. Res.* **2008**, 47, (15), 5602-5610.
32. Vomscheid, R.; Briend, M.; Peltre, M. J.; Man, P. P.; Barthomeuf, D., The Role of the Template in Directing the Si Distribution in SAPO Zeolites. *J. Phys. Chem.* **1994**, 98, (38), 9614-9618.
33. Maple, M. J.; Williams, C. D., Separating Nitrogen/Methane on Zeolite-Like Molecular Sieves. *Microporous Mesoporous. Mater.* **2008**, 111, (1-3), 627-631.
34. Briend, M.; Vomscheid, R.; Peltre, M. J.; Man, P. P.; Barthomeuf, D., Influence of the Choice of the Template on the Short-Term and Long-Term Stability of SAPO-34 Zeolite. *J. Phys. Chem.* **1995**, 99, (20), 8270-8276.
35. Dyer, A., Ion-Exchange Capacity. *Microporous Mesoporous. Mater.* **1998**, 22, (4-6), 543-545.
36. Joshi, U. D.; Joshi, P. N.; Tamhankar, S. S.; Joshi, V. V.; Rode, C. V.; Shiralkar, V. P., Effect of Nonframework Cations and Crystallinity on the Basicity of NaX Zeolites. *Appl. Catal. A-Gen.* **2003**, 239, (1-2), 209-220.
37. Kosanovic, C.; Bronic, J.; Subotic, B.; Smit, I.; Stubicar, M.; Tonejc, A.; Yamamoto, T., Mechanochemistry of Zeolites: 1. Amorphization of Zeolite-A and Zeolite-X and Synthetic Mordenite by Ball-Milling. *Zeolites* **1993**, 13, (4), 261-268.
38. Kosanovic, C.; Cizmek, A.; Subotic, B.; Smit, I.; Stubicar, M.; Tonejc, A., Mechanochemistry of Zeolites: 4. Influence of Cations on the Rate of Amorphization of Zeolite-A by Ball-Milling. *Zeolites* **1995**, 15, (7), 632-636.
39. Hutson, N. D.; Reisner, B. A.; Yang, R. T.; Toby, B. H., Silver Ion-Exchanged Zeolites Y, X, and Low-Silica X: Observations of Thermally Induced Cation/Cluster Migration and the Resulting Effects on the Equilibrium Adsorption of Nitrogen. *Chem. Mater.* **2000**, 12, (10), 3020-3031.
40. Yang, R. T., *Adsorbents: Fundamental and Applications*. John Wiley & Sons, Inc.: New York, 2003.
41. Breck, D. W., *Zeolite Molecular Sieves*. Wiley: New York, 1973.
42. Karge, H.; Wichterlová, B.; Beyer, H., High-Temperature Interaction of Solid Cu Chlorides and Cu Oxides in Mixtures with H-Forms of ZSM-5 and Y Zeolites. *J. Chem. Soc. Faraday T.* **1992**, 88, (9), 1345-1351.
43. Xie, Y. C.; Tang, Y. Q., Spontaneous Monolayer Dispersion of Oxides and Salts onto Surfaces of Supports: Application to Heterogeneous Catalysis. *Adv. Catal.* **1990**, 37 1-43.
44. Petunchi, J.; Marcelin, G.; Hall, W., Studies of the Changes Occurring on Reduction and Reoxidation of Cu-Y Zeolites. *J. Phys. Chem.* **1992**, 96, (24), 9967-9975.
45. Schoonheydt, R.; Roodhooft, D., Spectroscopy of the Thermal Reduction of Ni(II) in the Presence of H₂ in Zeolites X and Y. *J. Phys. Chem.* **1986**, 90, (23), 6319-6323.
46. Valyon, J.; Hall, W., Effects of Reduction and Reoxidation on the Infrared-Spectra from Cu-Y and Cu-ZSM-5 Zeolites. *J. Phys. Chem.* **1993**, 97, (27), 7054-7060.

47. Watanabe, Y.; Koiwai, A.; Takeuchi, H.; Hyodo, S.; Noda, S., Multinuclear NMR Studies on the Thermal Stability of SAPO-34. *J. Catal.* **1993**, 143, (2), 430-436.
48. Wyckoff, R. W. G., *Crystal Structures*. Interscience Publishers: New York, 1963; Vol. 1.
49. Bryce, D. L.; Bultz, E. B., Alkaline Earth Chloride Hydrates: Chlorine Quadrupolar and Chemical Shift Tensors by Solid-State NMR Spectroscopy and Plane Wave Pseudopotential Calculations. *Chem.-Eur. J.* **2007**, 13, (17), 4786-4796.
50. Heemsoth, J.; Tegeler, E.; Roessner, F.; Hagen, A., Generation of Active Sites for Ethane Aromatization in ZSM-5 Zeolites by a Solid-State Reaction of Zinc Metal with Brønsted Acid Sites of the Zeolite. *Microporous Mesoporous. Mater.* **2001**, 46, (2-3), 185-190.
51. Lazar, K.; Palborbely, G.; Beyer, H. K.; Karge, H. G., Solid State Ion-Exchange in Zeolites: 5. NH₄-Y-Iron(II) Chloride. *J. Chem. Soc. Faraday T.* **1994**, 90, (9), 1329-1334.
52. Khelifa, A.; Benchehida, L.; Derriche, Z., Adsorption of Carbon Dioxide by X Zeolites Exchanged with Ni²⁺ and Cr³⁺: Isotherms and Isosteric Heat. *J. Colloid Interface Sci.* **2004**, 278, (1), 9-17.

Chapter 4

Location of Cationic Species in Alkaline Earth Metal Exchanged SAPO-34 Materials from Solid State ^1H MAS NMR and ^{23}Na MAS NMR Spectroscopy

The location of extraframework cations in Sr^{2+} and Ba^{2+} ion-exchanged chabazite type silicoaluminophosphate (SAPO-34) was estimated by means of ^1H and ^{23}Na magic angle spinning nuclear magnetic resonance (MAS NMR) spectroscopy and spectral deconvolution. Incorporation of the alkaline earth metal cations onto the SAPO framework was achieved via conventional liquid state ion exchange, coupled partial detemplation/solid-state ion exchange, and combination of both techniques. MAS NMR revealed that the level of ion exchange was limited by the presence of protons and sodium cations located in or near hexagonal prisms (site SI), which are forbidden for exchange of either of the alkaline metals due to steric and charge repulsion criteria. In addition, the presence of ammonium cations in the supercages facilitated the exchange of otherwise tenacious hydrogen by the alkaline earth metal as corroborated by unit cell compositional data as well as enhanced CO_2 adsorption at low partial pressures. The

extraframework ammonium species were produced from partial detemplation of the structure-directing agent employed for the SAPO-34 synthesis, tetraethylammonium (TEA^+).

4.1. Introduction

The incorporation of alkaline earth metal cations into the framework of silicoaluminophosphate-34 (SAPO-34) has resulted in promising materials for the selective removal of CO_2 at temperatures and pressures that approach ambient conditions,¹⁻³ particularly the variants containing Sr^{2+} and Ba^{2+} extra-framework cations.³⁻⁵ The sorbent is synergistically functionalized by the exposed Sr^{2+} or Ba^{2+} species and the small dimensions of the SAPO-34 cages, which when combined still do not provide transport resistance or pore blocking to the structure. Since the adsorption interactions are in the physisorption range, these sorbents can be fully regenerated by simple engineering methods (i.e., lowering pressure).⁵⁻⁷

Different approaches could be used to incorporate cations onto zeolitic frameworks. Techniques such as conventional and multi step liquid state ion exchange,^{5, 7} wetness impregnation⁸ as well as solid state ion exchange^{4, 9-11} have been studied to attain full exchange of the original charge-balancing species. However, full knowledge of the location and distribution of the charge-compensating cations inside zeolitic structures is of utmost importance to optimize ion exchange procedures and promote the occupancy of sites available for interaction with other extra-framework guest molecules or adsorbates (i.e. CO_2). To determine cations location inside zeolitic materials, studies usually rely on X-ray diffraction and structural refinement.¹²⁻¹⁶ However, determination of the structure is still a difficult task due to the presence of disordered structure configurations and low occupancy of cations. Another approach that has been proven to be powerful in the determination of cations location and distribution is

the use of molecular simulation such as Monte Carlo simulation in faujasite materials¹⁷⁻¹⁹ and density functional theory. Examples include description of Na⁺ mobility upon adsorption of chloroform in Faujasite,²⁰ prediction of extraframework cations site location preference in chabazite materials²¹ and evaluation of the adsorption of O₂ in cation exchanged materials,²² just to mention a few. Still, the assumption of a rigid and unique framework structure and allowing non-framework cations to move during the course of the simulation also limits its applicability to a wide variety of ion exchanged zeolitic materials.

On the other hand, solid-state magic angle spinning nuclear magnetic resonance (MAS NMR) spectroscopy is a powerful direct and efficient tool for probing cations location since the distribution of these controls the material framework electric fields.²³ In contrast to crystallography studies and molecular simulation, which heavily depend on strong computational efforts, MAS NMR allows determination of the location of cations by direct analysis of their local environment without the need of a model assumption. This approach has been successfully employed to describe the location of protons and cations in zeolite materials such as ZSM-5²⁴⁻²⁶ X²⁷ and Y²⁸⁻³⁰. For example, ²³Na MAS NMR was used to study the distribution of sodium ion in partially lanthanum-exchanged Na-Y zeolites.²⁸ Analysis of ²³Na MAS NMR and ²³Na 2D multiple-quantum (MQ) MAS NMR spectra revealed the occupation of at least three different sites in Na-Y zeolite in contrast with previous computational studies where only one occupied site was found.³⁰ Furthermore, using ¹H MAS NMR it has been possible to measure the concentration of acidic hydroxyl groups, Brønsted acid sites in silicoaluminophosphates,^{24, 31} and has been used to evaluate the hydration-dehydration effects and thermal treatments on the material.^{32, 33}

The scope of the present study is to estimate the location of extra-framework sodium and hydrogen cations in partially exchanged Sr^{2+} - and Ba^{2+} -SAPO-34 materials, prepared via conventional liquid state ion exchange and coupled partial detemplation and solid-state ion exchange, by means of ^1H and ^{23}Na MAS NMR experiments. The results will be used to explain the level of alkaline earth metal ion exchange onto the materials based on the location of both sodium and protons in the as-prepared and modified materials and to further explain the interaction between adsorbed CO_2 and the cations all based on the estimated location of the latter species.

4.2. Experimental Section

4.2.1. Samples Preparation

The crystalline material, TEA^+Na^+ -SAPO-34, was prepared via hydrothermal synthesis using tetraethylammonium hydroxide (TEAOH) as a structure directing agent (SDA) or template. A detailed description of the synthesis is available elsewhere.^{5, 7, 34} Detemplation was performed in partial or complete fashion via calcination in a computer controlled muffle furnace.^{35,36} Incorporation of ammonium cations was accomplished using the fully detemplated Na^+ -SAPO-34 and liquid state ion exchange (LSIE). The resulting sample was denominated NH_4^+ -SAPO-34. Alkaline earth metals (Sr^{2+} or Ba^{2+}) were introduced onto a fully detemplated SAPO-34 framework via LSIE using $\text{SrCl}_2 \cdot 6\text{H}_2\text{O}$ or BaCl_2 salts using the procedures described elsewhere.^{5, 7} The resulting samples were identified as either Sr^{2+} -SAPO-34 LSIE or Ba^{2+} -SAPO-34 LSIE.

Samples were also prepared via solid-state ion exchange (SSIE), where the process consisted essentially of thoroughly mixing the as-synthesized TEA^+Na^+ -SAPO-34 materials with either

$\text{SrCl}_2 \cdot 6\text{H}_2\text{O}$ or BaCl_2 in an agate mortar for 3 to 5 minutes and the resulting mixture thermally treated in a flow reactor under dry helium atmosphere. The thermal treatment was performed in two stages: (i) treatment at 430 °C for 15 hours to accomplish partial detemplation followed by (ii) treatment at 600 °C for 50 hours to accelerate the SSIE and remove any template tenacious residue.^{4, 11} The resulting samples were identified as either Sr^{2+} -SAPO-34 SSIE or Ba^{2+} -SAPO-34 SSIE. Some of the SSIE samples were also LSIE afterward either $\text{SrCl}_2 \cdot 6\text{H}_2\text{O}$ or BaCl_2 solutions to further exchange sodium.⁴

4.2.2. Compositional Analyses

The unit cell elemental composition data materials were estimated using the onboard EDX energy dispersive X-ray spectrometer of a JEOL JSM-6480LV instrument and using a voltage of 20.0 KV with a SUTW-Sapphire Detector. In addition, the alkaline earth metal content was measured using an Agilent 7500ce inductively coupled plasma mass spectrometry (ICP-MS) instrument.

4.1.3. Solid-state Magic Angle Spinning Nuclear Magnetic Resonance

^1H MAS NMR measurements were performed on a Bruker DMX 300 NMR spectrometer where the ^1H Larmor frequency is 300 MHz using a Bruker 4 mm double resonance MAS NMR probe. ^{23}Na MAS NMR measurements were carried out on an ultra-wide bore 21T magnet with a Bruker Avance II NMR console, where the ^{23}Na Larmor frequency is 237.85 MHz, using a 3.2 mm homemade double resonance MAS NMR probe. For the ^1H NMR analyses, the samples were spun at 10 kHz and the chemical shifts were referenced to the ^1H signal of adamantane at 0.6 ppm. The NMR experimental parameters used were pulse length of 1.0 μs ($\sim\pi/10$ small

angle pulse), td (the number of FID points) of 512, dwell time of 5 μ s, and 128 scans for signal accumulation with a recycle delay of 2 s. For ^{23}Na NMR the chemical shifts were referenced to a NaCl sample at 0 ppm. The NMR experimental parameters were: pulse length of 2 μ s ($\sim\pi/7$ small angle pulse), td of 1024, dwell time of 2 μ s, and 512 scans with a recycle delay of 5 s.

4.2.4. CO₂ Adsorption Equilibrium Isotherms

Carbon dioxide equilibrium isotherm data on barium-exchanged SAPO-34 materials at 25 °C were obtained employing a volumetric adsorption unit (Micromeritics ASAP 2020) outfitted with turbo molecular drag pumps. The gases used were CO₂ (Ultra High Purity Grade, Praxair) and He (High Purity Grade, Linde). Helium was used as a backfill gas after the sorbent degassing stage and removed via ultra-high vacuum prior to adsorption tests. All samples were pre-treated in vacuum at 375°C to remove water molecules strongly bound inside the structure. Adsorption data for the strontium-exchanged SAPO-34 materials were gathered from results published previously by Hernandez-Maldonado and co-workers.⁴

4.3. Results and Discussion

The estimation of the location of extraframework cations using MAS NMR studies heavily depends on the analysis of all the observed resonances. It is therefore imperative to keep in mind that, since in most zeolitic structures extraframework cations occupy more than one site, the resulting line shape of the spectra will require deconvolution to separate the resonances associated with the various sites^{24, 37}. The assignment of the deconvoluted resonances to specific cation sites in SAPO-34 zeolitic framework was initially based on crystallography studies available for natural chabazite.^{38, 39} In this material cations are known to occupy four main sites

within the chabazite cages as shown in Fig. 1. Site SI located at the center of the hexagonal prism, SII located at the center of the six-ring window, SII' at the cavity displaced from the six-ring window and SIII located near the center of the eight-ring window (see Figure 2.1).

4.3.1. ^1H MAS-NMR investigation of partially exchanged SAPO-34 samples

The ^1H spectrum of fully detemplated Na^+ -SAPO-34 presented in Fig. 4.1 consisted of three deconvoluted resonances at 4.8, 5.8, and -1.9 ppm. The resonance at 4.8 ppm was ascribed to the presence of water molecules adsorbed on Brønsted acid sites, Si-OH-Al centers, located near the eight-ring channels (i.e. SII, SII' and SIII).^{32, 40, 41} Meanwhile, the broader resonance at 5.8 ppm was assigned to the environments that are more strongly hydrogen-bonded to other framework sites or to sites within the small hexagonal prisms (i.e. SI).^{41, 42} The small signal at -1.9 ppm was associated to bridging hydroxyls coordinated to framework defects and the outer surface of the silicoaluminophosphate particles (e.g. Si-OH, P-OH, Al-OH)^{24, 32, 43}.

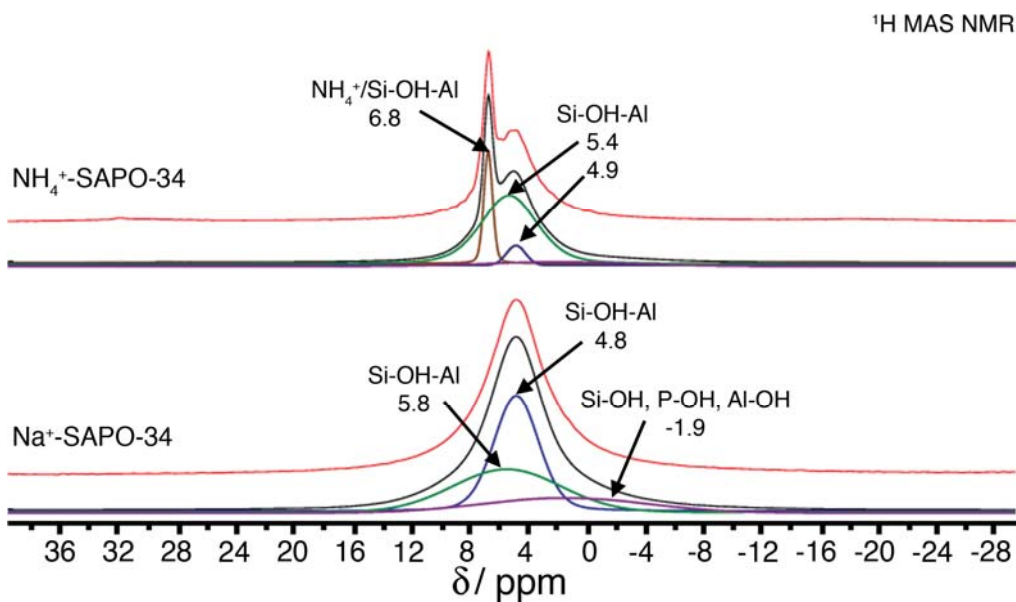


Figure 4.1. ^1H MAS NMR spectra recorded at 300 MHz for fully detemplated Na^+ -SAPO-34 and NH_4^+ -SAPO-34 samples. The red line corresponds to the experimental data, while the black line corresponds to the simulated spectra. Blue, green, purple and brown lines correspond to the deconvoluted resonances. Chemical shifts are referred to an adamantane sample.

For NH_4^+ -SAPO-34, the ^1H NMR spectrum (top in Fig. 4.1) also contained the aforementioned resonances plus an additional sharp signal observed at 6.82 ppm, most likely related to the presence of ammonium ($\text{NH}_4^+/\text{Si-OH-Al}$).^{25, 44} Furthermore, the bands associated to hydrogen cations located in the supercages and the hexagonal prisms were also observed at 4.9 and 5.4 ppm, respectively.⁴⁵ The small peak corresponding to the former resonance is probably a result of faster motion associated with hydration conditions (i.e. SII, SII' and SIII).⁴⁵ The narrow peak corresponding to the former resonance is probably a result of decreased dipolar couplings of proton species due to fast exchange under hydration conditions (i.e. SII, SII' and SIII).⁴⁵ These results correlated well with the observed unit cell compositions (see Table 4.1), which exhibited considerable amounts of unexchanged protons (Na^+ -SAPO-34 vs. NH_4^+ -SAPO-34).

Table 4.1. Unit cell composition of fully detemplated and ion exchanged Na^+ -SAPO-34.

Sample	Description	Unit Cell Composition
Na^+ -SAPO-34	Calcined at 600 °C	$\text{Na}_{2.03}\text{H}_{3.09}[\text{Si}_{4.07}\text{Al}_{18.52}\text{P}_{13.41}\text{O}_{72}]$
NH_4^+ -SAPO-34	LSIE of Na^+ -SAPO-34	$\text{Na}_{0.96}\text{H}_{3.84}[\text{Si}_{4.16}\text{Al}_{18.32}\text{P}_{13.52}\text{O}_{72}]^a$
Sr^{2+} -SAPO-34 LSIE	LSIE of Na^+ -SAPO-34	$\text{Na}_{0.85}\text{Sr}_{1.16}\text{H}_{1.90}[\text{Si}_{4.16}\text{Al}_{18.46}\text{P}_{13.38}\text{O}_{72}]$
Sr^{2+} -SAPO-34 SSIE	SSIE of as-synthesized TEA^+ , Na^+ -SAPO-34 at 600 °C with ca. 10-wt% $\text{SrCl}_2 \cdot 6\text{H}_2\text{O}$	$\text{Na}_{1.56}\text{Sr}_{1.12}\text{H}_{1.29}[\text{Si}_{4.21}\text{Al}_{18.44}\text{P}_{13.35}\text{O}_{72}]$
Sr^{2+} -SAPO-34 SSIE-LSIE	SSIE of as-synthesized TEA^+ , Na^+ -SAPO-34 at 600 °C with ca. 10-wt% $\text{SrCl}_2 \cdot 6\text{H}_2\text{O}$ followed by LSIE	$\text{Na}_{0.97}\text{Sr}_{1.61}\text{H}_{0.96}[\text{Si}_{4.21}\text{Al}_{18.47}\text{P}_{13.32}\text{O}_{72}]$
Ba^{2+} -SAPO-34 LSIE	LSIE of Na^+ -SAPO-34	$\text{Na}_{1.08}\text{Ba}_{1.77}\text{H}_{0.91}[\text{Si}_{4.31}\text{Al}_{18.38}\text{P}_{13.31}\text{O}_{72}]$
Ba^{2+} -SAPO-34 SSIE	SSIE of as-synthesized TEA^+ , Na^+ -SAPO-34 at 600 °C with ca. 10-wt% BaCl_2	$\text{Na}_{1.99}\text{Ba}_{0.26}\text{H}_{1.86}[\text{Si}_{4.73}\text{Al}_{17.83}\text{P}_{13.44}\text{O}_{72}]$
Ba^{2+} -SAPO-34 SSIE-LSIE	SSIE of as-synthesized TEA^+ , Na^+ -SAPO-34 at 600 °C with ca. 10-wt% BaCl_2 followed by LSIE	$\text{Na}_{0.55}\text{Ba}_{1.94}\text{H}_{0.77}[\text{Si}_{4.29}\text{Al}_{18.46}\text{P}_{13.25}\text{O}_{72}]$

Protons occupying SI sites are forbidden to exchange with ammonium cations due to steric considerations and should remain afterward. On the other hand, any proton located near the supercage was probably exchanged during the process and this could also be explained by the rather small resonance peak observed in the ^1H NMR spectrum of the NH_4^+ -SAPO-34 sample at 4.9 ppm (see Fig. 4.2). It should be mentioned that the ^1H NMR spectrum of the Na^+ -SAPO-34 sample treated for partial detemplation of TEA^+ (data not shown here) is similar to the one of NH_4^+ -SAPO-34. This is in agreement with the Fourier transformed infrared spectroscopy (FT-IR) studies performed by Zhang et al.,³⁶ where the formation of ammonium ions was followed during partial detemplation of SAPO-34 also prepared with TEA^+ .

Fig. 4.2 stacks the ^1H MAS NMR spectra for the Sr^{2+} and Ba^{2+} ion exchanged SAPO-34 samples. All the spectra appear to have a main resonance at approximately 4.8 ppm and can be assigned again to Si-OH-Al centers. Some small differences were also observed in the line width and relative intensity of the curves when compared to that of the fully detemplated Na^+ -SAPO-34 sample. Location of hydrogen cations in SI was observed for the SSIE and SSIE-LSIE samples, which exhibited resonances at 5.4 and 5.5 ppm, respectively, and corresponded to protons that would be forbidden to exchange with the alkaline earth metal cation due to steric and charge repulsion criteria. This matches well, again, with the compositional data shown in Table 4.1. However, the samples prepared via coupled partial detemplation and SSIE (i.e., Sr^{2+} -SAPO-34 SSIE and Ba^{2+} -SAPO-34 SSIE) have narrower MAS NMR spectra with similar hydrogen occupancies in either the hexagonal prisms or in the main SAPO-34 cages. It is important to mention that no major differences were observed in the ^1H MAS NMR spectra of the ion exchanged SAPO-34 materials, probably as a consequence of de-localized cations by the presence of water molecules. Furthermore, previous ^1H solid state NMR studies have

demonstrated that Brønsted acidity in SAPO-34 materials is not a constant and the acidity of the material is lost when exposed to moisture, these finding may also account for the variations in the hydrogen cation location in the samples²⁴.

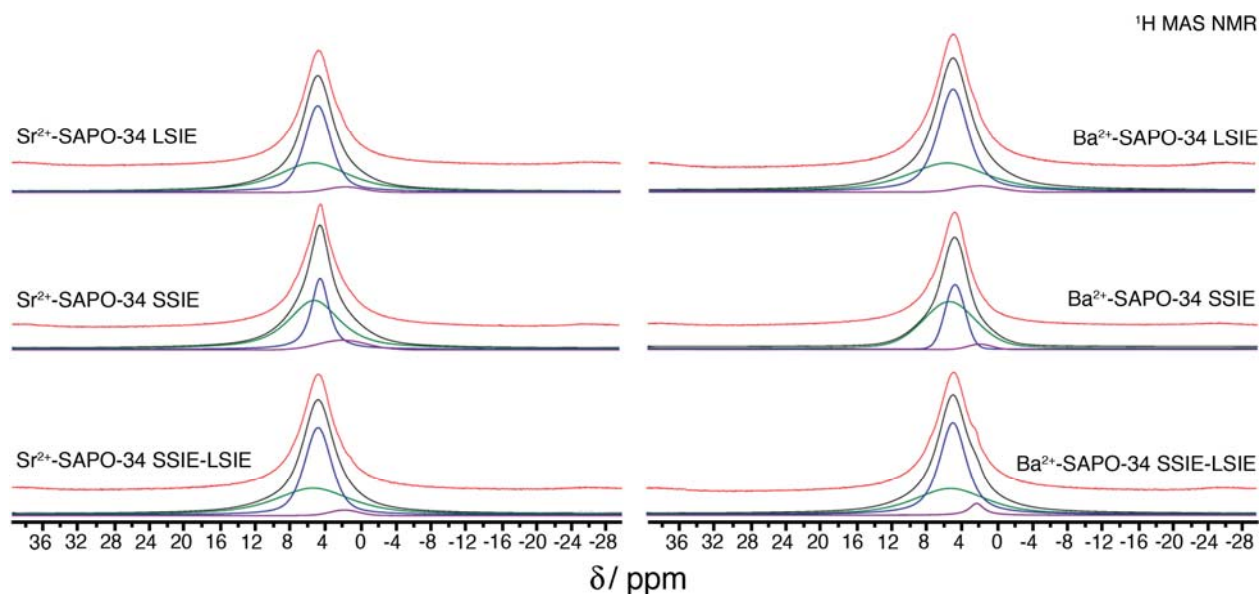


Figure 4.2. ^1H MAS NMR spectra recorded at 300 MHz for Sr^{2+} -SAPO-34 and Ba^{2+} -SAPO-34 samples prepared via LSIE, SSIE and SSIE-LSIE, respectively. The red line corresponds to the experimental data, while the black line corresponds to the simulated spectra. Blue, green and purple lines correspond to the deconvoluted resonances. Chemical shifts are referred to an adamantane sample.

4.3.2. ^{23}Na MAS-NMR investigation of partially exchanged SAPO-34 samples

Solid-state ^{23}Na MAS NMR is a very sensitive technique to determine the sodium local environment because the natural abundance of ^{23}Na nuclei and its quadrupole moment.²³ In order to minimize the second-order quadrupolar interaction and avoid the overlapping of the resonances, ^{23}Na MAS NMR measurements were performed at the ultra-wide bore 21 T magnet (i.e. 900 MHz) NMR spectrometer.

The ^{23}Na MAS NMR spectrum of a fully detemplated Na^+ -SAPO-34 sample (see Fig. 4.3) exhibited two resonances, a high field signal at approximately -19.9 ppm and a high field signal at -11.6 ppm. The former was ascribed to the Na^+ cations located in SI and the latter to the non-localized Na^+ cations and hydrated Na^+ cations located in the SAPO-34 supercages. The

narrower resonance at -11.6 ppm was probably a result of the relatively mobile hydrated Na^+ cations and the water molecules.³¹ Meanwhile, the NH_4^+ -SAPO-34 material showcased a single small resonance at -19.7 ppm, probably attributed to the sodium cations trapped in SI, each surrounded by six framework oxygen atoms. Further evidence of this sole sodium cation position in the ammonium-exchanged samples was provided by the unit cell composition data (see Table 4.1), which showed about 1 Na^+ remaining after exchanged. The only explanation for the survival of this center after exchange of the sample is that it occupied a site forbidden to ammonium (i.e., SI).

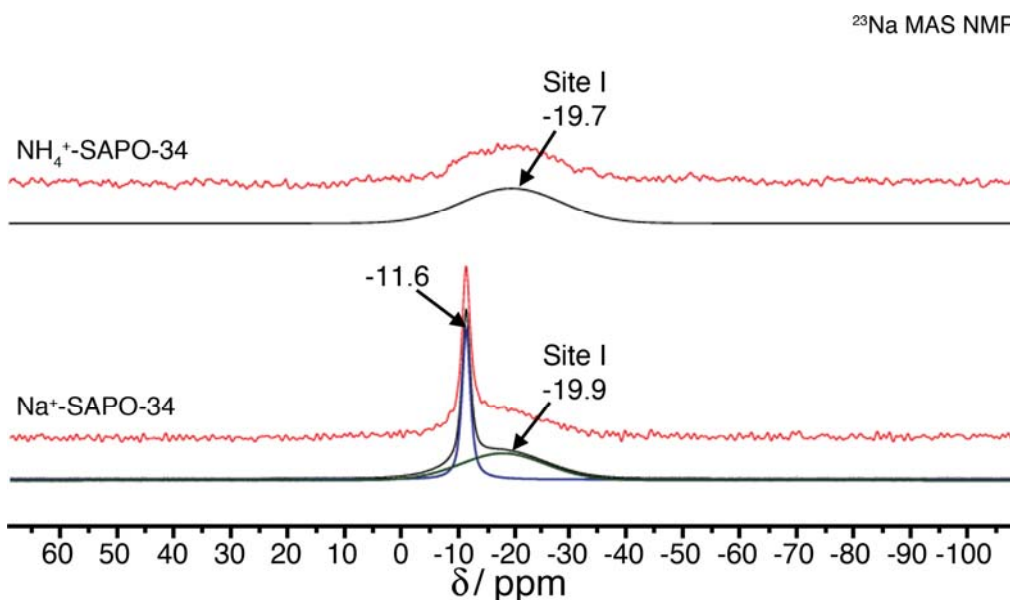


Figure 4.3. ^{23}Na MAS NMR spectra recorded at 900 MHz for fully detemplated Na^+ -SAPO-34 and NH_4^+ -SAPO-34 samples. The red line corresponds to the experimental data, while the black line corresponds to the simulated spectra. Blue and green lines correspond to the deconvoluted resonances. Chemical shifts are referred to a sodium chloride sample.

Fig. 4.4 shows the ^{23}Na MAS NMR spectra recorded for the Sr^{2+} and Ba^{2+} ion exchanged SAPO-34 materials. It is important to notice that, after deconvolution, a resonance signal at approximately -19 ppm corresponding to the Na^+ cations located in SI appeared to be common to all the ion exchanged samples, once again implying that the cations trapped in the SI site are difficult to be exchanged. In addition, all the samples that were prepared using SSIE probably

contained Na^+ cations located near the supercages as evidenced by a resonance located at ca. -11 ppm. In fact, a strong resonance related to sodium cations located in the supercages was observed for the Sr^{2+} -SAPO-34 SSIE-LSIE material. However, this resonance has negligible intensity in the ^{23}Na MAS NMR spectrum gathered for Ba^{2+} -SAPO-34 SSIE-LSIE sample (see Fig. 5). This could be due to sodium cations being forced to occupy sites near hexagonal prisms (SI) because barium cations would prefer sitting near the supercages due to their larger size when compared to that of strontium (1.80 vs. 2.15 Å). It should be mentioned that an additional resonance was observed for the Sr^{2+} -SAPO-34 SSIE sample at ~0 ppm and could be attributed to the presence of NaCl, the product of the high temperature solid-state reaction with $\text{SrCl}_2 \cdot 6\text{H}_2\text{O}$. However, this resonance was not observed for Ba^{2+} -SAPO-34 SSIE sample indicating that the exchanged reaction went to completion.

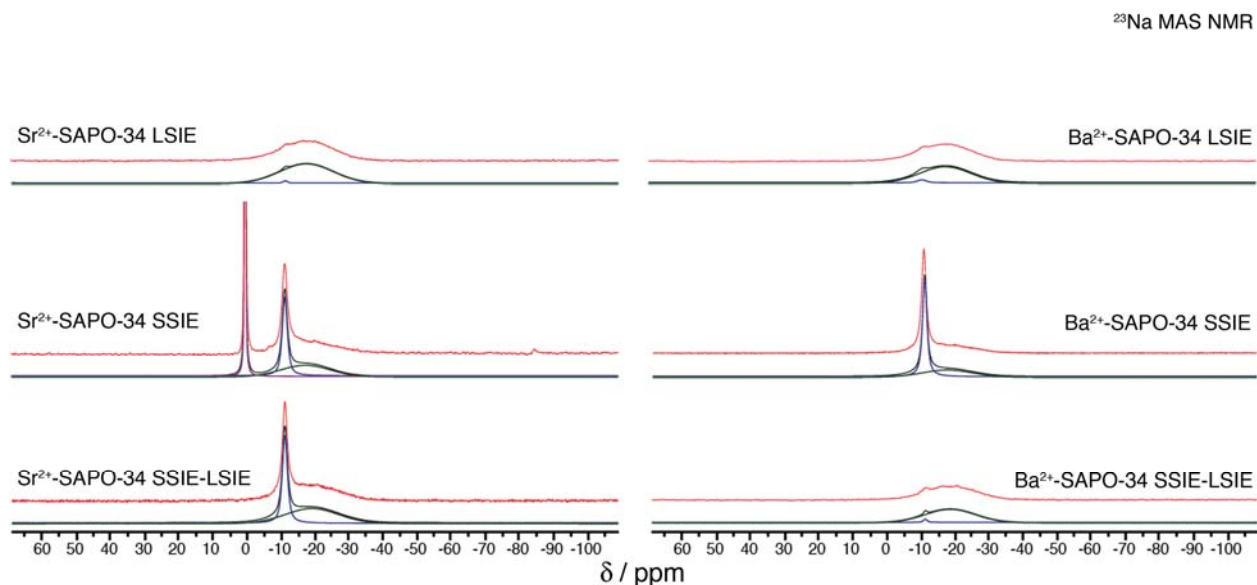


Figure 4.4. ^{23}Na MAS NMR spectra recorded at 900 MHz for Sr^{2+} -SAPO-34 and Ba^{2+} -SAPO-34 samples prepared via LSIE, SSIE and SSIE-LSIE, respectively. The red line corresponds to the experimental data, while the black line corresponds to the simulated spectra. Blue, green and purple lines correspond to the deconvoluted resonances. Chemical shifts are referred to a sodium chloride sample.

According to Table 4.1, the amount of sodium cations per unit cell in the strontium exchanged samples increases as follows: LSIE < SSIE-LSIE < SSIE. On the other hand, the

amount of hydrogen increases as follows: SSIE-LSIE < SSIE < LSIE. One possible explanation for this behavior is that the production of intermediary NH_4^+ species upon partial detemplation of TEA^+ permits the exchange of “hydrogen” by the alkaline earth metal before the formation of SI protons. Since the SSIE process will be limited by the amount of in-going cation source, the process was completed prior to the exchange of the sodium cations and hence the content of the unit cells in discussion (i.e., Na^+ occupying supercages). An analogous analysis could be made for the barium-exchanged samples with similar results, but the discussion will be omitted here to avoid redundancy.

4.3.4. Analysis of carbon dioxide pure component equilibrium adsorption

Fig. 4.5 shows pure component CO_2 adsorption isotherms gathered at 25°C for Sr^{2+} -SAPO-34 and Ba^{2+} -SAPO-34 materials prepared via LSIE, SSIE and coupled SSIE-LSIE. The data are also compared to the results gathered for Na^+ -SAPO-34. The differences observed in the CO_2 adsorption capacity were associated to the availability and level of exposure (i.e., location) of the Sr^{2+} or Ba^{2+} adsorption sites. Such information could be inferred from the ^1H and ^{23}Na MAS NMR data shown previously.

For SSIE samples, a significant amount of Sr^{2+} or Ba^{2+} was incorporated onto SAPO-34 (see Table 1), especially in the latter variant. According to ^1H and ^{23}Na MAS NMR and compositional analyses, the exchange of the alkaline earth metal was enhanced by the formation of hydrogen-based species (i.e., NH_4^+) initially occupying sites located nearby the supercages and minimizing the formation of protons that occupy sites forbidden to the divalent cations. This is reflected in the low partial pressure region of the isotherms (see Fig. 4.5) where the adsorbate-adsorbate interactions are predominant. An increase in strontium or barium loading resulted in an increase in CO_2 loading. For the case of the samples prepared via coupled SSIE-LSIE, perhaps

the lower than anticipated uptake was due to the presence of sodium cations in the supercages (from analyses of NMR data shown in Fig. 5), which probably affected the whole surface interaction potential or electric field. This would affect the interaction with the CO₂ quadrupole moment, which would be predominant among the different surface potential specific contributions.^{3, 6}

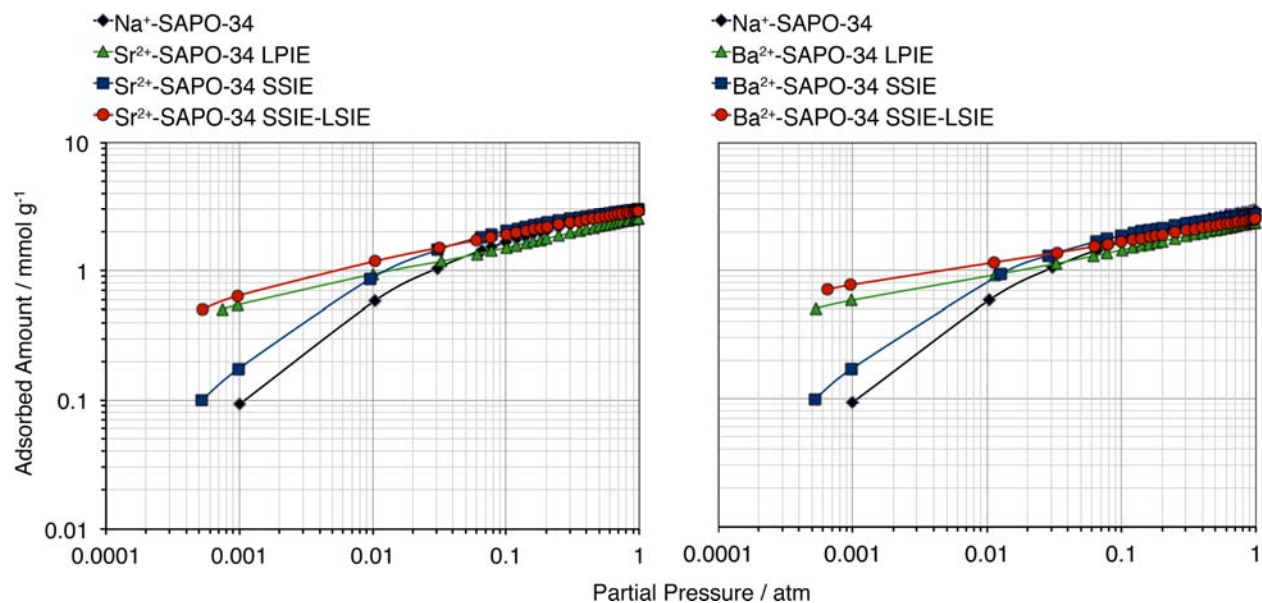


Figure 4.5. CO₂ adsorption isotherms obtained at 25 °C for Sr²⁺-SAPO-34 and Ba²⁺-SAPO-34 samples prepared via LSIE, SSIE and SSIE-LSIE, respectively. The figure also includes isotherm data gathered for a fully detemplated Na⁺-SAPO-34 material. Refer to Table 4.1 for sample description.

According to Fig. 4.5, both SSIE-LSIE samples adsorbed considerable amounts of CO₂ when compared to the other variants, with the barium-variant showing slightly better capacities at similar low partial pressures. The ²³Na MAS NMR analysis for the Sr²⁺-SAPO-34 SSIE-LSIE sample indicated that sodium cations occupy two unique sites, including the supercages. The Ba²⁺-SAPO-34 SSIE-LSIE sample, however, exhibited only sodium cations located in SI. This could explain the observed adsorption behavior since sodium cations that are present in the supercages might result in a smaller net surface electric field.

4.4. Conclusions

This work has demonstrated that ^1H and ^{23}Na MAS NMR experiments are extremely useful to corroborate the location of extra-framework cations in alkaline earth metal based SAPO-34 samples. Deconvolution analyses revealed resonances corresponding to unique H^+ and Na^+ sites with high and low symmetries located in or near the hexagonal prisms and in the supercages, respectively. When the NMR data is compared to compositional analyses, it is quite clear that the incorporation of alkaline earth metal is limited by the amount of out-going cations located in sites SI, which are forbidden to the divalent cations.

4.5. References

1. Hong, M.; Li, S.; Funke, H. F.; Falconer, J. L.; Noble, R. D., Ion-exchanged SAPO-34 membranes for light gas separations. *Microporous Mesoporous Mat.* **2007**, 106, (1-3), 140-146.
2. Li, S. G.; Falconer, J. L.; Noble, R. D., SAPO-34 membranes for CO_2/CH_4 separation. *J. Membrane Sci.* **2004**, 241, (1), 121-135.
3. Rivera-Ramos, M. E.; Ruiz-Mercado, G. J.; Hernandez-Maldonado, A. J., Separation of CO_2 from light gas mixtures using ion-exchanged silicoaluminophosphate nanoporous sorbents. *Ind. Eng. Chem. Res.* **2008**, 47, (15), 5602-5610.
4. Arevalo-Hidalgo, A. G.; Almodovar-Arbelo, N. E.; Hernandez-Maldonado, A. J., Sr^{2+} -SAPO-34 prepared via coupled partial detemplation and solid state ion exchange: Effect on textural properties and carbon dioxide adsorption. *Ind. Eng. Chem. Res.* **2011**, 50, (17), 10259-10269.
5. Arevalo-Hidalgo, A. G.; Santana, J. A.; Fu, R.; Ishikawa, Y.; Hernandez-Maldonado, A. J., Separation of CO_2 from light gas mixtures using nanoporous silicoaluminophosphate sorbents: Effect of multiple-step ion exchange and adsorption mechanism via computational studies. *Microporous Mesoporous Mat.* **2009**, 130, (1-3), 142-153.
6. Yang, R. T., *Adsorbents: Fundamental and Applications*. John Wiley & Sons, Inc.: New Jersey, 2003.
7. Rivera-Ramos, M. E.; Hernandez-Maldonado, A. J., Adsorption of N_2 and CH_4 by ion-exchanged silicoaluminophosphate nanoporous sorbents: Interaction with monovalent, divalent, and trivalent cations. *Ind. Eng. Chem. Res.* **2007**, 46, (14), 4991-5002.
8. Obrzut, D. L.; Adekkanattu, P. M.; Thundimadathil, J.; Liu, J.; Dubois, D. R.; Guin, J. A., Reducing methane formation in methanol to olefins reaction on metal impregnated SAPO-34 molecular sieve. *React. Kinet. Catal. L.* **2003**, 80, (1), 113-121.

9. Neinska, Y.; Minchev, C.; Kosova, L.; Kanazirev, V.; H.K. Beyer, H. G. K. I. K.; Nagy, J. B., Solid state modification of as-synthesized SAPO molecular sieves with indium. In *Studies in Surface Science and Catalysis*, Elsevier: 1995; Vol. Volume 94, pp 262-269.
10. Zamaro, J. M.; Miro, E. E.; Boix, A. V.; Martinez-Hernandez, A.; Fuentes, G. A., In-zeolites prepared by oxidative solid state ion exchange (OSSIE): Surface species and structural characterization. *Microporous Mesoporous Mat.* **2010**, 129, (1-2), 74-81.
11. Weitkamp, J.; Ernst, S.; Bock, T.; Kromminga, T.; Kiss, A.; Kleinschmit, P. Modified molecular sieves by means of solid ion exchange. 1996.
12. Kim, J. J.; Kim, C. W.; Sen, D.; Heo, N. H.; Seff, K., The pentagallium cation in zeolite y. preparation and crystal structure of $\text{Ga}_{42}\text{Tl}_{9,3}\text{-Si}_{121}\text{Al}_{71}\text{O}_{384}$ containing Ga_5^{7+} , Ga^+ , Ga^{2+} , Ga^{3+} , and Tl^+ . *J. Phys. Chem. C* **2011**, 115, (6), 2750-2760.
13. Zhu, L.; Seff, K., Cation crowding in zeolites. Reinvestigation of the crystal structure of dehydrated potassium-exchanged zeolite X. *J. Phys. Chem. B* **2000**, 104, (38), 8946-8951.
14. Martucci, A.; Alberti, A.; Guzman-Castillo, M. D.; Di Renzo, F.; Fajula, F., Crystal structure of zeolite omega, the synthetic counterpart of the natural zeolite mazzite. *Microporous Mesoporous Mat.* **2003**, 63, (1-3), 33-42.
15. Nakatsuka, A.; Okada, H.; Fujiwara, K.; Nakayama, N.; Mizota, T., Crystallographic configurations of water molecules and exchangeable cations in a hydrated natural CHA-zeolite (chabazite). *Microporous Mesoporous Mat.* **2007**, 102, (1-3), 188-195.
16. Yakubovich, O. V.; Massa, W.; Gavrilenko, P. G.; Pekov, I. V., Crystal structure of chabazite K. *Crystallogr. Rep.* **2005**, 50, (4), 544-553.
17. Calero, S.; Dubbeldam, D.; Krishna, R.; Smit, B.; Vlugt, T. J. H.; Denayer, J. F. M.; Martens, J. A.; Maesen, T. L. M., Understanding the role of sodium during adsorption: A force field for alkanes in sodium-exchanged faujasites. *J. Am. Chem. Soc.* **2004**, 126, (36), 11377-11386.
18. Beauvais, C.; Guerrault, X.; Coudert, F. X.; Boutin, A.; Fuchs, A. H., Distribution of sodium cations in faujasite-type zeolite: A canonical parallel tempering simulation study. *J. Phys. Chem. B* **2004**, 108, (1), 399-404.
19. Buttefey, S.; Boutin, A.; Mellot-Draznieks, C.; Fuchs, A. H., A simple model for predicting the Na^+ distribution in anhydrous NaY and NaX zeolites. *J. Phys. Chem. B* **2001**, 105, (39), 9569-9575.
20. Ramsahye, N. A.; Bell, R. G., Cation mobility and the sorption of chloroform in zeolite NaY: Molecular dynamics study. *J. Phys. Chem. B* **2005**, 109, (10), 4738-4747.
21. Civalieri, B.; Ferrari, A. M.; Llundell, M.; Orlando, R.; Merawa, M.; Ugliengo, P., Cation selectivity in alkali-exchanged chabazite: An ab initio periodic study. *Chem. Mater.* **2003**, 15, (21), 3996-4004.
22. Perez-Badell, Y.; Solans-Monfort, X.; Sodupe, M.; Montero, L. A., A DFT periodic study on the interaction between O_2 and cation exchanged chabazite MCHA ($\text{M} = \text{H}^+$, Na^+ or Cu^+): Effects in the triplet-singlet energy gap. *Phys. Chem. Chem. Phys.* **2009**, 12, (2), 442-452.

23. Hunger, M.; Brunner, E.; Karge, H. G.; Weitkamp, J., NMR Spectroscopy Characterization I. In Springer Berlin / Heidelberg: 2004; Vol. 4, pp 2733-2734.
24. Wang, X. W.; Coleman, J.; Jia, X.; White, J. L., Quantitative investigations of acidity, and transient acidity, in zeolites and molecular sieves. *J. Phys. Chem. B* **2002**, 106, (19), 4941-4946.
25. Xu, M. C.; Harris, K. D. M.; Thomas, J. M., In situ solid-state ^1H NMR studies of hydration of the solid acid catalyst ZSM-5 in its ammonium form. *Solid State Nucl. Mag.* **2009**, 35, (2), 93-99.
26. Zhang, W. P.; Bao, X. H.; Guo, X. W.; Wang, X. S., A high-resolution solid-state NMR study on nano-structured HZSM-5 zeolite. *Catal. Lett.* **1999**, 60, (1-2), 89-94.
27. Lim, K. H.; Grey, C. P., Characterization of extra-framework cation positions in zeolites NaX and NaY with very fast ^{23}Na MAS and multiple quantum MAS NMR spectroscopy. *J. Am. Chem. Soc.* **2000**, 122, (40), 9768-9780.
28. Lin, C. F.; Chao, K. J., Cation location in La,Na-Y zeolites by 2-dimensional ^{23}Na nutation NMR. *J. Phys. Chem.* **1991**, 95, (23), 9411-9415.
29. Sanchez-Sanchez, M.; Blasco, T., Investigation on the nature of the adsorption sites of pyrrole in alkali-exchanged zeolite Y by nuclear magnetic resonance in combination with infrared spectroscopy. *J. Am. Chem. Soc.* **2002**, 124, (13), 3443-3456.
30. Gueudre, L.; Quoineaud, A. A.; Pirngruber, G.; Leflaive, P., Evidence of multiple cation site occupation in zeolite NaY with high Si/Al ratio. *J. Phys. Chem. C* **2008**, 112, (29), 10899-10908.
31. Zibrowius, B.; Löffler, E.; Hunger, M., Multinuclear MAS NMR and IR spectroscopic study of silicon incorporation into SAPO-5, SAPO-31, and SAPO-34 molecular sieves. *Zeolites* **1992**, 12, (2), 167-174.
32. Buchholz, A.; Wang, W.; Arnold, A.; Xu, M.; Hunger, M., Successive steps of hydration and dehydration of silicoaluminophosphates H-SAPO-34 and H-SAPO-37 investigated by in situ CF MAS NMR spectroscopy. *Microporous Mesoporous Mat.* **2003**, 57, (2), 157-168.
33. Buchholz, A.; Wang, W.; Xu, M.; Arnold, A.; Hunger, M., Thermal stability and dehydroxylation of Brønsted acid sites in silicoaluminophosphates H-SAPO-11, H-SAPO-18, H-SAPO-31, and H-SAPO-34 investigated by multi-nuclear solid-state NMR spectroscopy. *Microporous Mesoporous Mat.* **2002**, 56, (3), 267-278.
34. Briend, M.; Peltre, M. J.; Massiani, P.; Man, P. P.; Vomscheid, R.; Derewinski, M.; Barthomeuf, D. In Modifications of Structure and Si Environment Upon Heating of SAPO-5, SAPO-34, and SAPO-37, Garmisch Partenkir, Germany, Jul 17-22, 1994; Weitkamp, J.; Karge, H. G.; Pfeifer, H.; Holderich, W., Eds. Garmisch Partenkir, Germany, 1994; pp 613-620.
35. Briend, M.; Vomscheid, R.; Peltre, M. J.; Man, P. P.; Barthomeuf, D., Influence of the choice of the template on the short-term and long-term stability of SAPO-34 zeolite. *J. Phys. Chem.* **1995**, 99, (20), 8270-8276.

36. Zhang, L.; Primera-Pedrozo, J. N.; Hernandez-Maldonado, A. J., Thermal detemplation of Na-SAPO-34: Effect on Sr^{2+} ion exchange and CO_2 adsorption. *J. Phys. Chem. C* **2010**, 114, (35), 14755-14762.
37. Metz, K. R.; Lam, M. M.; Webb, A. G., Reference deconvolution: A simple and effective method for resolution enhancement in nuclear magnetic-resonance spectroscopy. *Concept. Magnetic Res.* **2000**, 12, (1), 21-42.
38. Mortier, W. J.; Commission, I. Z. A. S., *Compilation of extra framework sites in zeolites*. Butterworth Scientific Limited on behalf of the Structure Commission of the International Zeolite Association: 1982.
39. Djieugoue, M. A.; Prakash, A. M.; Kevan, L., Electron spin resonance and electron spin echo modulation studies on reducibility, location, and adsorbate interactions of N(I) in Ni(II)-exchanged SAPO-34. *J. Phys. Chem. B* **1998**, 102, (22), 4386-4391.
40. Liu, H. M.; Kao, H. M.; Grey, C. P., ^1H MAS and $^1\text{H}/^{27}\text{Al}$ TRAPDOR NMR studies of oxygen-zeolite interactions at low temperatures: Probing Bronsted acid site accessibility. *J. Phys. Chem. B* **1999**, 103, (23), 4786-4796.
41. Hunger, M.; Freude, D.; Pfeifer, H., Magic-angle spinning nuclear-magnetic-resonance studies of water-molecules adsorbed on Bronsted-acid and Lewis-acid sites in zeolites and amorphous silica-aluminas. *J. Chem. Soc. Faraday T.* **1991**, 87, (4), 657-662.
42. Batamack, P.; Doremieuxmorin, C.; Fraissard, J.; Freude, D., Broad-line and high-resolution NMR-studies concerning the hydroxonium ion in HZSM-5 zeolites. *J. Phys. Chem.* **1991**, 95, (9), 3790-3796.
43. Campbell, G. C.; Galya, L. G.; Beeler, A. J.; English, A. D., Effect of RF inhomogeneity upon quantitative solid-state NMR measurements. *J. Magn. Reson.* **1995**, 112, (2), 225-228.
44. Pfeifer, H.; Freude, D.; Hunger, M., Nuclear magnetic-resonance studies of the acidity of zeolites and related catalyst. *Zeolites* **1985**, 5, (5), 274-&.
45. Krishna, R.; Li, S.; van Baten, J. M.; Falconer, J. L.; Noble, R. D., Investigation of slowing-down and speeding-up effects in binary mixture permeation across SAPO-34 and MFI membranes. *Separation and Purification Technology* **2008**, 60, (3), 230-236.

Chapter 5

Synthesis of SAPO-34 Using Triethylamine as Structure Directing Agent to improve the Textural and Adsorptive Properties of the Sorbent Material

The use of organic amines as structure directing agents (SDA) clearly influences the subsequent ion exchange behavior of zeolitic materials. It is possible to control specific synthesis parameters related to ion exchange properties of the material by modifying the template nature and its subsequent removal of the material pores. In this chapter, H^+ -SAPO-34 material was synthesized using triethylamine as SDA, the synthesized material was characterized by using X-ray diffraction (XRD) and scanning electron microscopy (SEM) to verify its crystallinity and morphology, respectively. Energy analysis by X-ray diffraction (EDS) was performed to determine its composition and measurements of the surface area and CO_2 adsorption of the material were also made. Furthermore, a coupled TGA-FTIR analysis of triethylamine template decomposition was done to evaluate the possibility of partially decomposing the organic template and produce species available to ion exchange. The post-detemplation and ion exchange of the material could result in a sorbent with improved CO_2 adsorptive properties which are

going to be discussed in the following sections, including the comparison with the SAPO-34 materials previously presented.

5.1 Introduction

Nanoporous sorbents are usually prepared by hydrothermal synthesis crystallization. In the case of silicoaluminophosphates (SAPO) materials, a typical crystallization procedure involves the use of water, boehmite, orthophosphoric acid, colloidal silica as the source of T atoms ($T=Si^{4+}$, Al^{3+} and P^{5+}), a mineralizing agent (OH^-), and a structure-directing agent (SDA) such as alkylammonium cations or organic amines.¹ Several structure-directing agents are reported to be useful for SAPO-34 synthesis, including tetraethylammonium hydroxide,^{2,3} morpholine,⁴ diethylamine,^{5,6} piperidine,⁷ triethylamine,⁸⁻¹⁰ and mixing templating agents (i.e. multiple SDAs).^{11, 12}

Triethylamine has been proved to be a successful organic template directing the synthesis of SAPO-34 materials, for example it has been used to synthesize SAPO-34 for growing of polymer hydrogels and incorporated on cordierite honeycombs for catalysis applications.^{10, 13} It has also been used to synthesize H^+ -SAPO-34 for the catalytic conversion of chloromethane to light olefins.^{8, 14} Additionally some studies related to the synthesis of SAPO-34 and the effect of the silicon content to produce different silicon coordination environments have been also performed.⁹ Unfortunately, the influence of triethylamine and its decomposition mechanism in the SAPO-34 structure has not been reported, related to the subsequent ion exchange properties of the material. The present study aims to elucidate about those effects.

Based on the reported results in Chapter 4 and recent studies made by Zhang et al.¹⁴ on partial decomposition of tetraethylammonium hydroxide template in SAPO-34 material to produce the formation of larger protonated species exposed to Sr^{2+} ion exchange, this chapter study the triethylamine template decomposition in H^+ -SAPO-34 material and subsequent ion exchange to develop a material with improved textural and adsorptive properties. A detailed study of the sodium free H^+ -SAPO-34 material is presented, including a TGA-FTIR analysis of triethylamine template decomposition to evaluate the possibility of partially decomposing the organic template to produce species available for ion exchange. The synthesized material was characterized to determine its textural properties and the surface area and CO_2 adsorption capacity of the material.

5.2 Experimental Section

5.2.1 Sorbent Synthesis. SAPO-34 was prepared by the method described in reference ¹⁵ using pseudoboehmite (73 wt% Al_2O_3 Wako Chemicals Company), orthophosphoric acid (85 wt% H_3PO_4 Sigma Aldrich), colloidal silica (40.32 wt% SiO_2 Sigma Aldrich) and triethylamine (TEA Sigma Aldrich) as the template. The synthesis procedure for the gel preparation is described as follows. First, 27.3 g of boehmite were dissolved in 62.5 g of deionized water under stirring to form alumina sol. In a separate teflon beaker, 39.1 g of phosphoric acid and 50 g of water were mixed under stirring. Both solutions were mixed together. Then 17.2 g of triethylamine template were added, and later a mixture of 20.2 g of colloidal silica and 33.8 g of water was slowly added under vigorous stirring. The pH value of the resulting mixture was approximately 3.4, which was adjusted adding an excess of triethylamine template to obtain the CHA phase as will be discussed in more detail later. The resulting gel mixture was transferred

into an stainless-steel autoclave and it was aged for 24h at room temperature. Then it was heated and crystallized at 150°C for 24 h, after which the temperature was increased to 200°C for 72 h. The solid samples were obtained by centrifugation, and washed with 3 L of distilled-deionized water.

5.2.2 Sorbent Characterization. The materials were characterized by X-ray diffraction (XRD), energy dispersive analysis by X-ray diffraction (EDX), coupled thermogravimetric analysis and Fourier transform infrared spectroscopy (FTIR), and ^1H and ^{23}Na solid state magic angle spinning nuclear magnetic resonance (MAS-NMR). X-ray diffraction (XRD) patterns of the materials were obtained using a Rigaku UTIMA III X-ray diffraction (CuK_α) equipped with a crossbeam optics system and it was used to corroborate the crystallinity of the materials. The unit cell elemental composition data were obtained employing the onboard energy dispersive X-ray (EDX) spectrometer of a JEOL JSM-6480LV instrument using a voltage of 20.0 KV with a SUTW-sapphire detector. Solid-State ^1H Magic Angle Spinning Nuclear Magnetic Resonance (MAS-NMR) measurements were performed on an ultra-narrow bore 21T magnet with a Bruker DRX NMR console where the ^1H Larmor frequencies is 900 MHz and using an in-house made single resonance of 3.5 mm MAS-NMR probe, the samples were spun at 20 kHz. The chemical shifts were referenced to adamantane. For the TGA-FTIR analysis, a TA-Q500 microbalance was employed for gravimetric measurements where the samples were heated inside the chamber of the TGA unit from ambient temperature to 1000°C at a heating rate of 15°C/min using a constant helium (high purity grade, Praxair) flow of 60 mL/min. The gas exhaust of the TGA instrument was monitored and analyzed with FT-IR spectrometer setup consisted of a Nicolet 6700 Optical Spectrometer Mainframe connected to a Nicolet X700 TGA/IR interface module

with a high efficiency condensing and collection optics setup, a DLa TGS detector, a nickel-coated stainless steel gas cell and a heated transfer line.

5.2.3 Porosimetry Analyses and CO₂ Adsorption Equilibrium Isotherms. Effective material surface area values were measured for all H⁺-SAPO-34 variants. The textural property was estimated after evaluation of nitrogen equilibrium adsorption data gathered at -196°C in a static volumetric adsorption system (Micromeritics ASAP 2020) outfitted with turbo molecular drag pumps. Carbon dioxide equilibrium isotherm data were also obtained employing the volumetric adsorption unit described above. Gases used were CO₂ (ultrahigh purity grade, Praxair) and He (high purity grade, Linde). Helium was used as a backfill gas after the adsorbent degassing stage and removed via an ultrahigh vacuum prior to the adsorption tests. All samples were pretreated in vacuum at 375°C to remove water molecules strongly bound inside the structure. Carbon dioxide equilibrium tests were performed at 25°C and pressures up to 1 atm.

5.3 Results and Discussion

The development of an improved material for CO₂ adsorption based on the knowledge obtained in the previous chapters about partial detemplation and ion exchange is proposed in this chapter. For this purpose, the first challenge was to synthesize the silicoaluminophosphate (SAPO-34) using triethylamine as SDA and obtaining a pure chabazite (CHA) phase. In this respect, it is important to mention that the resulting synthesis mixture, according to the reported procedure, has a pH value of 3.3. After analyses with SEM and X-ray diffraction the material clearly shows the presence of an aluminophosphate phase (type AFI materials), which will be discussed extensively later. In order to obtain the desired CHA phase, the pH of the resulting synthesis gel was modified by using an excess of triethylamine template.¹⁶ As reported by Jhung

et. al. both CHA and AFI structures form with triethylamine template, and the CHA amount increases with increasing template concentration,¹⁷ the effect of the pH in the resulting synthesis product as well as the characterization of the material will be discussed below.

5.3.1 Synthesis Characterization

Table 5.1 presents the unit cell composition of fully detemplated H⁺-SAPO-34 materials prepared using different pH values of the synthesis mixture. As has been previously found for other zeolitic materials, the pH has a strong influence in the properties of the resulting as-synthesized material.¹⁶ The results indicate that an increment in the pH produced an increment in the surface area, pore volume and pore size of the material. For the samples with pH = 7.4 and 8.3, the compositional analyses of the latter reveals the presence of a higher silicon content, a reduced amount of phosphorous, and consequently a high hydrogen concentration than the sample prepared with a pH of 7.4. In the synthesis route of SAPO-34 material using TEA as template, silicon is usually incorporated at a later stage of the synthesis mechanism. The obtained results about the influence of the pH in the silicon incorporation in the synthesis gel could be associated to the participation of silicon in the crystal nucleation in the induction period of crystallization, in an early stage of the synthesis.^{5, 18}

The H⁺-SAPO-34 sample obtained with a pH = 8.3 has the higher surface area, pore volume and pore size of all the SAPO-34 compared with the reported materials in this thesis dissertation, corresponding to 809 m²/g, 0.34 cm³/g and 4.91 Å, respectively. It should be mentioned that the starting H⁺-SAPO-34 material for this study, in comparison with previously reported data^{10,18,19}, has a higher hydrogen content. The main difference between the synthesized SAPO-34 materials previously reported (i.e. Na⁺-SAPO-34 TEAOH) and the presented here is based in the use of a

different templating agent to avoid the presence sodium cations in the resultant material. Sodium cations are bigger than hydrogen cations and this could lead to higher surface areas in H⁺-SAPO-34, although the increment in the surface area was greater than 200 m²/g and it is considered a significant improvement in the textural properties of the material.

Table 5.1. Unit cell composition of fully detemplated H⁺-SAPO-34 samples, prepared using triethylamine as templating agent and different pH values.

Material	Unit Cell Composition	Surface Area (m ² /g)	Pore Volume HK (cm ³ /g)	Median pore width-HK (Å)
H ⁺ SAPO-34 TEA (pH=3.3)	Not measured	430	0.15	4.28
H ⁺ SAPO-34 TEA (pH=7.4)	H _{3.22} [Si _{4.03} Al _{17.60} P _{14.37} O ₇₂]	728	0.26	3.69
H ⁺ SAPO-34 TEA (pH=8.3)	H _{3.81} [Si _{4.37} Al _{17.72} P _{13.92} O ₇₂]	809	0.34	4.91

X-ray diffraction analyses presented in Figure 5.1 are useful to elucidate the crystalline properties of H⁺-SAPO-34 materials synthesized using different pH values of the synthesis gel. The results were compared with the one gathered for Na⁺-SAPO-34 material synthesized using TEAOH as template, reported in the previous chapters. From the analyzed samples, H⁺-SAPO-34 materials with a pH of the synthesis gel of 3.3 and 7.4 respectively, present a different phase corresponding to the AFI structure. Probably the obtained solids contains a mixture of both CHA and AFI materials associated to the presence of a SAPO-5 prephase.^{16, 17} On the other hand, Na⁺-SAPO-34 TEAOH and H⁺-SAPO34 TEA (pH=8.3) have the crystalline structure corresponding to CHA phase, the results also confirm that the template (i.e. TEAOH vs. TEA) have no effect in the position of the diffraction peaks, only in the intensity.²⁰

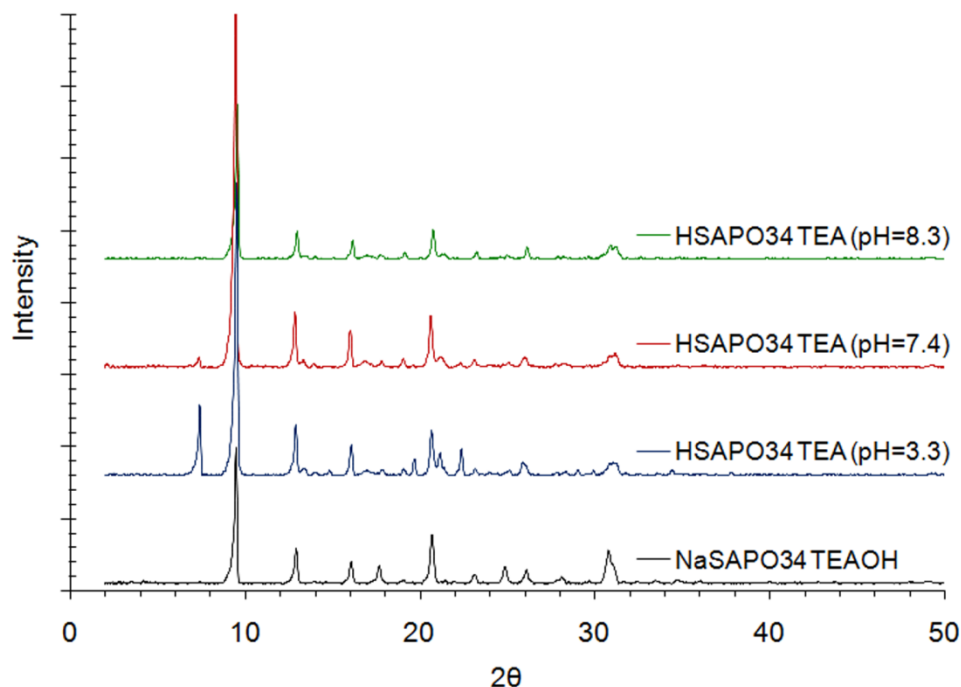


Figure 5.1. X-ray diffraction patterns for H^+ -SAPO-34 materials prepared using TEA as template and different synthesis pH values, the pattern for Na^+ -SAPO-34 synthesized using TEOH as template is also presented.

SEM micrographs were used to confirm the presence of a single phase (i.e. CHA) and evaluate the morphology of H^+ -SAPO-34 materials. Figure 2.3 presents the micrographs for H^+ -SAPO-34 TEA prepared with a synthesis pH of 8.3. The sample shows a single pure phase with cubic crystals characteristics of SAPO-34 materials, with slightly polydispersed crystals with 0.5-2.5 μm size approximately. When compared with SAPO-34 materials prepared using tetraethylammonium hydroxide,^{21,22} H^+ -SAPO-34 TEA material presents better textural properties. Furthermore, the use of triethylamine as SDA as observed in Figures 5.2, reduced the formation of unwanted side-products (i.e. amorphous silica or amorphous alumina) when compared with Na^+ -SAPO-34 materials prepared using TEOH as SDA and NaOH as stabilizing agent, respectively.

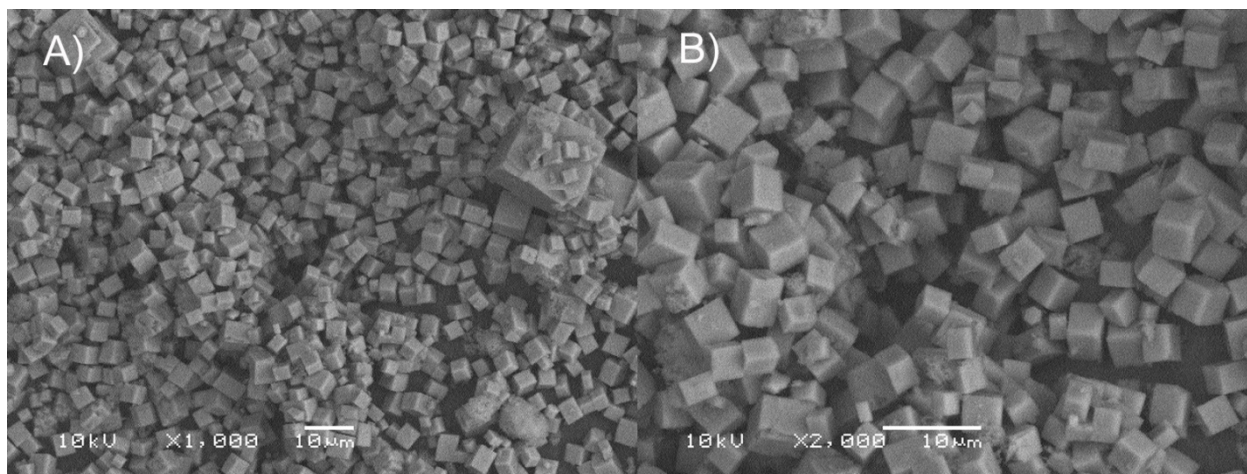


Figure 5.2. SEM images of H^+ -SAPO-34 (pH=8.3) synthesized using triethylamine as SDA.

This can be corroborated by the ^{27}Al and ^1H MAS-NMR (Figure 2.7 and Figure 4.1, respectively), presenting resonances associated to an amorphous phase in the as-synthesized TEAOH material. Figure 5.3 shows ^1H MAS-NMR spectra of H^+ -SAPO-34 (pH=8.3) recorded at 900 MHz, three resonances at 6.9, 5.3 and 3.3 ppm were observed corresponding to hydrogen ions located in three different environments.

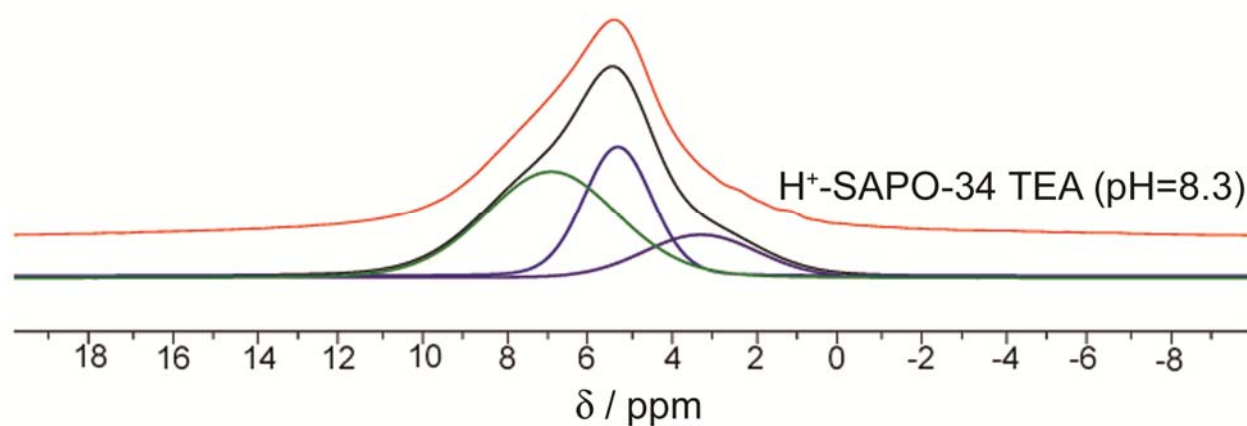


Figure 5.3. ^1H MAS-NMR spectra of H^+ -SAPO-34 (pH=8.3) recorded at 900 MHz synthesized using triethylamine as SDA.

The resonance at 5.3 ppm is attributed to hydrogen cations located in the hexagonal prism (i.e. Site I) and the resonances at 6.9 and 3.3 ppm are associated to hydrogen cations in Bronsted acid sites in the supercages,^{23, 24} the former is associated to environments that are more strongly hydrogen-bonded to other framework sites.²⁵ When compared with the calcined Na⁺-SAPO-34 TEAOH material (see Figure 4.1) an additional hydrogen environment is observed in H⁺-SAPO-34 sample at -6.9 ppm. It is also observed a different distribution of protons inside the material structure, predominantly located in Site I and near nearly octahedral coordination close to the hexagonal prisms.

5.2.3 TGA-FTIR Studies of Template Decomposition

To achieve ion exchange of the protons presented in the material structure, it is imperative to study the detemplation mechanism of triethylamine inside SAPO-34 material structure. The main challenge is to identify the formation of ion exchangeable species at specific temperatures during the detemplation process.²² For this purpose a coupled TGA/FT-IR study was made to evaluate the decomposition profile of triethylamine molecule and select a suitable temperature for PD mechanism of the as-synthesized H⁺-SAPO-34. Figure 5.4 shows the TGA profile of the as-synthesized SAPO-34 sample treated under helium. Three appreciable weight loss regions were observed. The first region (25 - 200 °C) was attributed to bulk water desorption from the sample; the second (200-700 °C), corresponds to triethylamine decomposition and the third region (700-1000 °C) to decomposition of remaining volatile impurities. Region III was formed by two decomposition steps possibly resulting from amine molecules that remains encaged in the pores up to 673 K under the conditions studied.²⁶

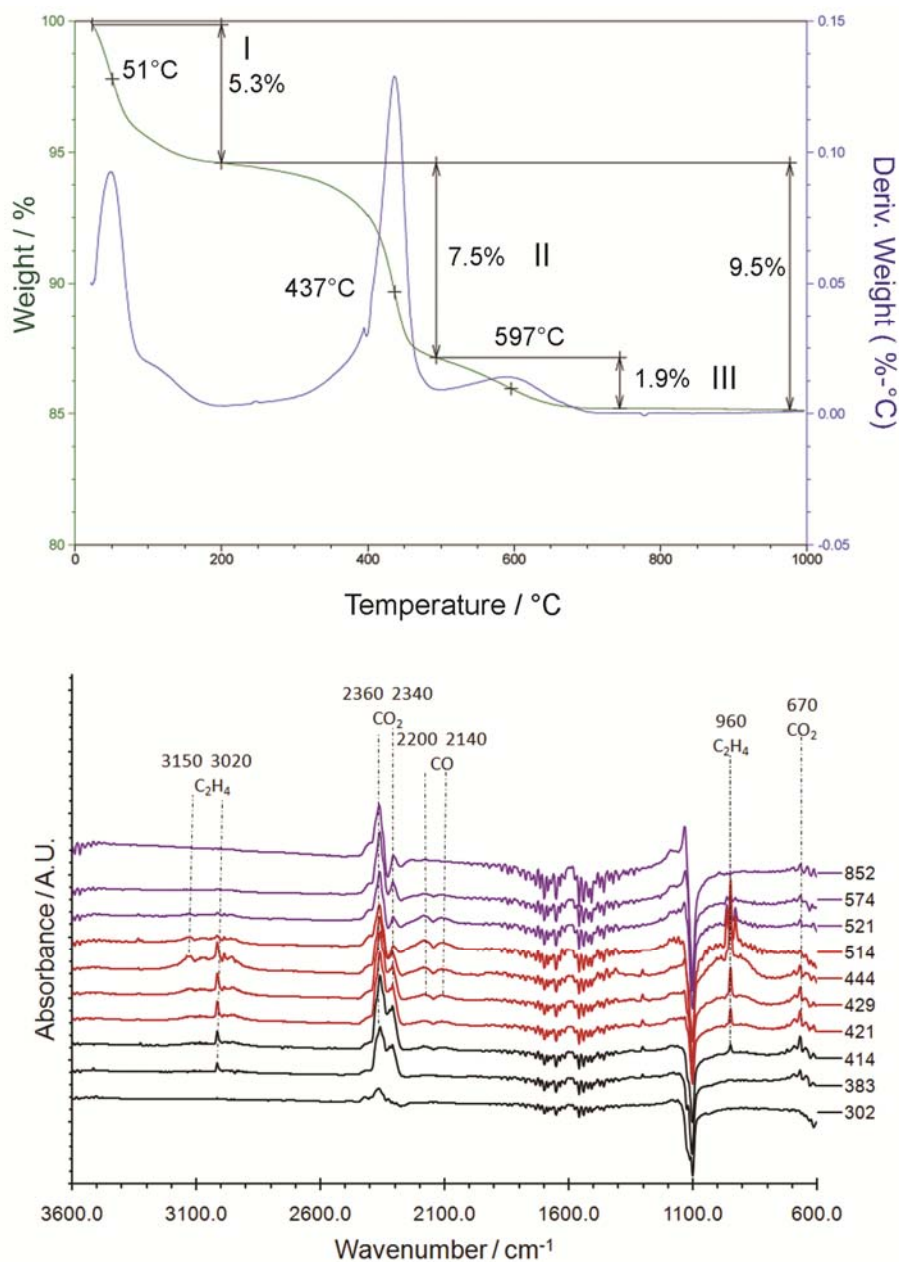


Figure 5.4. Coupled thermal gravimetric analyses (TGA) and Fourier transform infrared spectroscopy (FT-IR) spectra of the desorbed species arising from decomposition of TEA⁺ in H⁺-SAPO-34 (pH=8.3) under helium at various temperatures.

The corresponding transient FT-IR spectra stack (Figure 5.4) shows no apparent contributions from functional groups until a temperature of 383 °C is reached, corresponding to a TGA weight loss of 6.88%. The formation of C₂H₄ (3020 cm⁻¹) accompanied by an small amount of CO₂ is formed at this temperature as indicated by the characteristic IR bands (2340, 2360 and

670 cm^{-1}). At a temperature of approximately 414 °C, the TGA/FT-IR profiles show the formation of CO (2200 and 2140 cm^{-1}) plus what appears to be C_2H_4 (960 cm^{-1}). The thermal treatment results in a successive release of ethylene from the templating triethylamine molecules.²⁶ Although the gas medium employed was oxygen-free, Zhang et al. discussed the formation of CO_2 and CO as a result of the reaction between extra-lattice oxygen (ELO) available in the SAPO-34 framework and TEA^+ , produced during syntheses in aqueous media.²² Taking into consideration the aforementioned analysis, a suitable temperature for SSIE should be in the range of 380 and 520 °C with as-synthesized Na^+ -SAPO-34 as the basis material. Although diffuse reflectance infrared spectroscopy (DRIFT) studies should be addressed to corroborate the formation of a specie available to ion exchange with the functional surface species.

5.3.3 CO_2 Adsorption Performance

The carbon dioxide adsorption of fully detemplated H^+ -SAPO-34 (pH=8.3) at 25°C is presented in Figure 5.5 as well as the isotherm for the materials after exposure to ion exchange treatments. The CO_2 adsorption capacity of the material at 1 atm was 3.2 mmol/g which matches well with the value reported for Na^+ -SAPO-34 TEAOH.³ The isotherm shape, especially in the low partial pressure range, indicates the absence of functional surface species (e.g. Na^+ or metal cations) with a strong affinity toward CO_2 coupled with the location of hydrogen cations in inaccessible sites (i.e. Site I).

To prove the hypothesis previously postulated related to the preferential occupancy of hydrogen cations in the hexagonal prism, an attempt was made to incorporate strontium cations via liquid state ion exchange with an aqueous solution of $\text{SrCl}_2 \cdot 6\text{H}_2\text{O}$, as shown in Figure 5.5. After the ion exchange treatment and subsequent measurement of the CO_2 adsorption capacity of

the material, Figure 5.5 shows that incorporation of strontium cations was not achieved in the material. Thus, confirming the location of hydrogen cations for the fully detemplated H^+ -SAPO-34 in the hexagonal prisms, Site I.

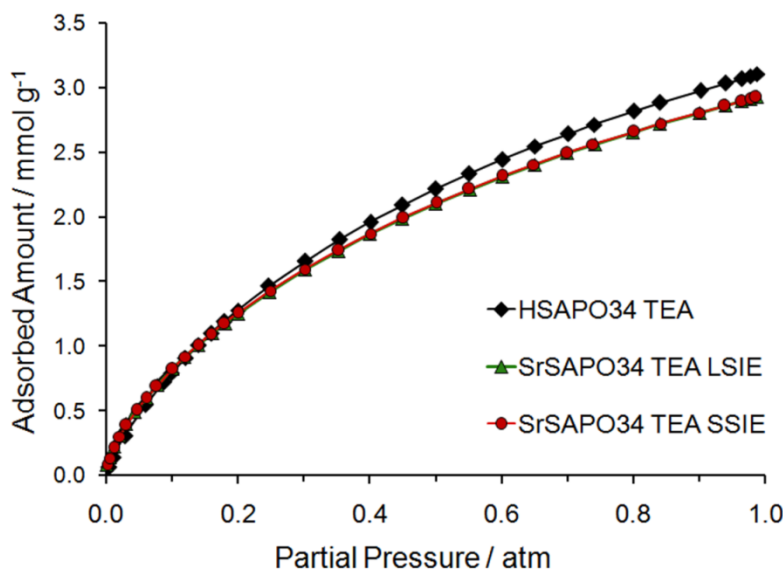


Figure 5.5. CO_2 adsorption isotherms obtained at 25 °C for H^+ -SAPO-34 and attempts to incorporate of strontium

Additionally, to incorporate Sr^{2+} metal cations in the H^+ -SAPO-34 material structure, based on the observed TGA-FTIR profile of triethylamine template inside SAPO-34 material, strontium chloride salt was mixed with the as-synthesized material and partial detemplation at 430°C followed by solid state ion exchange at 600 °C. This process was done to achieve diffusion of the strontium salt throughout the small SAPO-34 pores. However, no ion exchange was achieved under these conditions (see Figure 5.5), the thermal treatment was not successful to produce ion exchangeable species probably because hydrogen were located in Site I before the ion exchange occurred. Schnabel et. al., after studying the triethylamine template decomposition in SAPO-5 materials found that the template is progressively decomposed to lower amines and finally to ammonia²⁶ and these species cannot be readily exchanged per Sr^{2+} cations. Moreover,

a more detailed and rigorous study about triethylamine template decomposition in SAPO-34 materials should be performed to elucidate a suitable temperature to produce ion exchange of the species formed during partial detemplation of the material.

5.4 Conclusions

H⁺-SAPO-34 was successfully synthesized using triethylamine as structure directing agent. Crystallinity results indicate the formation of a pure CHA phase at pH values of 8.3 in the synthesis gel, at lower pH values was obtained an AFI phase. SEM micrographs confirm the presence of cubic crystals characteristics of SAPO-34 of 0.5-2.5 μm size. ¹H MAS-NMR indicate that hydrogen cations are predominantly located in Site I and nearly octahedral coordination close to the hexagonal prisms. Characterization of H⁺-SAPO-34 material with synthesis gel pH of 8.3 using TEA as template indicates an improvement in the textural properties of the material when compared with Na⁺-SAPO-34 using TEAOH as template. Additionally, CO₂ adsorption results of H⁺-SAPO-34 materials confirm the hypothesis proposed in the previous chapters of this dissertation about the preferential location of hydrogen in Site I and the difficulty of ion exchange species located in this site. Although, a comprehensive study (e.g. DRIFT studies) about detemplation mechanism of triethylamine template should be addressed to corroborate the production of species available to ion exchange and the suitable temperature for this happen.

References

1. Hammoudi, H.; Bendenia, S.; Marouf-Khelifa, K.; Marouf, R.; Schott, J.; Khelifa, A., Effect of the Binary and Ternary Exchanges on Crystallinity and Textural Properties of X Zeolites. *Micropor. Mesopor. Mat.* **2008**, 113, (1-3), 343-351.

2. Sato, K.; Nishimura, Y.; Matsubayashi, N.; Imamura, M.; Shimada, H., Structural Changes of Y Zeolites During Ion Exchange Treatment: Effects of Si/Al Ratio of the Starting NaY. *Micropor. Mesopor. Mat.* **2003**, 59, (2-3), 133-146.
3. Amari, D.; Ginoux, J. L.; Bonnetain, L., Textural Damage of Cation-Exchanged LTA Zeolites Studied by Gas-Adsorption. *Zeolites* **1994**, 14, (1), 58-64.
4. Fichtnerschmittler, H.; Lutz, W.; Amin, S.; Dyer, A.; Wark, M., Hydrothermal Damage of Ion-Exchanged A-type Zeolite Cation-Directed Mechanism of Phase-Transformation. *Zeolites* **1992**, 12, (6), 750-755.
5. Lok, B. M.; Messina, C. A.; Patton, R. L.; Gajek, R. T.; Cannan, T. R.; Flanigen, E. M. Crystalline Silicoaluminophosphates. 1984.
6. Rivera-Ramos, M. E.; Ruiz-Mercado, G. J.; Hernandez-Maldonado, A. J., Separation of CO₂ from Light Gas Mixtures using Ion-Exchanged Silicoaluminophosphate Nanoporous Sorbents. *Ind. Eng. Chem. Res.* **2008**, 47, (15), 5602-5610.
7. Rivera-Ramos, M. E.; Hernandez-Maldonado, A. J., Adsorption of N₂ and CH₄ by Ion-Exchanged Silicoaluminophosphate Nanoporous Sorbents: Interaction with Monovalent, Divalent, and Trivalent Cations. *Ind. Eng. Chem. Res.* **2007**, 46, (14), 4991-5002.
8. Vomscheid, R.; Briend, M.; Peltre, M. J.; Man, P. P.; Barthomeuf, D., The Role of the Template in Directing the Si Distribution in SAPO Zeolites. *J. Phys. Chem.* **1994**, 98, (38), 9614-9618.
9. Briend, M.; Vomscheid, R.; Peltre, M. J.; Man, P. P.; Barthomeuf, D., Influence of the Choice of the Template on the Short-Term and Long-Term Stability of SAPO-34 Zeolite. *J. Phys. Chem.* **1995**, 99, (20), 8270-8276.
10. Dyer, A., Ion-Exchange Capacity. *Micropor. Mesopor. Mat.* **1998**, 22, (4-6), 543-545.
11. Barros, M.; Araujo, I. F.; Arroyo, P. A.; Sousa-Aguiar, E. F.; Tavares, C. R. G. In *Multicomponent Ion Exchange Isotherms in NaX Zeolite*, Santa Fe, Argentina, Sep 16-20, 2001; Santa Fe, Argentina, 2001; pp 339-344.
12. Horvath, G.; Kawazoe, K., Method for the Calculation of Effective Pore Size Distribution in Molecular-Sieve Carbon. *J. Chem. Eng. Jpn.* **1983**, 16, (6), 470-475.
13. Rege, S. U.; Yang, R. T., Corrected Horvath-Kawazoe Equations for Pore-Size Distribution. *AIChE J.* **2000**, 46, (4), 734-750.
14. Lippens, B. C.; de Boer, J. H., Studies on Pore Systems in Catalysts V. The t-Method. *J. Catal.* **1965**, 4, (3), 319-323.
15. de Boer, J. H.; Linsen, B. G.; Osinga, T. J., Studies on Pore Systems in Catalysts VI. The Universal t-Curve. *J. Catal.* **1965**, 4, (6), 643-648.
16. de Boer, J. H.; Linsen, B. G.; van der Plas, T.; Zondervan, G. J., Studies on Pore Systems in Catalysts VII. Description of the Pore Dimensions of Carbon Blacks by the t-Method. *J. Catal.* **1965**, 4, (6), 649-653.
17. Hutson, N. D.; Reisner, B. A.; Yang, R. T.; Toby, B. H., Silver Ion-Exchanged Zeolites Y, X, and Low-Silica X: Observations of Thermally Induced Cation/Cluster Migration and the

- Resulting Effects on the Equilibrium Adsorption of Nitrogen. *Chem. Mater.* **2000**, 12, (10), 3020-3031.
18. Delley, B., An All-Electron Numerical Method for Solving the Local Density Functional for Polyatomic Molecules. *J. Chem. Phys.* **1990**, 92, (1), 508-517.
 19. Delley, B., From Molecules to Solids with the DMol³ Approach. *J. Chem. Phys.* **2000**, 113, (18), 7756-7764.
 20. Perdew, J. P.; Burke, K.; Ernzerhof, M., Generalized Gradient Approximation Made Simple. *Phys. Rev. Lett.* **1996**, 77, (18), 3865.
 21. Maple, M. J.; Williams, C. D., Separating Nitrogen/Methane on Zeolite-Like Molecular Sieves. *Micropor. Mesopor. Mat.* **2008**, 111, (1-3), 627-631.
 22. Fletcher, P.; Townsend, R. P., Exchange of Ammonium and Sodium-Ions in Synthetic Faujasites. *J. Chem. Soc. Farad. T. 1* **1982**, 78, 1741-1753.
 23. Djieugoue, M. A.; Prakash, A. M.; Kevan, L., Electron Spin Resonance and Electron Spin Echo Modulation Studies on Reducibility, Location, and Adsorbate Interactions of N(I) in Ni(II)-Exchanged SAPO-34. *J. Phys. Chem. B* **1998**, 102, (22), 4386-4391.
 24. Hunger, M.; Brunner, E., NMR Spectroscopy. *Mol. Sieves* **2004**, 4, 201-293.
 25. Vistad, O. B.; Akporiaye, D. E.; Taulelle, F.; Lillerud, K. P., In Situ NMR of SAPO-34 Crystallization. *Chem. Mater.* **2003**, 15, (8), 1639-1649.
 26. Buchholz, A.; Wang, W.; Xu, M.; Arnold, A.; Hunger, M., Thermal stability and dehydroxylation of Brønsted acid sites in silicoaluminophosphates H-SAPO-11, H-SAPO-18, H-SAPO-31, and H-SAPO-34 investigated by multi-nuclear solid-state NMR spectroscopy. *Micropor. Mesopor. Mat.* **2002**, 56, (3), 267-278.
 27. Blackwell, C. S.; Patton, R. L., Solid-State NMR of Silicoaluminophosphate Molecular-Sieves and Aluminophosphate Materials. *J. Phys. Chem.* **1988**, 92, (13), 3965-3970.
 28. Buchholz, A.; Wang, W.; Arnold, A.; Xu, M.; Hunger, M., Successive steps of hydration and dehydration of silicoaluminophosphates H-SAPO-34 and H-SAPO-37 investigated by in situ CF MAS NMR spectroscopy. *Micropor. Mesopor. Mat.* **2003**, 57, (2), 157-168.
 29. Xu, L.; Du, A. P.; Wei, Y. X.; Wang, Y. L.; Yu, Z. X.; He, Y. L.; Zhang, X. Z.; Liu, Z. M., Synthesis of SAPO-34 with only Si(4Al) Species: Effect of Si Contents on Si Incorporation Mechanism and Si Coordination Environment of SAPO-34. *Micropor. Mesopor. Mat.* **2008**, 115, (3), 332-337.
 30. Yan, Z. M.; Chen, B. H.; Huang, Y., A solid-state NMR study of the formation of molecular sieve SAPO-34. *Solid State Nucl. Mag.* **2009**, 35, (2), 49-60.
 31. Karge, H. G.; Beyer, H. K., *Solid-State Ion Exchange in Microporous and Mesoporous Materials*. Springer-Verlag: Berlin Heidelberg, 2002; Vol. 3.
 32. Yang, R. T., *Adsorbents: Fundamentals and Applications*. Wiley: New York, 2003.
 33. Khelifa, A.; Derriche, Z.; Bengueddach, A., Sorption of Carbon Dioxide by Zeolite X Exchanged with Zn²⁺ and Cu²⁺. *Micropor. Mesopor. Mat.* **1999**, 32, (1-2), 199-209.

Chapter 6

Concluding Remarks and Thesis Contributions

The aim of this dissertation was to contribute to the study of different approaches to incorporate Sr^{2+} and Ba^{2+} extraframework cations onto SAPO-34 crystal structure to improve the adsorptive properties of the material. The use of multi-step liquid phase ion exchange (LSIE) technique increased the concentration of the functional surface species in SAPO-34, although the procedure resulted in a detrimental effect of the CO_2 adsorptive behavior of the material. Moreover, the presence of solvated species and the interaction between the in-going cation and the available sites inside the structure resulted in an equilibrium limitation of the ion exchange technique. Thus, incorporation of Sr^{2+} and Ba^{2+} cations via conventional and multi-step ion exchanged into SAPO-34 material did not yield the maximum ion exchange capacity of the material. X-ray diffraction (XRD) studies of the ion exchanged SAPO-34 materials via LSIE indicated that the crystalline structure of SAPO-34 materials was preserved after the ion exchange treatments while ^{27}Al , ^{29}Si , ^{31}P magic angle spinning nuclear magnetic resonance (MAS-NMR) tests suggested possible damage of the local crystal structure from the

detemplation of the original material, but none from the ion exchange process. This hypothesis leads to the development of a novel coupled partial detemplation and solid state ion exchange mechanism (PD-SSIE) to incorporate metal cations in SAPO-34 material structure in a moisture free process, eliminating the equilibrium limitations found in LSIE technique. In terms of CO₂ adsorption performance, the Sr²⁺-SAPO-34 adsorbent material prepared via PD-SSIE exhibited the best uptake capacity at moderate gas partial pressure among different SSIE variants prepared. Finally, the preparation of Sr²⁺-SAPO-34 and Ba²⁺-SAPO-34 via SSIE followed by a liquid-state ion exchange (LSIE) treatment resulted in materials with a superior CO₂ adsorption capacity at all partial pressures.

Experimental results and DFT studies indicate that Sr²⁺ and Ba²⁺ cations are preferentially located in Site II' extra-framework positions, which allows a high interaction with CO₂ molecules. This was confirmed by ¹H and ²³Na MAS-NMR studies, elucidating the presence of H⁺ and Na⁺ cations in the supercages of the materials being available to Sr²⁺ and Ba²⁺ ion exchange. But it also revealed the presence of tenacious cations in SAPO-34 materials sitting in the hexagonal prisms (Site I) which makes extremely difficult to fully ion exchange H⁺ and Na⁺ cations.

Finally, it is proposed the study of triethylamine template decomposition and subsequent ion exchange in the sodium free H⁺-SAPO-34 material to improve the textural and adsorptive properties. Preliminary CO₂ adsorption results of ion exchanged H⁺-SAPO-34 materials confirmed the hypothesis about the preferential location of hydrogen in Site I.

Furthermore, our results have demonstrated that both Sr²⁺ and Ba²⁺-SAPO-34 materials are superior sorbents for the selective adsorption of CO₂ especially at low concentrations.

Appendix A

Ion exchanged Sr^{2+} - and Ba^{2+} -13X materials for Carbon Dioxide Adsorption Applications

Sr^{2+} and Ba^{2+} -13X materials were prepared via multiple-step liquid phase ion exchange (MLSIE) and solid state ion exchange (SSIE), results are shown in Figure A.1 and A.2, respectively. The materials prepared via liquid state ion exchange show a high adsorption capacity at low partial pressures, especially in the Ba^{2+} variants. The multi-step ion exchange procedure leads to a detrimental effect in the adsorptive properties of the material as discussed extensively in Chapter 2 for SAPO-34 materials.

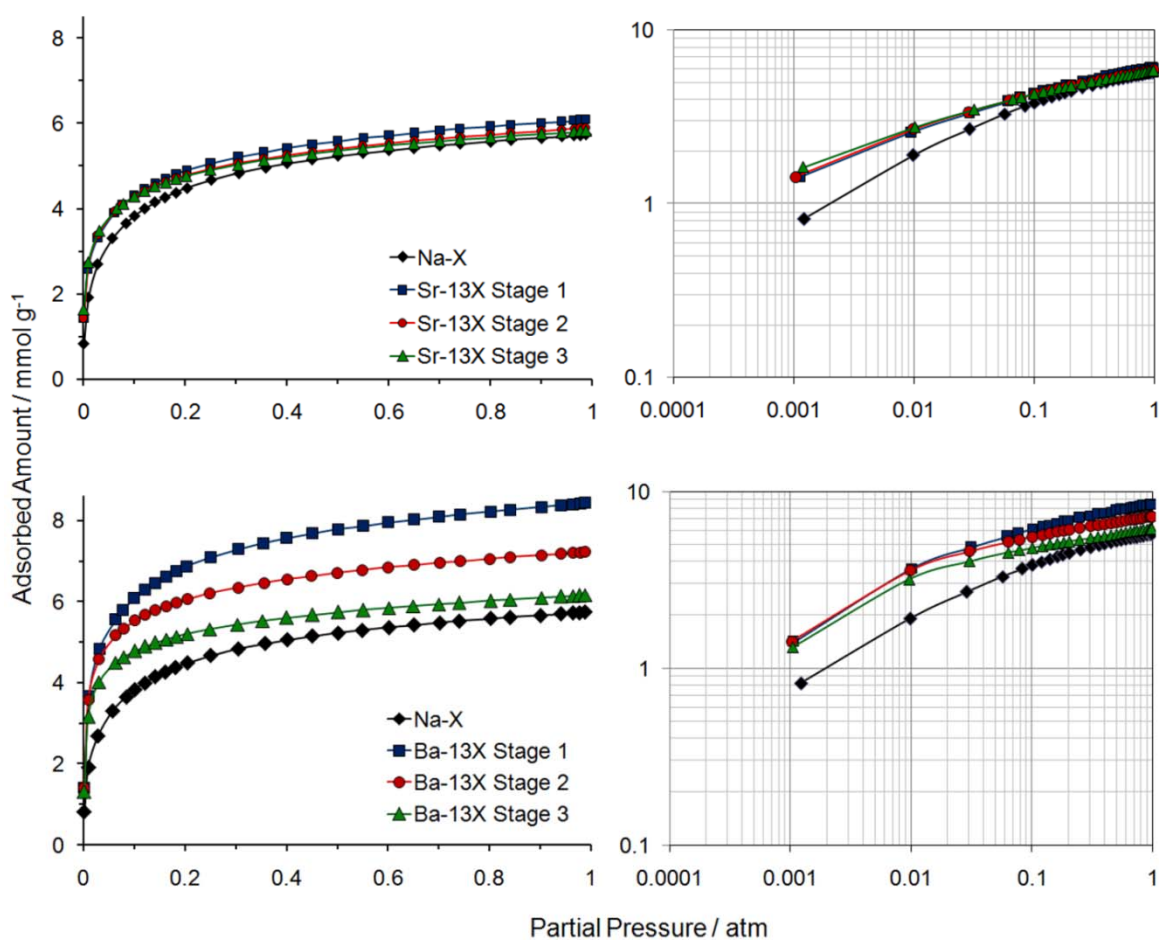


Figure A.1. CO_2 adsorption isotherms (normal and logarithm scales) at 25°C for Na^+ -13X and ion-exchanged samples prepared via multiple step liquid phase ion exchange. Stages 1, 2 and 3 refer to ion exchange for 24, 48 and 72 hours, respectively.

In addition, the CO₂ adsorption isotherm for ion exchanged Sr²⁺-13X materials prepared via solid state ion exchange (see Figure A.2) shows that the maximum CO₂ loading was obtained using 29 wt% SrCl₂ in the starting Na⁺-SAPO-34 material, although the results are below the ones for fully detemplated Na-13X material and the reported CO₂ adsorption of the sample prepared via liquid state ion exchange (see Figure A.1). The X-ray diffraction analyses indicate that the material loses crystallinity after the thermal treatment and this may also account for the reduced surface area and the CO₂ adsorption results.

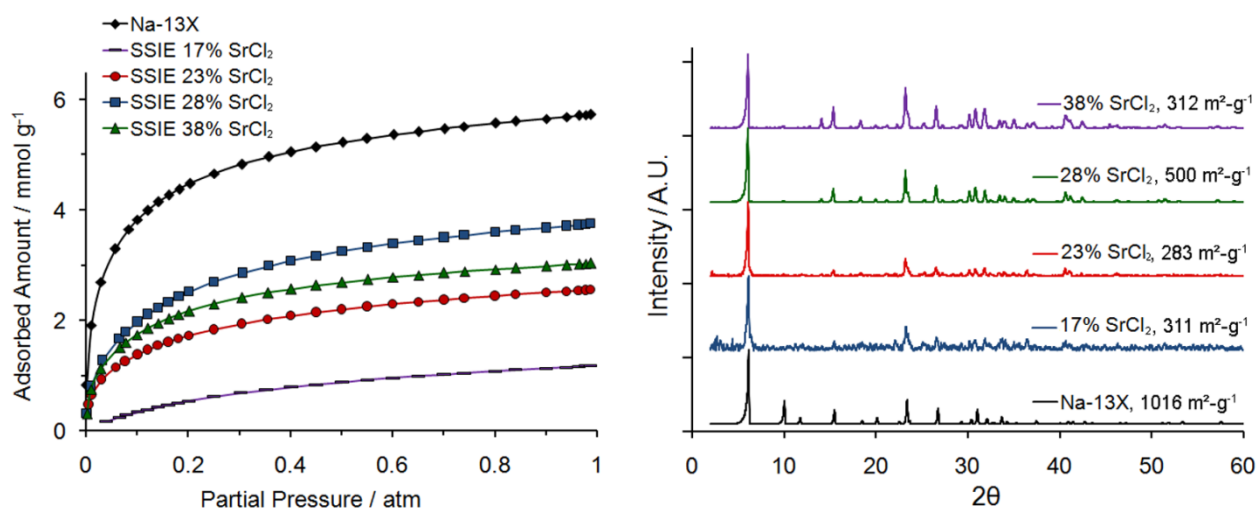


Figure A.2. CO₂ adsorption isotherms (normal and logarithm scales) at 25°C, X-ray diffraction analyses, and surface area for Na⁺-13X and ion-exchanged samples prepared via solid state ion exchange.

Furthermore, Figure A.3 shows pure component adsorption isotherms for CO₂, N₂, O₂ and CH₄ in Sr²⁺- and Ba²⁺-13X. It is observed the high selectivity of the materials toward CO₂ attributed to its relatively strong quadrupole moment interaction with the divalent cation electric field.

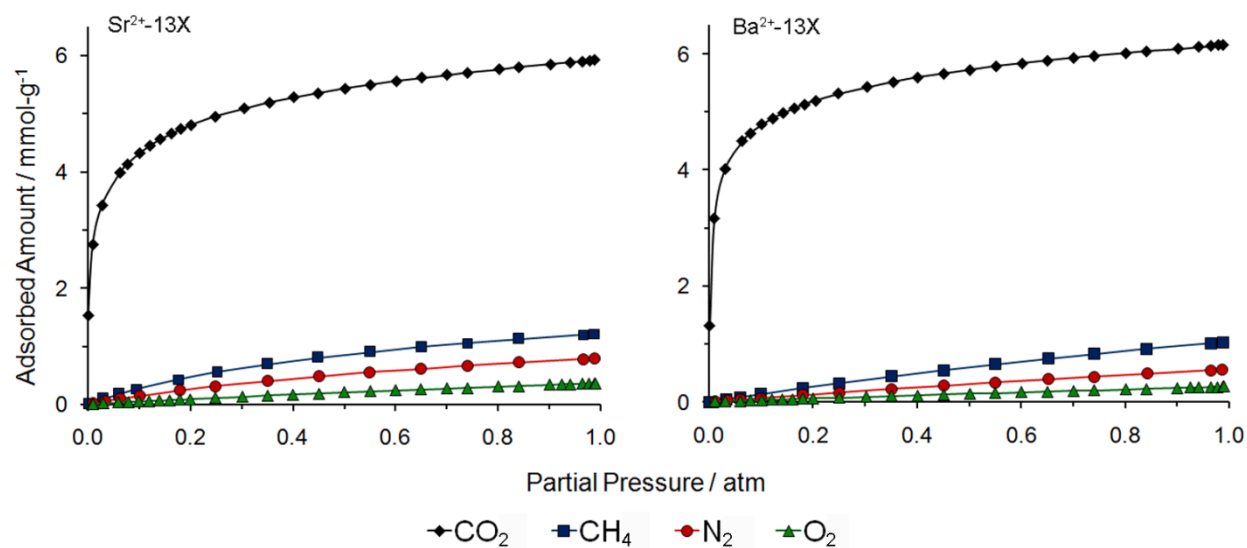


Figure A.3. CO_2 , CH_4 , N_2 and O_2 single gas adsorption isotherms for Na^+ -13X and Sr^{2+} and Ba^{2+} -13X after 72 hours of liquid state ion exchange (SII), gathered at 25°C .

Appendix B

Binder-less Procedure for Pelletizing Ion Exchanged Zeolitic Materials and CO₂ Adsorption for a Powder and a Pelletized Sample

1. Using a spatula, place ca. 0.5 grams of the zeolite inside a punch and die unit.



Figure B.1 Punch and die set used to prepare pellets of Sr²⁺-SAPO-34 material.

2. A pressure of 4500 lbs is then applied to the punch and die using a manual hydraulic tablet press. Replacing the die base with a hollow one and applying pressure should achieve successful retrieval of the tablet.
3. The resulting tablet is then shattered into small pieces using an Agatha mortar. Unless performed under ultra-dry conditions, it is critical not to apply too much friction during this stage to avoid zeolite dealumination.
4. The resulting small particles are sieved through a mesh of size 20 x 40 (0.841mm - 0.420mm). The coarser and finer particles are then gathered for reshaping.
5. Steps 1-4 are repeated until all particles have the desired mesh size.

Crystallinity and morphology were preserved after the pelletizing procedure as confirmed by X-ray diffraction and electron microscopy (data not shown here). Furthermore, CO₂ static volumetric adsorption experiments were used to evaluate the effect of the pelletizing procedure in the adsorptive performance of the material. Figure B.2 shows that the adsorption capacity of Sr²⁺-SAPO-34 was reduced after the pelletization procedure. The powder sample suffered a 20% loss in capacity during the preparation of the pellets. This is probably due to a slight decrease in surface area that resulted after the pelletization process. However, it should be noted that after normalizing their adsorbed amount by their respective Langmuir surface areas (N₂ adsorption isotherms at -196 °C) the isotherms for powder and pellets overlapped each other, suggesting that the loss in CO₂ adsorption capacity is proportional to the loss in surface area caused by the pelletizing process.

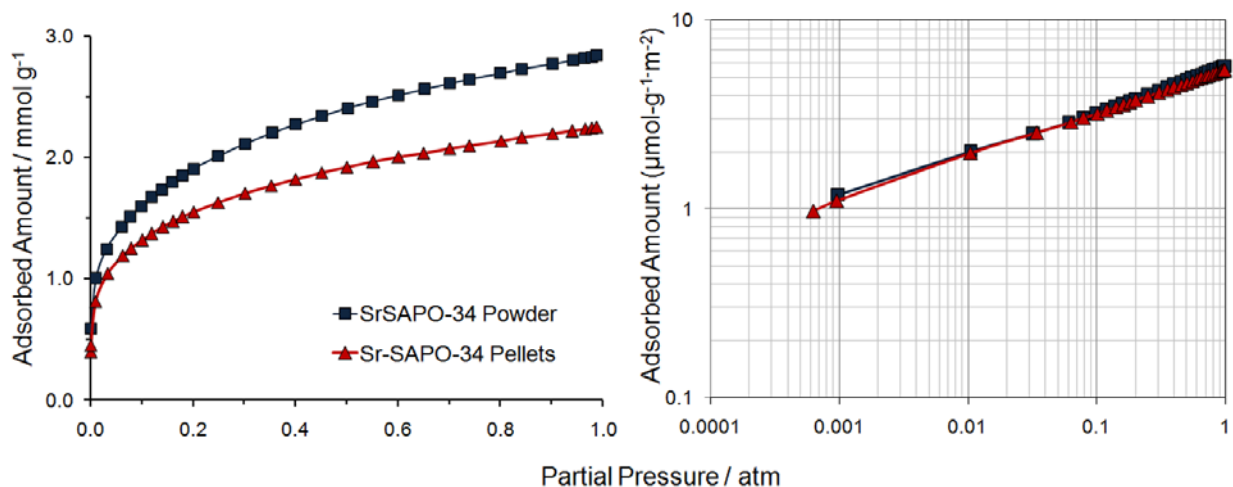


Figure B.2 CO₂ adsorption isotherms at 25°C for a powder and a pelletized ion-exchanged Sr²⁺-SAPO-34 material.

The pelletized material was used to determine CO₂ dynamic adsorption analyzes of the Sr²⁺-SAPO-34 material (breakthrough curves). Data is not presented here and is being prepared for publication in collaboration with NASA Ames Research Center.

Appendix C

Sr²⁺-SAPO-34 materials prepared via Wetness Impregnation and Solvent Mixing

Additional procedures to the ones proposed in the present dissertation can be used to distribute the salt throughout the matrix of the zeolite. Figure C.1 shows the CO₂ adsorption isotherm of a sample prepared using hexane to homogenize the salt throughout the powder zeolite (i.e. solvent mixing) and the adsorption isotherm of a sample prepared via wetness impregnation is also presented. Both procedures were followed by solid state reaction at 600 °C. The results clearly show that these methodologies are not effective for the salt-zeolite mixing procedure presenting lower CO₂ adsorption properties than the fully detemplated Na⁺-SAPO-34 material.

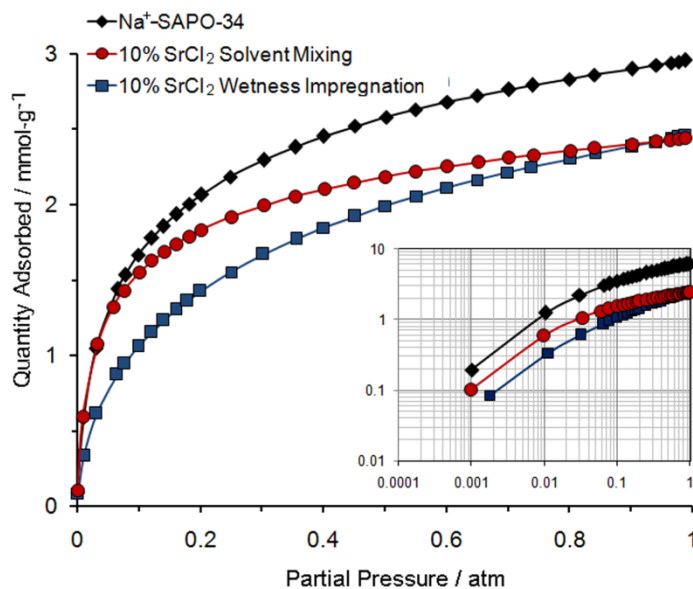


Figure. C.1. CO₂ adsorption isotherms (normal and logarithm scale) obtained at 25 °C of partially exchanged Sr²⁺-SAPO-34 prepared via solvent mixing or wetness impregnation and subsequent solid state ion exchange treatment. The figure also included isotherm data gathered for a fully detemplated Na⁺-SAPO-34 material.

Appendix D

Ion Exchanged Ba^{2+} -SAPO-34 Materials Prepared Via Coupled Partial Detemplation and Solid State Ion Exchange

Figure B.1. presents the CO_2 adsorption isotherms of ion exchanged Ba^{2+} -SAPO-34 materials were prepared via solid state ion exchange at 600 °C using as basis materials either NH_4^+ -SAPO-34 or partially detemplated Na^+TEA^+ -SAPO-34 materials with different amounts of barium chloride salt (BaCl). The samples prepared using NH_4^+ -SAPO-34 basis material do not show incorporation of Ba^{2+} cations after the solid state ion exchange procedure as observed in the CO_2 adsorption isotherm. On the other hand, for the samples prepared using Na^+TEA^+ -SAPO-34 as basis material, it was found that 10 wt% BaCl was enough to achieve solid state ion exchange.

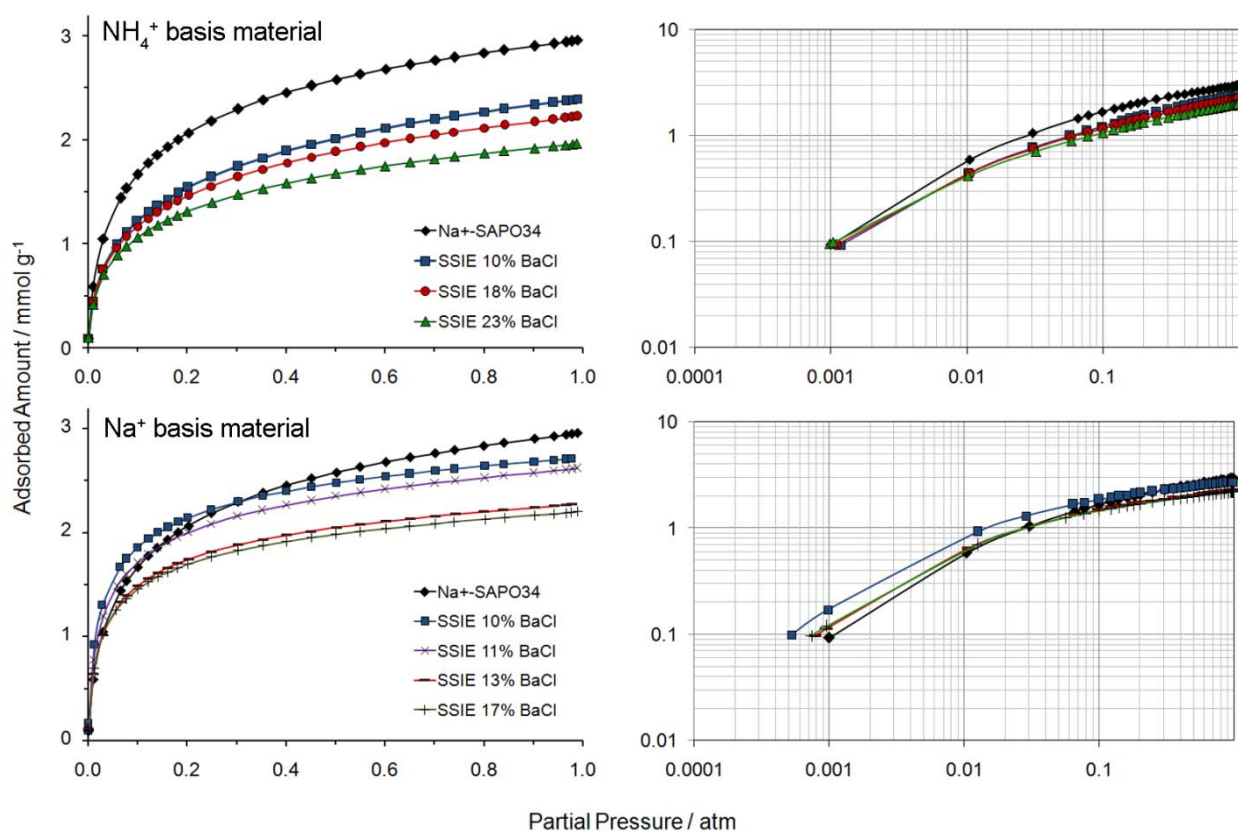


Figure D.1. CO_2 adsorption isotherms (normal and logarithm scale) obtained at 25 °C of partially exchanged Ba^{2+} -SAPO-34 prepared via Solid State Ion Exchange using A) NH_4^+ -SAPO-34 and B) as-synthesized Na^+ -SAPO-34 as starting materials. The figure also included isotherm data gathered for a fully detemplated Na^+ -SAPO-34 material.

Figure D.2 presents the CO₂ adsorption isotherm of partially exchanged Ba²⁺-SAPO-34 materials prepared via solid state ion exchange (SSIE), liquid state ion exchange (LSIE) and both SSIE-LSIE using as basis materials either NH₄⁺-SAPO-34 or partially detemplated Na⁺TEA⁺-SAPO-34 materials. The samples prepared using NH₄⁺-SAPO-34 basis material show no incorporation of Ba²⁺ cations after the solid state ion exchange procedure. For Na⁺TEA⁺-SAPO-34 was found that 10 wt% BaCl was enough to achieve solid state ion exchange.

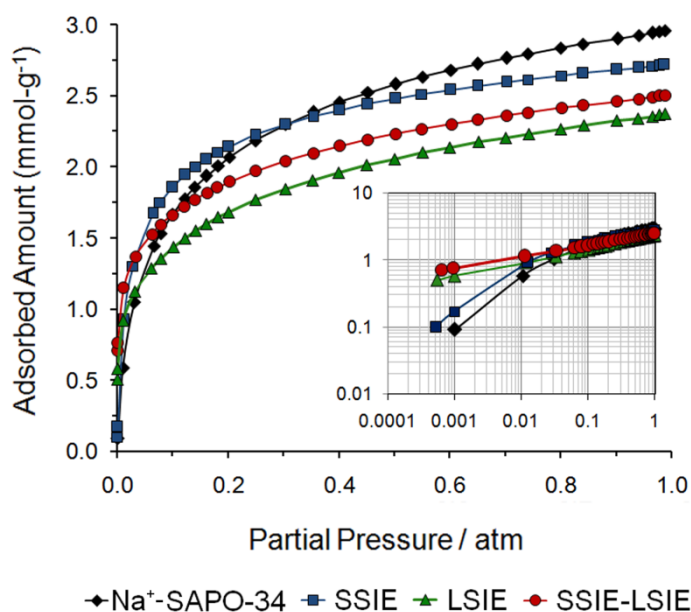


Figure. D.2. CO₂ adsorption isotherms (normal and logarithm scale) obtained at 25 °C of partially exchanged Ba²⁺-SAPO-34 via Coupled Partial Detemplation and Solid State Ion Exchange (SSIE), Solid State, Conventional Liquid State Ion Exchange (LSIE) and Liquid State Ion Exchange techniques together (SSIE-LSIE), respectively. The figure also included isotherm data gathered for a fully detemplated Na⁺-SAPO-34 material.

Appendix E

Deconvolution Parameters for ^1H and ^{23}Na MAS NMR spectra for SAPO-34 materials

Table E.1. ^1H MAS NMR deconvolution parameters for SAPO-34 samples.

Sample	Parameter	Peak 1	Peak 2	Peak 3	Peak 4					
Na ⁺ -SAPO-34	Frequency	5.4	4.8	1.8						
	Width	81.5	67.5	56.9						
	A(rel)	697	719	261						
NH ₄ ⁺ -SAPO-34	Frequency	5.3	4.9	1.8	6.8					
	Width	1358.52	463	3692	212					
	A(rel)	455	44	77	116					
		SSIE			SSIE-LSIE			LSIE		
		Peak 1	Peak 2	Peak 3	Peak 1	Peak 2	Peak 3	Peak 1	Peak 2	Peak 3
Sr ²⁺ -SAPO-34	Frequency	5.4	4.5	1.8	5.3	4.8	1.7	5.4	4.8	1.8
	Width	1974	747	1864	2831	1077	1432	3005	1102	1147
	A(rel)	805	386	145	677	770	66	659	810	52
Ba ²⁺ -SAPO-34	Frequency	5.3	4.7	1.8	5.2	4.9	2.2	5.5	4.9	1.8
	Width	2152	818	1238	2872	1106	591	3150	1244	1935
	A(rel)	874	453	49	566	788	54	647	443	72

Table E.2. ^{23}Na MAS-NMR deconvolution parameters for SAPO-34 samples.

Sample	Parameter	Peak 1	Peak 2					
Na ⁺ -SAPO-34	Frequency	-11.6	-19.9					
	Width	425	4242					
	A(rel)	360	648					
NH ₄ ⁺ -SAPO-34	Frequency	19.7						
	Width	4936						
	A(rel)	4936						
		SSIE			SSIE-LSIE		LSIE	
		Peak 1	Peak 2	Peak 3	Peak 1	Peak 2	Peak 1	Peak 2
Sr ²⁺ -SAPO-34	Frequency	-11.4	-18.8	0	-11.5	-19.4	-11.6	-17.9
	Width	442	3734	83	438	446	384	4425
	A(rel)	39	43		367	653	37	3993
Ba ²⁺ -SAPO-34	Frequency	-11.1	-19.2		-11.3	-18.9	-11.3	-18.2
	Width	389	3749		295	4173	881	4204
	A(rel)	364	237	57	3360	114	3580	

Table E.3. ^1H MAS-NMR deconvolution parameters for H^+ -SAPO-34 sample synthesized with triethylamine as template.

Sample	Parameter	Peak 1	Peak 2	Peak 3
H^+ -SAPO-34	Frequency	5.3	3.3	6.9
	Width	1755	2882	3992
	A(rel)	84	438	1302